



NUCLEAR FORENSICS APPLICATIONS OF
PRINCIPAL COMPONENT ANALYSIS ON
MICRO X-RAY FLUORESCENCE IMAGES

THESIS

Sarah T. Castro, 2nd Lieutenant, USAF
AFIT-ENP-MS-16-M-061

DEPARTMENT OF THE AIR FORCE
AIR UNIVERSITY

AIR FORCE INSTITUTE OF TECHNOLOGY

Wright-Patterson Air Force Base, Ohio

DISTRIBUTION STATEMENT A
APPROVED FOR PUBLIC RELEASE; DISTRIBUTION UNLIMITED

The views expressed in this document are those of the author and do not reflect the official policy or position of the United States Air Force, the United States Department of Defense or the United States Government. This material is declared a work of the U.S. Government and is not subject to copyright protection in the United States.

AFIT-ENP-MS-16-M-061

NUCLEAR FORENSICS APPLICATIONS OF PRINCIPAL COMPONENT
ANALYSIS ON MICRO X-RAY FLUORESCENCE IMAGES

THESIS

Presented to the Faculty
Department of Engineering Physics
Graduate School of Engineering and Management
Air Force Institute of Technology
Air University
Air Education and Training Command
in Partial Fulfillment of the Requirements for the
Degree of Master of Science

Sarah T. Castro, BS
2nd Lieutenant, USAF

March 2016

DISTRIBUTION STATEMENT A
APPROVED FOR PUBLIC RELEASE; DISTRIBUTION UNLIMITED

AFIT-ENP-MS-16-M-061

NUCLEAR FORENSICS APPLICATIONS OF PRINCIPAL COMPONENT
ANALYSIS ON MICRO X-RAY FLUORESCENCE IMAGES

THESIS

Sarah T. Castro, BS
2nd Lieutenant, USAF

Committee Membership:

Dr. John W. McClory
Chair

Lt Col Briana J. Singleton, Ph.D.
Member

Dr. Tony D. Kelly
Member

Abstract

A method is developed for rapid detection and analysis of actinides and correlated materials in nuclear fallout debris using principal component analysis on quantified micro x-ray fluorescence intensity values. This method is then applied to address goals of nuclear forensics. The first implementation is a collaborative effort with the National Institute of Standards and Technology and the Federal Bureau of Investigation Laboratory to produce a standard reference material that is a surrogate for glassy nuclear fallout debris in a modern urban environment. This reference material will enable researchers in the development and validation of nuclear forensics methods. A method for determining material homogeneity is developed and demonstrated. A preliminary minimum sample size for the surrogate fallout SRM is calculated to be 0.607 g based on an infinite thickness depth of 2.242 mm. It is also shown that, for an adequately simple model, the surrogate fallout SRM is indistinguishable from real fallout. The second implementation is a quantitative analysis of element-actinide correlation in historical nuclear test fallout debris, which will contribute further to the body of knowledge surrounding the formation of nuclear fallout. Eleven historical fallout samples are used. A method for determining the elemental composition descriptors that best account for the variance in these samples is developed. A trend in the composition of media surrounding areas of significant activity, based on correlation of autoradiography images, is confirmed for micro x-ray fluorescence.

For the Chuckleheads, my wonderful and unusual nuclear family.

I couldn't ask for better friends.

Acknowledgements

I would like to thank my thesis committee for their guidance and patience throughout this process, as well as my sponsor, the Defense Threat Reduction Agency, for funding this research. Additionally, I extend great thanks to the National Institute of Standards and Technology and the FBI Laboratory for their collaboration and expertise, as well as to the National Physical Laboratory and Lawrence Livermore National Lab for their contributions. Specifically, I would like to thank Dr. Jackie Mann and Dr. John Molloy for their enthusiasm in answering my many firestorms of electronic correspondence.

Sarah T. Castro

Table of Contents

	Page
Abstract	iv
Acknowledgements	vi
List of Figures	ix
List of Tables	xiii
1. Introduction	1
1.1 Overview	1
1.2 Motivation	3
1.3 Problem Statement	4
1.4 Scope of Study	4
1.5 Sponsorship and Partnership	5
2. Previous Research	6
2.1 Early Forensic Research	6
2.2 Fuel Source	7
2.3 Fahey	7
2.4 Wallace	8
2.5 Monroe	9
2.6 Dierken	9
2.7 Molloy and Sieber	11
3. Theory	17
3.1 Nuclear Fallout Formation	17
Fission Fragments and Radioactive Decay Products	17
Fractionation	18
3.2 X-Ray Fluorescence	19
Infinite Thickness	22
3.3 Silicon Drift Detectors	24
Peltier Cooling	25
3.4 Principal Component Analysis	26
Algorithm	26
Underlying Assumptions	29
3.5 Reference Materials	29
Types of Certified Reference Materials	30
Production and Certification Process	31

	Page
4. Experiment	33
4.1 Sample Preparation	33
NIST SRM	33
Historical Test Fallout Debris	35
4.2 Equipment	36
Horiba XGT-7200 X-Ray Analytical Microscope	36
Die and Press	40
4.3 Research Approach	40
Experimental Techniques: NIST	41
Experimental Techniques: LLNL	43
Computational Techniques	44
5. Results: NIST SRM	48
5.1 Micro-XRF Results	48
SRM 2702 and 2703	48
SPUD Blanks	54
5.2 Principal Component Analysis	56
Test Data Set	56
SRM 2702 and 2703	58
SPUD Blanks	68
6. Results: Fallout	81
6.1 Micro-XRF Results	81
6.2 Principal Component Analysis	83
Sample Separation	83
Actinide Correlation	95
7. Conclusion	105
7.1 Conclusions of Research	105
7.2 Recommendations for Future Research	106
7.3 Significance of Research	107
Bibliography	109

List of Figures

Figure		Page
1	Monroe study results comparing autoradiography, micro-XRF, and SEM images.....	10
2	Dierken study results comparing BSE and autoradiography images	12
3	Molloy study PCA results for SRM 2702 and 2703	14
4	Molloy study PCA results for SRM 1729	15
5	Chart of Nuclides with line of stability.....	17
6	Generation of incident x-rays inside the XRF detector	20
7	Physics of x-ray fluorescence at the atomic level.....	21
8	Transitions for x-ray emission lines	22
9	The AXAS-M silicon drift detector unit used in this study	25
10	SRM 2702 in pressed briquette form (left) and loose powder form (right).	34
11	SPUD-1 Test 1 in pressed briquette form	35
12	AFIT Horiba detector setup.....	37
13	The five pieces of the die used to press the SRM material: base, die, plunger, and two anvils.	41
14	An auto-ID sample spectrum from a data collection on SRM 2702. Peak values represent counts at each energy and are labeled with the element line to which they correspond.	48
15	An auto-ID sample spectrum from a data collection on SPUD-1. Peak values represent counts at each energy and are labeled with the element line to which they correspond.	54
16	Biplot of the first and second principal components of Fisher's Iris data.	57

Figure		Page
17	Scatter plot, color-coded by species, of the first and second principal components of Fisher's Iris data.	57
18	PCA results for stability measurements on SRM 2702.	60
19	PCA results for random measurements on SRM 2702.	61
20	PCA results for stability measurements on SRM 2703.	62
21	PCA results for random measurements on SRM 2703.	63
22	Scatter plot, with element labels and color-coded by measurement time, of six different tests of the same 100 points using measurement times of 5, 10, 15, 20, 25, and 30 seconds.	67
23	PCA results for stability measurements on SPUD-1 Test 1.....	69
24	PCA results for random measurements on SPUD-1 Test 1.....	70
25	PCA results for stability measurements on SPUD-1 58b.	71
26	PCA results for random measurements onSPUD-1 58b.	72
27	NIST PCA results plot for SPUD-1 Test 1.....	74
28	PCA results for stability measurements on SPUD-1 Test 1 using only important descriptors.....	76
29	PCA results for random measurements on SPUD-1 Test 1 using only important descriptors.....	77
30	PCA results for stability measurements on SPUD-1 58b using only important descriptors.	78
31	PCA results for random measurements on SPUD-1 58b using only important descriptors.	79
32	The fallout samples used in this experiment shown mounted in aluminum disks. Disk 1 is on the left and Disk 2 is on the right. Samples that were examined are indicated with red boxes.	81

Figure		Page
33	Autoradiography and micro-XRF raster scans for each of the LLNL fallout samples examined in this experiment.	82
34	Scatter plot, color-coded by sample, of a comparison of all samples examined in this study. PCA was conducted upon the element intensity values of every element that all fourteen samples had in common.	85
35	Scatter plot, color-coded by sample, resulting from PCA performed upon all eleven LLNL fallout samples using all element intensities.	86
36	Biplot resulting from PCA performed upon all eleven LLNL fallout samples using all element intensities. Vectors show how each element influences the variance in the samples.	87
37	Scatter plot, color-coded by sample, of a comparison of all samples examined in this study. PCA was conducted upon the element intensity values of every element shown to have an above-average influence on the results shown in Figure 34.	90
38	Scatter plot, color-coded by sample, resulting from PCA performed upon all eleven LLNL fallout samples using every element shown to have an above-average influence on the results shown in Figure 35.	91
39	Scatter plot, color-coded by sample, of a comparison of all samples examined in this study. PCA was conducted upon the element intensity values of every element shown to have an above-average influence on the results shown in Figure 37.	93
40	Scatter plot, color-coded by sample, resulting from PCA performed upon all eleven LLNL fallout samples using every element shown to have an above-average influence on the results shown in Figure 38.	94
41	Biplot resulting from PCA performed upon all eleven LLNL fallout samples using every element shown to have an above-average influence on the results shown in Figure 38.	95

Figure		Page
42	Scatter plot, color-coded by activity and uranium content, resulting from PCA performed upon all samples examined in this study using all element intensities.	97
43	Scatter plot, color-coded by activity and uranium content, of a comparison of all samples examined in this study. PCA was conducted upon six element intensity values: Ca, Si, Fe, K, Ti, and Cu.	98
44	Scatter plot, color-coded by activity, resulting from PCA performed upon all eleven LLNL fallout samples using all element intensities. Notable clustering is seen for the ninetieth percentile, represented by black stars.	99
45	Scatter plot, color-coded by activity, resulting from PCA performed upon all eleven LLNL fallout samples using six element intensity values: Ca, Si, Fe, K, Ti, and Cu. The notable clustering is seen for the ninetieth percentile is maintained even when the model is simplified.	100
46	Scatter plot, color-coded by species, of results of PCA performed on fallout element intensity data for five elements (Ca, Si, Fe, K, and Ti) that was first scaled based on the autoradiography pixel value associated with each spectrum. Regions with more radioactivity trend toward the right-hand side of the plot.	102

List of Tables

Table	Page
1	SPUD-1 sample identification alphanumerics and masses. 36
2	Horiba detector general information. 37
3	Horiba detector settings for SRM 2702 and 2703 with NIST-recommended parameters. 42
4	Horiba detector settings for SPUD with NIST-recommended parameters. 43
5	Horiba detector settings for LLNL samples. 44
6	Quantified XRF results and comparison to NIST values for SRM 2702..... 50
7	Quantified XRF results and comparison to NIST values for SRM 2703..... 51
8	Quantified XRF results for SRM 2702..... 52
9	Quantified XRF results for SRM 2703..... 53
10	Quantified XRF results for SPUD-1 Test 1. Values are intensities (c/s/mA). 55
11	Element intensity averages for locations with the highest amount of activity compared to element intensity averages for each sample. 103
12	Element mass percentage averages for locations with the highest amount of activity compared to element mass percentage averages for each sample. 103

NUCLEAR FORENSICS APPLICATIONS OF PRINCIPAL COMPONENT ANALYSIS ON MICRO X-RAY FLUORESCENCE IMAGES

1. Introduction

1.1 Overview

The goal of this research is to develop a method for rapid detection and quantitative analysis of element-actinide correlation in nuclear fallout debris using micro x-ray fluorescence analysis (micro-XRF) and principal component analysis (PCA). Two separate but related projects converge to meet this objective: first, the creation of a standard reference material (SRM) that is a surrogate for nuclear fallout debris in a modern, urban environment; second, the quantitative analysis of elemental distribution in fallout debris from historical surface tests.

Surrogate fallout samples were synthesized at the National Physical Laboratory in the United Kingdom and are composed of finely ground glassy material containing known quantities of radionuclides and other elements [1]. Upon arrival, loose powder samples were pressed into briquettes for examination. Sample preparation and handling techniques at AFIT mirror those used at the Federal Bureau of Investigation Laboratory (FBI Laboratory) as closely as possible. Obtaining accurate elemental composition information is of paramount importance, as this facet of the study is accomplished in pursuit of an SRM certified by the National Institute of Standards and Technology (NIST).

The nuclear forensics community is in need of certified standards that will allow for more accurate development of debris analysis methods. Standards allow analysts to

verify the results of their methods based on alignment with established values, which are developed under a rigorous system. For this reason, a particular interest of this study is the determination of a minimum sample size for the forthcoming standard. This is the smallest amount of the SRM that is proven to contain the elemental composition guaranteed on the standard certificate. This requires a certain degree of homogeneity throughout the material, as significant heterogeneities, or “nugget” effects, are known to skew results.

The historical fallout samples originate from nuclear tests conducted at the Nevada Test Site between 1951 and 1992. In order to ensure that environmental soil contributed to the composition of the fallout particles, this study focuses on fallout from surface tests. While studies of element-actinide correlation have been conducted at AFIT in the past [2,3], quantitative analysis of the data collected in those studies has been difficult to achieve due to machine and spatial reference limitations. PCA is used to develop a method to advance this process. The ability to quantitatively compare elemental distributions between samples and modalities will contribute positively to the accuracy of current analysis methods.

The historical fallout debris used in this study consists of 10 glassy spheroids with nominal diameters of < 1 mm. A past study, conducted by an AFIT student in 2014 [3], halved 48 spheroids and mounted them in epoxy on two carbon-coated aluminum sample mounts for scanning electron microscopy (SEM) and autoradiography (AR) measurements. Micro-XRF analysis could not be performed at that time due to the limitations of an aging machine. Recent upgrades to AFIT micro-XRF capabilities have made it possible for these measurements, as well as their comparison to the data collected in the 2014 study, to take place.

Once sample spectra were collected and averaged, PCA was conducted on the data. PCA allows a statistical examination of a multivariate sample set by tracking

the variance in the data and the variables that account for it. A minimum sample size for the surrogate fallout debris is found through a study of the amount of material needed to produce relative homogeneity, or statistical similarity between an average of random points over the surface of a sample and an average of the same number of measurements at a single location. PCA is also used to develop a method for quantitative analysis of element-actinide correlation in real fallout samples.

1.2 Motivation

A post-detonation, fresh-fission-product SRM representative of nuclear fallout in a modern urban environment does not currently exist. NIST seeks to create this surrogate nuclear debris to serve as a standard that can be used to reliably test nuclear forensics measurement capabilities. Once developed, this SRM will improve method development, validation, testing, and preparedness in the nuclear forensics community by providing a material with known chemical concentrations and isotope composition. Furthermore, the existence of a standard allows government agencies, including the FBI Laboratory, to demonstrate the efficacy, accuracy, and precision of their analysis methods. Their measurements can then be used as legal evidence in a court of law [1]. This will be a valuable capability in the nuclear forensics process in the event of a nuclear detonation.

The use of micro-XRF with PCA as a method for the quantitative analysis of element-actinide correlations in nuclear fallout has the potential to contribute to the efficient execution of time-sensitive nuclear forensics. While micro-XRF will likely not be used on fresh fallout material, as fission product radiation would overwhelm the detector, useful information on the nature of fallout can be collected by examining historical fallout particles. Correlation between unfissioned fuel and other elements or media in fallout particles are one example. A strong preferential correlation between

uranium or plutonium fuel, where the analysis of this fuel can be used for attribution, and a particular carrier medium in fallout would tell analysts where to look first for this valuable content. The ultimate goal of this line of research is to develop an accurate system for identifying the forensic usefulness of a fallout particle by visual inspection, allowing for more efficient focus of resources.

1.3 Problem Statement

This research seeks to show that the assessment of micro-XRF data with PCA is a viable technique for characterizing radionuclide content and correlation in fallout samples. The development of an SRM that is a surrogate for nuclear debris, which can be developed, certified, and applied to the nuclear forensics collection effort, will be instrumental to this work. Results will be analyzed in a twofold manner: first, to determine the relative homogeneity of the NIST samples, which will indicate the smallest sample size for which the NIST-certified values for elemental content and uncertainty hold true for micro-XRF measurements; second, to develop a quantitatively-validated method for rapid identification of areas of interest in nuclear fallout particles, which can then be examined in a more focused manner with more time-consuming forensics techniques.

1.4 Scope of Study

NIST will provide SRM 2702, SRM 2703, and surrogate post-detonation urban debris (SPUD) doped with natural uranium (blanks) in advance of a future “hot” material, which will be doped with enriched uranium. Enough material will be provided for approximately fifteen samples of each type. However, due to time constraints, only two SPUD blanks will be analyzed in this study. This study will utilize instruments located at AFIT in tandem with a similar study performed at the FBI Laboratory for

validation. Micro-XRF characterization will examine the presence of radionuclides in the samples while also mapping the presence of other elements. PCA will then be conducted on these results, serving to determine the relative homogeneity of the material and minimum sample size needed to eliminate nugget effects, which might affect method development results for a third party. Micro-XRF results from real nuclear fallout samples will also be analyzed to determine whether PCA is a useful technique for the quantitative determination of element-actinide correlation in fallout.

1.5 Sponsorship and Partnership

This research is sponsored by the Defense Threat Reduction Agency (DTRA) and completed in partnership with the National Institute of Standards and Technology (NIST), the Federal Bureau of Investigation (FBI), and Lawrence Livermore National Laboratory (LLNL).

2. Previous Research

The analysis and characterization of nuclear fallout debris has been the focus of many experiments, dating from the time period immediately surrounding the first weapons tests to the present day. Of interest to this study are those that used non-destructive techniques to characterize elemental compositions of debris samples, particularly micro-XRF. Studies using either destructive or non-destructive techniques, or a combination thereof, to determine the age and origin of nuclear material were also examined.

PCA has widespread function in many different fields of study. For this reason, this study focuses on previous research in this area that uses PCA to examine sample heterogeneity, especially in analyzing standard reference materials.

2.1 Early Forensic Research

Nuclear fallout debris research conducted in the late 1950s and early 1960s [4–6] sought to characterize particles, both in bulk and individually, in pursuit of a broad understanding of fallout formation. These studies established a relationship between different heights of burst and types of fallout. Fallout analyzed in these studies came from a variety of nuclear tests ranging from high air bursts, resulting in spherical and homogeneous particles, to ground surface bursts, resulting in more irregular particles [4]. It was determined that radioactivity is more concentrated in particles with constituents that are altered in form by interaction with the detonation (i.e., those that are melted and re-condensed, forming glassy spheres or components [5]) than in particles that are simply displaced [6]. Researchers also recognized that analyzing many fallout particles at once did not provide as much information about fallout formation as the analysis of individual particles, which allowed for a more detailed

examination of the correlation between actinides and other media present in fallout. This was particularly true for tests that used a tower as a weapon emplacement platform, indicating that materials most closely associated with the weapon before it detonates should be most strongly correlated with fuel remnants in the fallout [5].

2.2 Fuel Source

Several studies [7–10] focused on identification of fuel sources via elemental composition and morphological characteristics. The bulk of these studies were conducted on fallout from the 1945 Trinity test, though one instead focused on soil samples from the vicinity of the BOMARC accident in 1960 [7]. Elemental composition analyses allowed researchers to determine the relative age of actinide particles in samples drawn from different nuclear tests in the same location, as well as the type of test from which each likely originated [8]. It was also shown that researchers could confirm the grade of plutonium used at the Trinity test via independent analysis of trinitite, even six decades later [9]. Yield was also estimated based on the percentage of radionuclides remaining from the original detonation [10]. Gostic [7] emphasized the importance of environmental interpretation to forensics, stating that particles with the same origin should share common morphological characteristics, but some of those characteristics can be changed by environmental processes after a detonation occurs. Therefore, it is vital to be able to determine which characteristics in fallout particles are indicative of the source, and which are affected by the detonation environment.

2.3 Fahey

Conducted in 2010, Fahey’s study focused on attribution using post-detonation nuclear debris—in this case, a single piece of trinitite. Fahey concluded that forensic analysis must yield information about both nuclear and non-nuclear device materials

and their correlation in order to best identify the source of a weapon. Furthermore, he concluded that microscopic analysis methods (SEM, micro-XRF, light microscopy, autoradiography, secondary ion mass spectrometry, and backscattered electron imaging) are a necessary addition to bulk methods. This is because of the importance of spatial correlation, which can help identify elements in glassy fallout that were involved in the construction of the weapon rather than native to the detonation site. Isotopic composition is also vital to attribution, and it is suggested that microanalysis may identify geographically different isotopic compositions that can point to potential material sources [11].

Of interest, if not directly related to the specifics of correlating microanalysis techniques, is a comment made in Fahey’s discussion of uncertainty. The error is large in this study “because the concentration of each [radionuclide] element varies considerably and there are no standards containing known amounts of Pu and U with a major element composition similar to the [trinitite] glass” [11]. A standard such as the one NIST seeks to create would assist in decreasing uncertainty in the further development of this method for forensic attribution, and potentially many others as well.

2.4 Wallace

This study corroborates Fahey’s conclusion that material used in the construction of a weapon often correlates spatially to nuclear material found in fallout debris, emphasizing the need for spatial microanalysis instead of reliance on bulk techniques. Fourteen samples of trinitite were examined using SEM, alpha track and beta radiography, and electron microprobe. Wallace concluded that the majority of activity was concentrated in or near the glassy surface layer, particularly in areas rich in calcium and iron [12].

2.5 Monroe

Monroe’s research, conducted in 2013, focused on elemental identification in twelve nuclear fallout debris samples from the Nevada Test Site. Three different techniques were used to correlate elemental distribution patterns: micro-XRF, SEM, and AR. The micro-XRF system used here was the same AFIT system later used to perform this study. A side-by-side comparison of the results of these non-destructive analysis techniques are shown in Figure 1.

The results from the three different techniques were analyzed in concert to find non-radionuclide elemental indicators of activity presence and location in a sample. The intent of this research was to focus the use of analytical forensics to areas of interest in the case of time-sensitive fallout analysis. Monroe concluded that micro-XRF was “useful for determining bulk composition of major and minor elements, but did not detect trace elements” [2]. A possible reason for this issue is the fact that measurements in this study were not taken under vacuum, which made quantitative comparison impossible. The XRF software does not provide quantitative measurements for elemental composition unless either the probe head or the chamber is placed under vacuum. These configurations are helpful in decreasing Compton scattering background effects and other x-ray interactions with particles in the air, while also increasing detector sensitivity to light elements. Further conclusions suggest that regions rich in calcium and aluminum may correlate to actinide presence.

2.6 Dierken

Dierken’s research followed a similar approach to Monroe’s, with some improvements. In this study, 48 fallout particles with diameters < 1 mm were analyzed using image registration of AR and SEM scans. In this case, no micro-XRF was accomplished due to prohibitively high noise in an aging system. The goals of this research

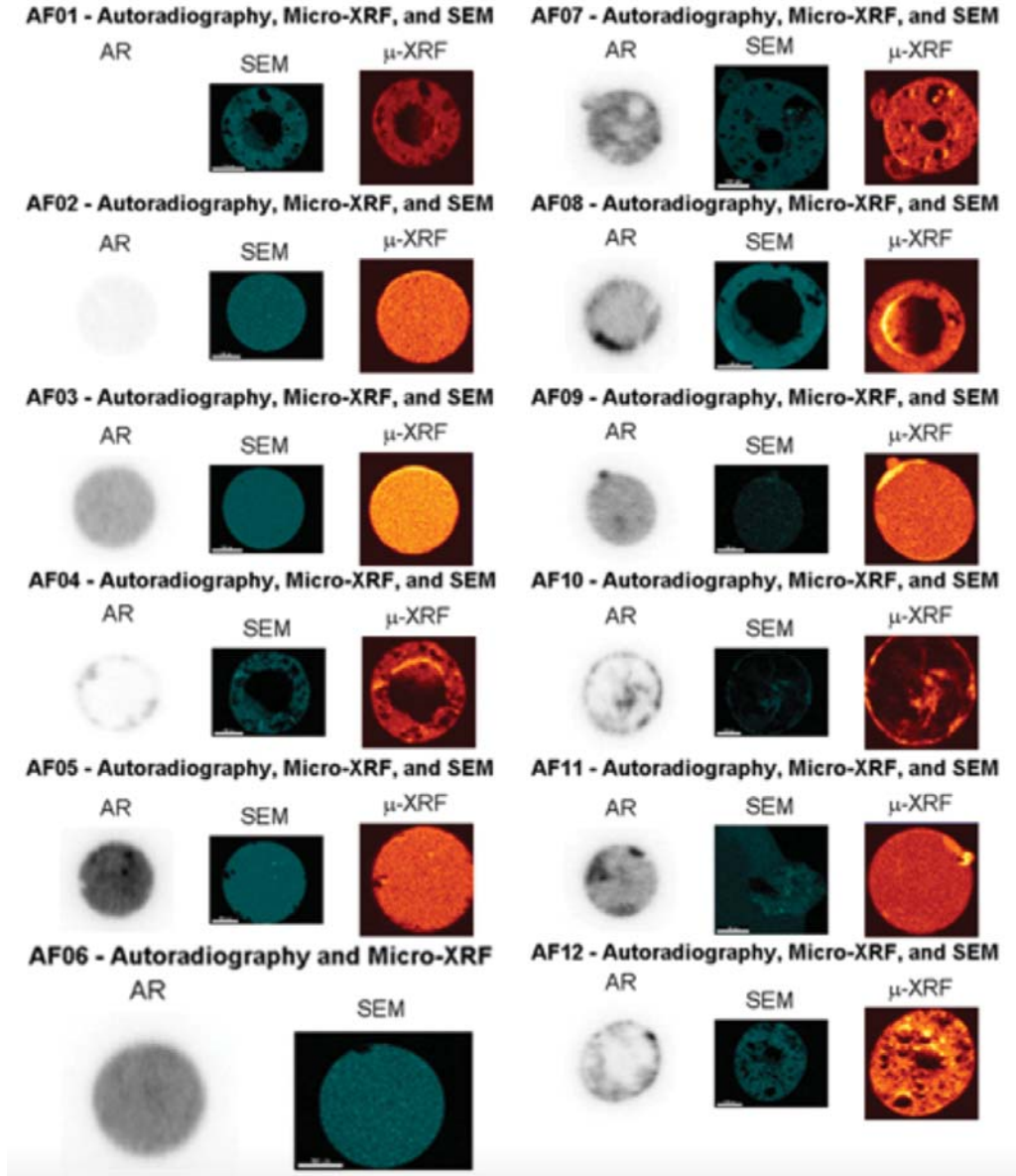


Figure 1. Comparison of results for all 12 of Monroe's samples. From left to right for each sample: autoradiography results, micro-XRF map, SEM map [2].

were: to determine the nature of plutonium weapon fuel collocation with environmental materials, to develop procedures for efficient data mapping and processing, and to understand the nature of fallout particle formation via correlation between activity and elemental distribution.

Multi-modal image registration is the use of two images produced by different modalities to express meaningful insights not apparent in separate analyses. This technique was used to correlate Dierken's AR and SEM results. Areas of high activity were superimposed upon an elemental map of a sample to determine the composition of the surrounding material. For this method, point matching is of paramount importance, because the loss of spatial information makes quantitative comparison of data impossible. One example of the image overlay technique used in this study is shown in Figure 2.

Dierken concluded that unfissioned plutonium fuel preferentially associates with the compositions in the fallout particles that are most capable of diffusion, such as mafic glass [3]. While many of these compositions are rich in calcium, this is not always the case; therefore, a conclusive connection to calcium cannot be made. The preferential association with mafic glass suggests that small particle sizes and materials with low melting points are more likely to allow these compositions to associate with the plutonium fuel as the fireball cools.

2.7 Molloy and Sieber

The intent of this research was a reduction in minimum sample sizes for SRM. Because the needs of analysts differ across disciplines and experimental techniques, NIST found that, in many cases, the certified sample size for an SRM was too large for some equipment and processes. It was desired, therefore, to attempt to decrease minimum sample size while maintaining sample consistency. This was accomplished

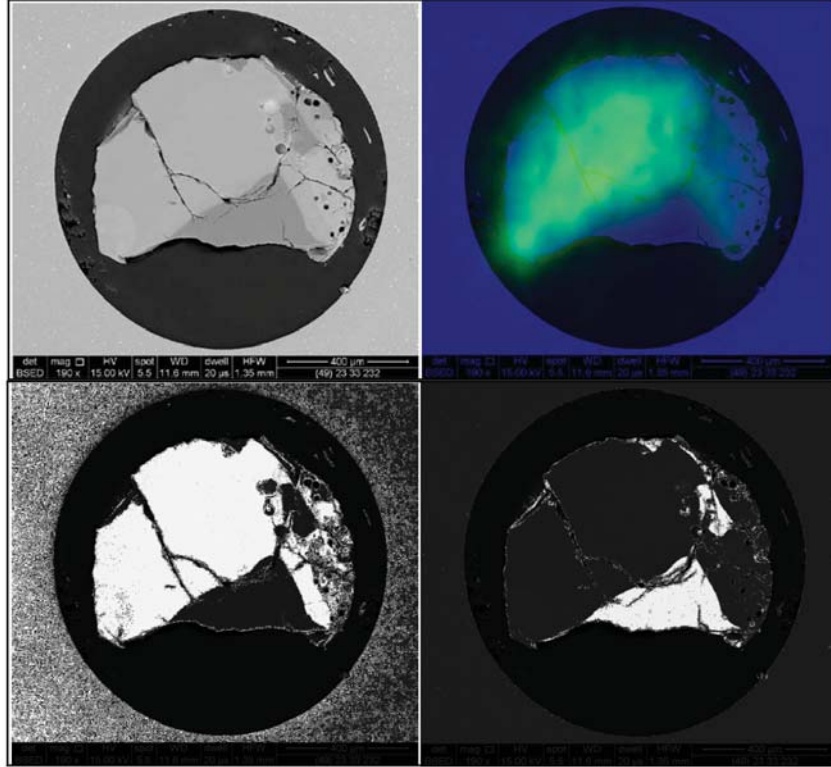
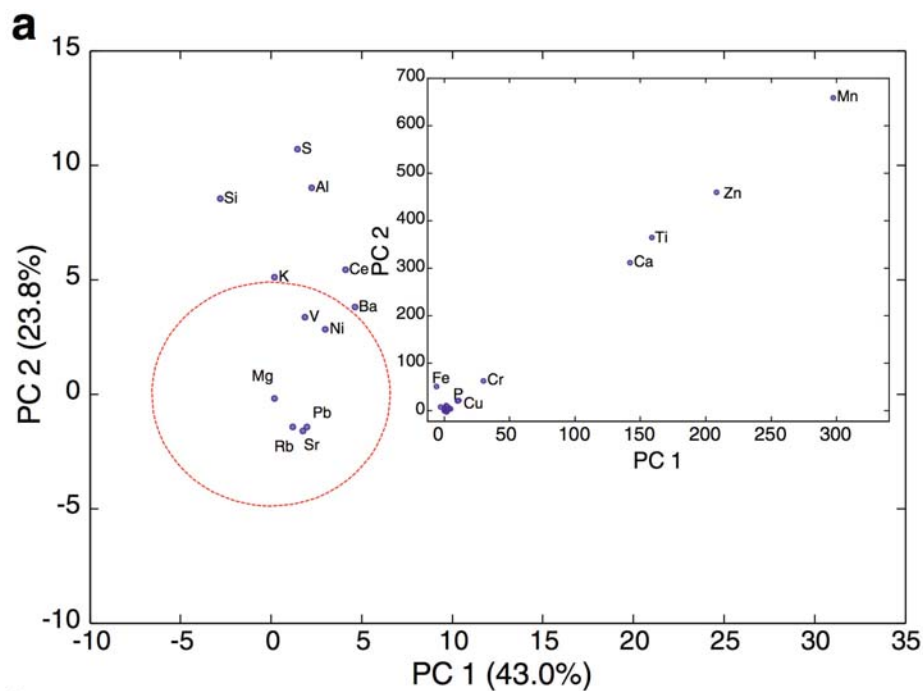


Figure 2. Image overlay for a single particle analyzed in the Dierken study. The backscattered electron image (top left) shows that calcium-rich distributions (highlighted in bottom left image) and silicon inclusions (highlighted in bottom right image) are present in this particle. The autoradiography overlay (top right), shows that areas of high activity overlap mafic glass phases [3].

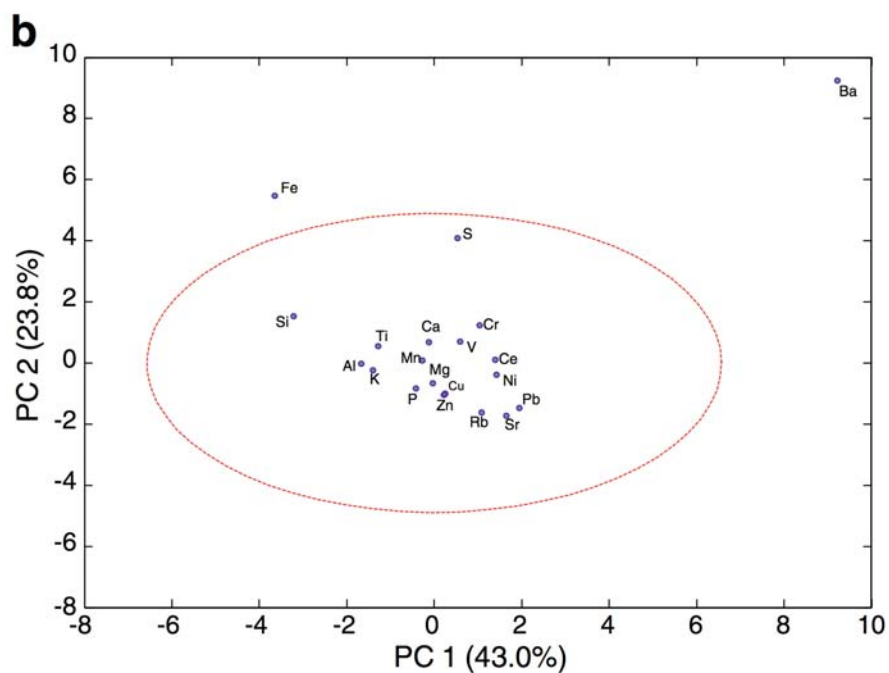
through a study of material heterogeneity.

Micro-XRF was used to investigate elemental distributions without destroying samples. In this case, SRM 2702 and 2703 were used. 2702 and 2703 are composed of the same material —marine sediment from Baltimore Harbor —with different levels of homogenization. 2702 is more heterogeneous, and therefore more likely to display nugget effects, than 2703. Samples in the sub-milligram mass range were examined for both materials. Two-dimensional maps of elemental concentrations in both samples were created and analyzed using PCA. PCA was run iteratively on different sample masses until the average heterogeneity of a map of uniformly spaced data points was statistically indistinguishable, with 99.5% confidence, from that of the same amount of data collected at a single point. The repeated data collection at a single point, or “stability measurement,” is taken as an expression of variance due to all factors outside of sample composition [13]. Results are shown in Figure 3.

Further research conducted at a later time assessed the minimally adequate number of data points needed for an accurate representation of the sample material based on data point selection methodology. SRM 1635a, which consists of homogenized subbituminous coal, and SRM 1729, a tin solder alloy formulated from tin and lead, were used for this analysis. Different sampling techniques were tested, including sampling uniformly spaced adjacent points, raster scanning, and random point selection. Random point selection was determined to be the most practical approach [14], converging on a stable average value of count rate with several orders of magnitude fewer measurements than the other techniques. The confidence ellipses in Figures 3 and 4 are illustrative of three standard deviations from the mean of each principal component, or a 99.5% confidence interval. The difference between raw data and the average of 1000 random points for SRM 1729 is clearly demonstrated. In Figure 4a, a significant number of points fall outside the confidence ellipse, indicating perceived

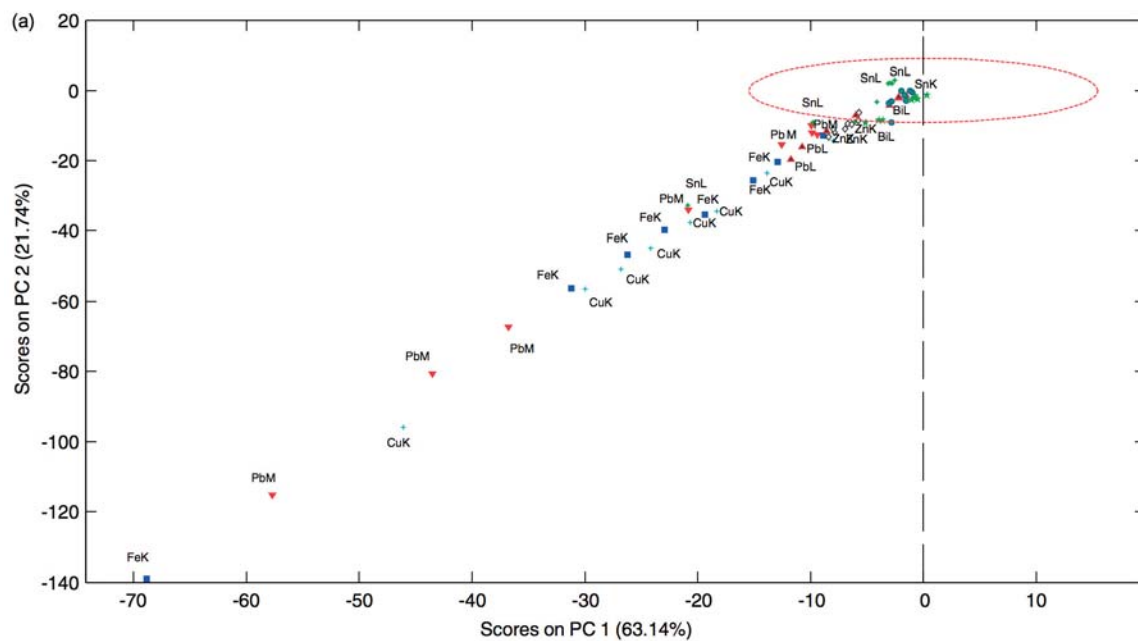


(a)

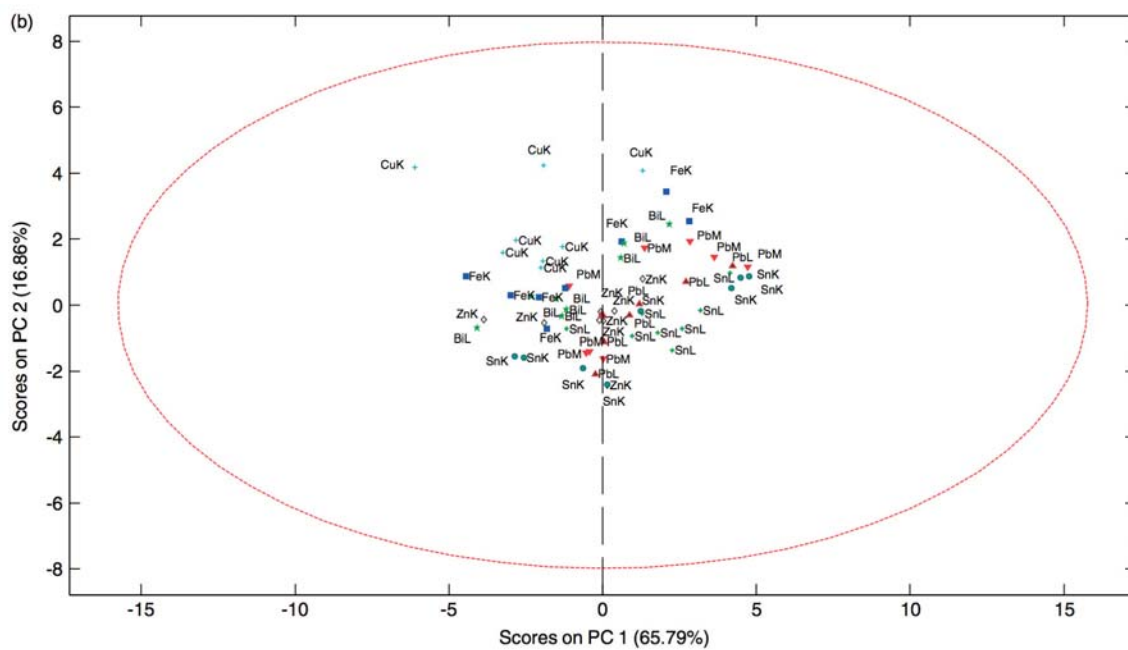


(b)

Figure 3. Molloy study PCA results for (a) SRM 2702 and (b) 2703. Inset chart shows elements with very high PC scores. Percentages on axis labels denote the amount of variance accounted for by that PC. Reproduced with permission from [13].



(a) Raw data



(b) Average of random points

Figure 4. Molloy study PCA results for SRM 1729 (a) raw data and (b) average of 100 measured locations. Reproduced with permission from [14].

material heterogeneity. However, in Figure 4b, all of the points are contained inside the ellipse, indicating that an average of 1000 random points removes perceived heterogeneities for a more accurate representation of whole sample composition.

3. Theory

3.1 Nuclear Fallout Formation

Fission Fragments and Radioactive Decay Products.

Nuclear fission typically produces two radioactive fission fragments, though in rare cases it is possible to produce three fission fragments. Collectively, this means that the fission of a nuclear weapon produces hundreds of different isotopes, which may have half-lives spanning a range from fractions of seconds to years. Each of these fragments then decays through a mass chain of radioactive daughters to a stable isotope. This process may progress through one of several types of mass chains: purely refractory (fission products that condense with lofted soil at around 1620 K), purely volatile (fission products that condense at around 1000 K), or mixed-mass, a combination of the two types of mass chains [15].

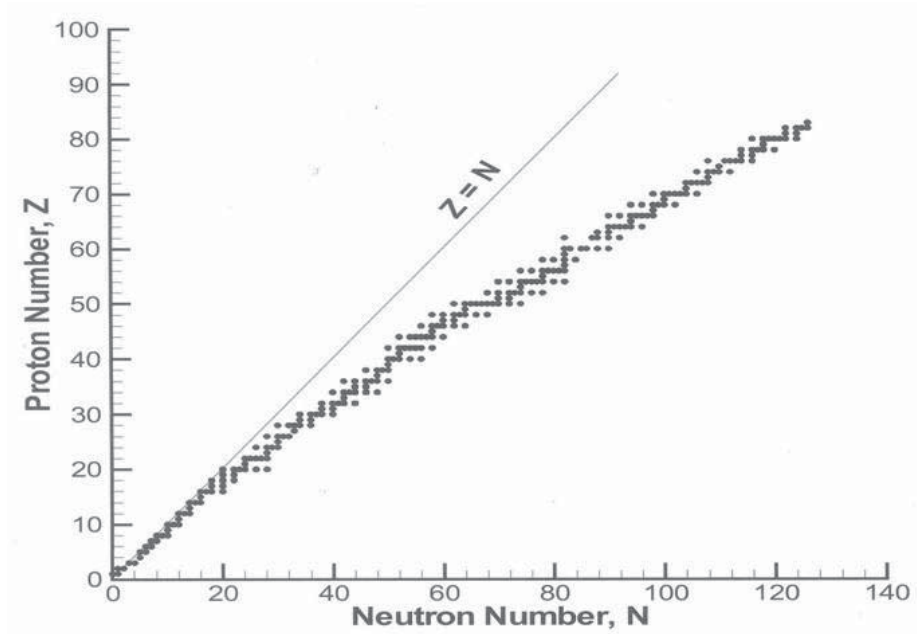


Figure 5. Chart of the Nuclides with the line of stability [16].

Radioactive decay occurs by whichever mechanism will bring the isotope closer to

the line of stability on the Chart of the Nuclides, plotted in Figure 5. Fission fragments are typically neutron-heavy, which means that they will initially appear below the line of stability and decay by beta emission. This process converts neutrons into protons and beta particles, during which the latter are ejected from the atom. Gamma rays often accompany the ejected beta particles, releasing excess energy. Alpha decay is also possible as the fission products approach their final, stable isotope. This process usually occurs closer to the end of decay chains, when beta decay may cause an isotope to overshoot the line of stability.

Fractionation.

Fractionation is every process that happens from the moment of fission that changes the materials of the weapon from their original state. This begins with fission fragment production and continues with the formation of fallout particles as they condense and rain down to earth. In the case of a surface burst (one that occurs < 90 m above ground level) [15], empirical evidence describes two main particle distributions. The larger distribution is dominated by particles that are displaced but may not be fully vaporized, accounting for 98.3% by mass of environmental material lofted into the cloud, while the smaller distribution is dominated by particles that have reformed after the original material was fully vaporized. The larger distribution will generally form more massive, heterogeneous particles and fall to the ground first, containing about 75% of the total radioactivity from the burst [15]. The smaller distribution (the only distribution present in air bursts) forms smaller, more homogeneous particles and usually falls out at a later time.

Activity can be distributed on the surface of the particles, throughout the particle volume, or both. The distribution of the activity for an individual particle is determined by its ratio of refractory to volatile elemental content. Assuming all material

is fully vaporized, refractory elements account more for volume-distributed activity due to their higher condensation temperature. They form the nucleus of the fallout particle, which, if it is light enough to remain lofted until the cloud has cooled to around 1000 K, then collects surface material consisting mostly of volatile elements, which accounts for surface-distributed activity. If the refractory fallout is too heavy to remain aloft, it falls from the debris cloud and does not exhibit significant surface-distributed activity. Surface-distributed activity with no volume-distributed component occurs when volatile fission fragments condense on lofted material that was not fully vaporized by the heat of the fireball.

3.2 X-Ray Fluorescence

X-ray fluorescence is the emission of characteristic secondary x-rays by a material that has been ionized by incident radiation. Ionizing radiation can consist of x-rays, beta particles, alpha particles, or neutrons; for this study, ionization is caused by machine-generated x-rays. Inside the microanalysis device, these primary x-rays are created in an evacuated chamber equipped with a Coolidge tube. A metal cathode is heated to produce thermal electrons, which are then accelerated across a large potential difference toward an anode, which is cooled to dissipate heat. A representative graphic of these features is shown in Figure 6. When the electrons reach the anode, which is usually angled at 120 degrees from perpendicular to the electron current, bremsstrahlung radiation and characteristic fluorescent x-rays produced by the anode material are emitted [17]. The bremsstrahlung radiation has a maximum energy equal to the energy imparted by the accelerating potential, and it exists as a continuous spectrum. By contrast, the fluorescent x-rays produced by the anode are discrete values with well-defined peaks.

The x-rays produced at the anode are collimated and directed toward the sample

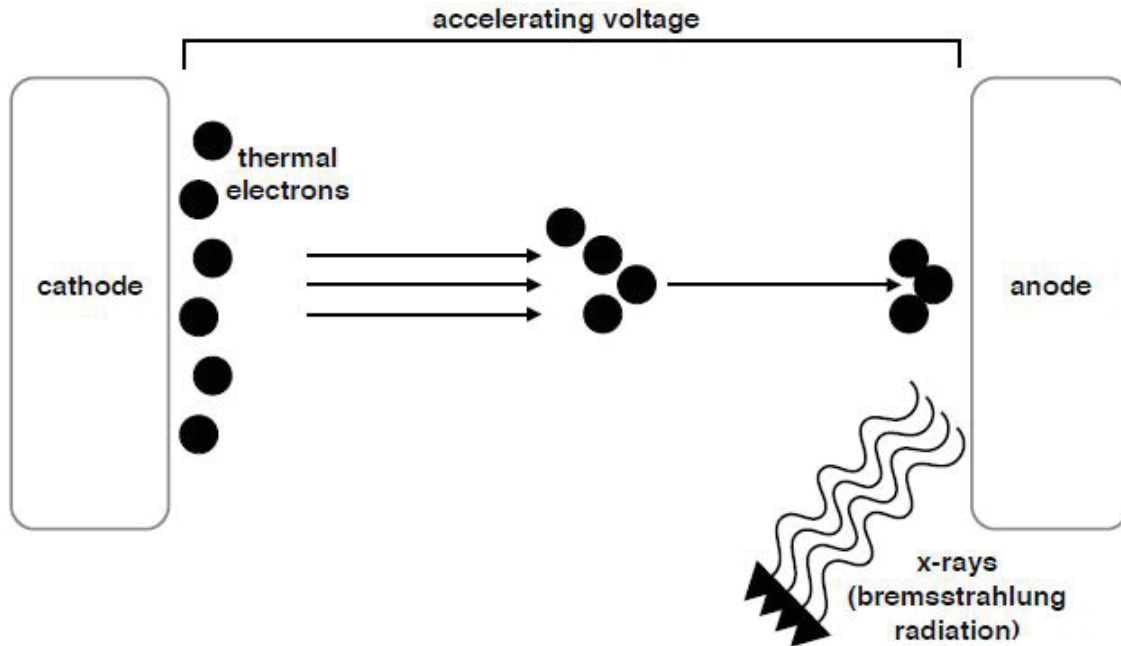


Figure 6. Generation of incident x-rays inside the XRF detector. The heated cathode emits thermal electrons, which are accelerated by a high voltage to the anode, where x-rays are generated by bremsstrahlung radiation.

as a beam with a diameter set by the user. The beam of x-rays incident upon the sample causes excitation at the atomic level. Because the energy of the incoming x-ray is greater than the ionization potential of the atom, this excitation causes the ejection of an electron. X-rays deposit enough energy to ionize electrons in the inner shells of the atom, which have less energy than the outer electrons [17].

The ejection of this inner-shell electron causes instability in the electronic structure of the atom. In order to re-establish stability, electrons in higher orbitals will cascade down to lower orbitals, filling the hole left by the inner-shell ionization. This process is illustrated in Figure 7. Because electrons in higher orbitals have more energy than those in lower orbitals, the extra energy in the cascading electron is emitted in the form of a photon. The energy of this photon is a characteristic quantity corresponding to the difference between the energies of the initial orbital and the final orbital [17]. This quantity is unique to the element in question, and each secondary

photon entering the detector is counted and sorted to quantify the amount of each element contained in the sample.

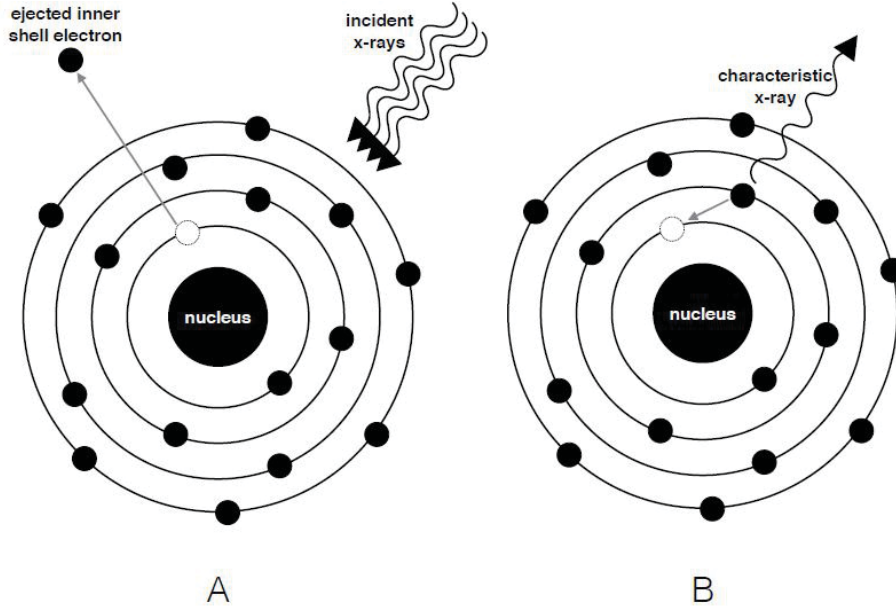


Figure 7. Physics of x-ray fluorescence at the atomic level. Incident x-rays ionize an atom, which ejects an inner-shell electron. In order to maintain electronic stability, an electron from a higher shell fills the gap, emitting a characteristic x-ray.

Each atom of an element does not undergo exactly the same ionization and transition every time. It is possible to ionize more than one of the inner shell electrons at a time, and it is also possible for different outer shell electrons to cascade down to a lower orbital to restore stability. For this reason, more than one type of transition can occur. Each releases its own characteristic amount of energy, known as a “line.”

There are three main types of transitions. These transitions are labeled K, L, or M, depending on which inner shell ejects the electron (though less common, N and O transitions may also occur [2]). For example, a K-shell electron is located in the innermost shell, so the K series line has the highest energy, with progressively lower energies resulting from progressively higher shells. Within these main types of line emissions, specific transitions are further labeled with Greek letters: alpha, beta, gamma, etc. This label corresponds to the energy shell at which the transition

started. Finally, a numerical subscript can be used to indicate the particular quantum state of the initial energy shell. Figure 8 displays several examples of different possible energy transitions and their corresponding naming conventions [18].

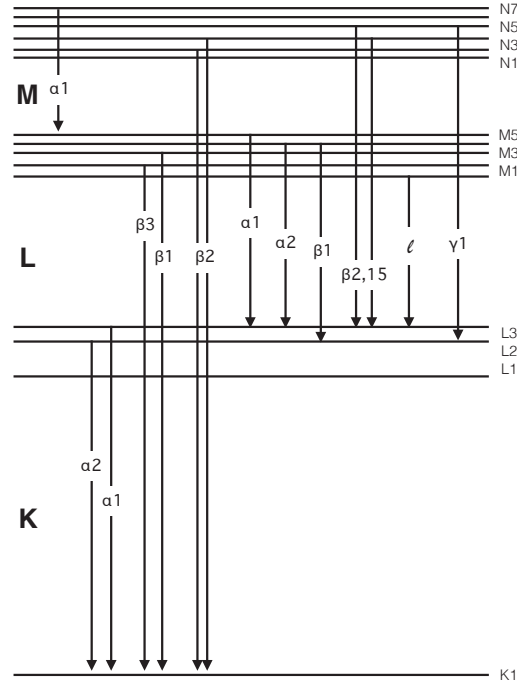


Figure 8. Transitions for x-ray emission lines.

Depending upon the composition of the sample, lower- or higher-energy primary x-rays and spectral lines can be more useful than others. Lower-energy incident x-rays and K lines are preferred for identifying lighter elements, while higher-energy incident x-rays and L lines are preferred for heavier elements.

Infinite Thickness.

In order for quantitative XRF analysis to work properly without further mathematical adjustment, the sample must be “infinitely thick” to incident x-rays. A

sample is considered infinitely thick if it is thick enough to absorb all x-rays from the primary beam, allowing maximum information return from fluorescent x-rays [19]. There are two main factors that play into this requirement: penetration depth and escape depth.

Penetration depth is the deepest point that the primary x-ray radiation beam reaches in the sample. If the sample is not thick enough, some x-rays may be transmitted through the sample to the other side. These x-rays do not interact with any atoms in the sample, which leads to partial signal loss. Escape depth is the deepest point in the sample from which fluorescent x-rays can escape and reach the detector. In most cases, once a sample is thicker than its penetration depth, it is also thicker than its escape depth.

The depth required for infinite thickness is different for every material. This value, which can vary from microns to millimeters, changes based on several factors. Higher tube voltage results in higher incident x-ray energy, which requires greater sample thickness than lower incident x-ray energy. Sample composition and density also strongly influence the depth required for infinite thickness. For a densely-packed material, infinite thickness is on the order of microns. However, a less dense material, such as a polymer, might require several millimeters of depth to qualify as infinitely thick [19].

Calculating infinite thickness first requires the mass attenuation coefficient of the material, which includes finding the atomic fraction of each element if the sample is a compound. This value can then be applied to the x-ray attenuation formula, shown in Equation (1) [20].

$$I = I_0 e^{-\frac{\mu}{\rho} \rho t} \quad (1)$$

In this equation, I is the final intensity of the x-ray, I_0 is the initial intensity, $\frac{\mu}{\rho}$

is the mass attenuation coefficient, ρ is the material density, and t is the thickness of the material. This formula can be simplified by taking the natural logarithm of both sides, yielding Equation 2.

$$\ln \left(\frac{I}{I_0} \right) = -\frac{\mu}{\rho} \rho t \quad (2)$$

For infinite thickness, $\frac{I}{I_0} = \frac{1}{e}$, so the left side of the equations gives a solution of -1 . Solving this equation for thickness gives Equation 3.

$$t_{inf} = \frac{1}{\frac{\mu}{\rho} \rho} \quad (3)$$

If the sample is a compound, the resulting value of μ for each element must be scaled by the corresponding atomic fraction of that element for accurate results [20].

If the sample does not meet the infinite thickness requirement, quantitative XRF calibrations are no longer accurate. This causes underestimating error in the data, as the XRF software interprets all measurements as coming from an infinitely thick sample.

3.3 Silicon Drift Detectors

The micro-XRF analyzer used in this study utilizes a silicon drift detector (SDD) to detect fluorescent x-rays. A SDD is the solid-state equivalent to an ionization-chamber radiation detector. It consists of a high-purity, high-resistivity n -type silicon wafer that is fully depleted through p^+ junctions integrated on both sides [21]. The energy of an incoming photon is measured based on the amount of ionization produced in the detector material. A very energetic x-ray will cause the formation of a large number of electron-hole pairs.

A strong electric transversal field is created by a series of reverse-biased rings, and

runs parallel to the surface of the device. This field causes charge carriers to drift to a small collection anode. This setup allows for higher count rates and extremely low anode capacitance, which is advantageous for energy resolution and shaping time [22]. An image of the detector device used in this study is shown in Figure 9.



Figure 9. An image of the AXAS-M silicon drift detector unit used in this study before installation.

Peltier Cooling.

Because an SDD is constructed with very high purity silicon, it allows the use of Peltier cooling instead of traditional cooling by liquid nitrogen. This mechanism works by creating a heat flux in the junction between two materials with different electron densities, typically two unique semiconductors. These materials are connected thermally in parallel and electrically in series, and joined with a thermally-conducting plate. Peltier cooling is, in essence, a solid-state heat pump that transfers heat from

one side of the device to the other in the same direction as a DC current [23]. The heated side of the junction is attached to a heat sink and maintained at room temperature, while the cooled side drops below room temperature.

Peltier cooling offers several advantages over liquid nitrogen. For the system used in this study, the Peltier cooling assembly lacks moving parts or circulating liquid, which leads to a longer life, invulnerability to leaks, smaller size, and more flexible shape than conventional refrigeration. However, it is more expensive to make, is not power efficient, and is limited to applications with relatively low heat flux, as there is a limit to the amount of heat that can be dissipated [22].

3.4 Principal Component Analysis

Principal component analysis is a statistical tool used to reduce the dimensionality of a data set, thereby revealing internal structure that may not be readily apparent [6]. The primary purpose of PCA is to allow visualization of the way that different variables work together to influence system dynamics. Other benefits include reduction in redundancy, noise, and data set size, all of which are accomplished without losing important information.

Algorithm.

The mathematics behind PCA allow for very straightforward computation. The first step is to transform the multidimensional data set into the proper form for further manipulation. This requires centering and scaling the data. Centering ensures that all of the data has a mean of zero, and is accomplished by subtracting off the mean of the data. This technique has the additional function of centering a plot of the data at the origin, which makes interpretation of results more intuitive. Scaling is accomplished by dividing values in each column by the standard deviation of the

column [24]. This results in data sets with a standard deviation of one, and ensures that data with different units are normalized.

Once the data is centered and scaled, the covariance matrix is computed. Covariance measures the degree of linear relationship between two variables —that is, how much they vary with respect to one another. Because the data is centered and scaled, the covariance matrix will have values of 1 on the main diagonal (were it not transformed this way, each value on the main diagonal would reflect the variance of the corresponding column). It is also possible to use the correlation matrix of the data for this purpose; it serves a similar function, with the added capability of standardizing the data in the same operation, which is often useful for data with different units or scales. However, because data in this study has already been centered and scaled, use of the correlation matrix is unnecessary, and might cause information to be lost.

Each matrix position associated with the covariance of two different variables will produce a large value in the case of a strong relationship, a small value for a weak relationship, and a value of zero if two variables are completely unrelated [25]. A positive covariance is one in which an increase in the value of one variable causes an increase in the value of other variable. Negative numbers represent a negative covariance, which occurs if an increase in one variable causes a decrease in the value of the other variable. If the data has dimensions $m \times n$, then the covariance matrix has dimensions $n \times n$.

Once the covariance matrix is obtained, its eigenvalues and eigenvectors are computed. This computation is likened to the Gram-Schmidt process; it creates a new series of orthogonal axes that can be used to rotate and map the data [26]. These new axes are represented by the eigenvectors. The eigenvectors are then ordered based on the decreasing value of their associated eigenvalues, or latent roots. The eigenvector

with the largest eigenvalue represents the direction of the first principal component; the large eigenvalue indicates that this is the eigenvector that best represents the behavior of the greatest portion of the data. Each succeeding eigenvector represents the direction of another, less influential principal component.

In this value-ordered state, the eigenvectors can be described as “loading coefficients.” These loading coefficients are then applied to the centered, scaled data, so that the data is expressed in terms of its principal components. These principal components are independent of one another, and progressively decrease with the amount of variance in the original data set from which they are determined. The first principal component will capture the largest percentage of the variance, the second principal component will capture the second-largest percentage of the variance, and so on. The major difference between these new axes and the original axes is that each axis now accounts for the greatest possible amount of variance in the data set, so that fewer axes are necessary to view and interpret the spread of the data. Furthermore, because the eigenvectors are computed from the covariance matrix of the original data, the PCA-transformed data points are not simply plotted as they are measured, as they would be in the xy -plane. Instead, their locations with respect to the axes and one another provide additional information about how each point relates to the other points in the set.

For scientific inquiry, a confidence interval of three standard deviations from the mean, the equivalent of 99.7% confidence, is desired for certainty in measurements. This means that all principal components contributing to a cumulative variance at or below 99.7% should be retained, if possible. However, for ease in visual representation, generally only two or three principal components are used in the creation of plots.

Underlying Assumptions.

Several criteria are necessary to determine whether PCA is a good fit for the analysis of a particular data set, because four main assumptions are made in its execution that limit its usefulness [6].

The first assumption is linearity of interaction, or the assumption that the only interaction between signal sources is additive. For multiplicative or other interactions between variables, PCA is not a good fit.

The second assumption is that the most important dynamics in the system are the ones with the largest variance. This means that principal components that account for the largest variance are preferentially chosen as the primary descriptors of the data set as a whole, while those that account for only small amounts of variance are often discarded. In this same vein, PCA also assumes that all variance is true variance, and does not account for error in the data.

The third assumption is that the data set can be adequately described solely by its mean and variance. This is because PCA is designed to use the covariance of the scaled and centered data, which only relies on these two statistical variables. Therefore, if the data does not follow a Gaussian or exponential distribution, PCA will not be as accurate.

The fourth assumption is that the principal components that result from the calculation will be orthogonal to one another. This is an effective simplifying assumption, but one that limits PCA's accuracy for many data sets. Orthogonality implies independence between components, which is not true for all distributions.

3.5 Reference Materials

Most analytical instrumentation is comparative. This means that a sample with a known composition is needed to calibrate instruments and validate results. Reference

materials act as measurement controls for these processes. In general, a reference material is defined as a material that is “sufficiently homogeneous and stable with respect to one or more specified properties, which has been established to be fit for its intended use in a measurement process” [27]. However, a generic reference material cannot be used for both calibration and validation of results in the same measurement procedure. This requires a certified or standard reference material. Certified reference materials (CRM) are a subset of reference materials that are further defined as “characterized by a metrologically valid procedure for one or more specified properties, accompanied by a certificate that provides the value of the specified property, its associated uncertainty, and a statement of metrological traceability” [27]. NIST Standard Reference Materials are CRMs that meet additional NIST-specific certification criteria. NIST lists three main purposes for the preparation and use of their SRMs:

1. To help develop accurate methods of analysis.
2. To calibrate measurement systems used to facilitate exchange of goods, institute quality control, determine performance characteristics, or measure quality assurance programs.
3. To ensure the long-term adequacy and integrity of measurement quality assurance programs.

Types of Certified Reference Materials.

CRMs can be divided into five main types as defined by the International Laboratory Accreditation Cooperation (ILAC) [28]:

1. Pure substances or chemicals
2. Standard solutions and gas mixtures

3. Matrix reference materials
4. Physico-chemical reference materials
5. Reference objects or artifacts

While the first two types are fairly self-explanatory and are characterized chiefly by their contents and purity, the latter three require further definition. Matrix reference materials are characterized by their major, minor, and trace chemical constituents, and are either prepared from matrices containing the components of interest or synthesized. The surrogate nuclear fallout debris SRM to be used in this study is an example of a synthesized matrix reference material. Physico-chemical reference materials are characterized based on chemical properties other than composition, such as melting point, viscosity, or optical density. Finally, reference objects are characterized by functional properties. These might include, but are not limited to, such qualities as taste, odor, octane number, flash point, and hardness.

Production and Certification Process.

Procedures for the production and certification of reference materials can be found in ISO Guides 34 and 35, entitled “General requirements for the competence of reference material producers” and “Reference materials —General and statistical principles for certification,” respectively. Steps involved in creating an SRM typically include: material collection or synthesis, sample preparation, homogeneity testing, stability assessment, and value assignment. Sample preparation and homogeneity testing are of particular relevance to this study.

Homogenization, which generally involves processing a sample to a fine powder or paste, is critical to sample preparation. Standards need to be processed to homogeneity on at least the scale of grams, or, in many cases, to smaller scales. However,

over-processing can have adverse effects on the constituents of some materials (for example, the breakdown of proteins in biological material), and must be avoided as well. It is also necessary that the material remain stable, which may require the addition of stabilizing agents.

Testing for homogeneity in SRMs follows typical experimental designs for each material as closely as possible, and involves repeated measurements on randomly, systematically, or stratified-randomly chosen units of multiple samples of the material. In the case of randomly chosen points, as in this study, true randomness must be maintained throughout all measurements. The main purpose of homogeneity testing is to eliminate point defects, another name for the “nugget” effects explored by Molloy and Seibert [13]. Homogeneity of the material is correlated to minimum sample size—the more homogeneous the material, the smaller the minimum sample size.

4. Experiment

4.1 Sample Preparation

NIST SRM.

The first set of samples prepared and analyzed at AFIT did not contain any nuclear material. SRM 2702 and SRM 2703 are both marine sediment standard reference materials originating from the mouth of the Baltimore Harbor in Maryland. In these two cases, the same sediment is processed differently to produce two distinct materials; 2702 is more heterogeneous, 2703 more homogeneous. Once experimental results for these materials were verified by NIST, surrogate nuclear material was prepared and analyzed. The samples analyzed in this study are “blanks,” which are doped with natural uranium (chiefly composed of U-238). At a later time, “hot” samples doped with enriched uranium (22% U-235) will be analyzed using the same techniques as this study.

SRM 4600, or SPUD-1, is a surrogate post-detonation urban debris that mimics the rubble left behind after a nuclear detonation in a modern city. It is a vitrified mixture of cement, concrete, and steel produced by the National Physical Laboratory in the United Kingdom. All reagents were mixed with a “cone and quartering” approach prior to producing batches, ensuring that the blend of materials was uniform across all samples. The glassy material was then ground and re-mixed to produce a homogeneous particle size of 150-300 microns. 100 units of 25 g each have been prepared for use, and the samples used in this study were taken from seven of these units for analysis. The most abundant elements in this blend are Ca, Al, Fe, and Si; minor and trace elements are also known.

In an effort to keep experimental methods as similar as possible, sample preparation at AFIT mirrors sample preparation demonstrated at the FBI Laboratory and

NIST [29].

SRM samples, consisting of 1 g each of either marine sediment or surrogate nuclear material in loose powder form, were pressed into briquettes using a pulled die press in a chemical hood. Attempts were made to use a pulled die press in a glove box for increased control of nuclear materials contamination, but the current glove box setup at AFIT does not allow for the efficient creation of briquettes. It should be noted that AFIT does not have a pressing die in the 30 mm size used by NIST, so a different die was used. All pressed briquettes in the AFIT study were created with a smaller die, which has a 10 mm diameter. This should not have a marked effect on experiment accuracy, though it does impose the limitation of a smaller surface area available to the micro-XRF. Briquettes were pressed under 10 tons of pressure for 3 minutes, and the die was cleaned with isopropanol between samples to control for sample cross-contamination. Examples of SRM 2702 in loose powder form and pressed briquette form are shown in Figure 10. The other two NIST SRM used in this study have similar pre-pressing and post-pressing appearances. A close-up image of the Test 1 pressed briquette of surrogate nuclear material is shown in Figure 11.



Figure 10. SRM 2702 in pressed briquette form (left) and loose powder form (right).



Figure 11. SPUD-1 Test 1 in pressed briquette form.

“Apparent heterogeneity,” often caused by surface irregularities, is of concern when producing accurate XRF data. While darker features are visible on the surface of this briquette, closer inspection confirmed that this is due to color differences in the SPUD-1 material, not by major surface irregularities.

Once each sample was created, it was marked with a unique alphanumeric for reference. Briquettes were stored in separate containers and handled as little as possible to maintain structural integrity and minimize surface defects throughout the course of the study. A list of sample IDs and masses is given in Table 1.

Historical Test Fallout Debris.

The historical fallout debris samples examined in this study were prepared for analysis by an earlier study. 50 glassy spheroids with nominal diameters of < 1 mm were mounted in two aluminum pucks, into which five rows of five 1 mm holes were drilled. The second row on each puck was offset to the right for orientation purposes.

Table 1. SPUD-1 sample identification alphanumeric and masses.

Sample ID	Initial Mass (g)
Test	1.9
12A	2.0
12B	1.6
26A	2.0
26B	1.6
40A	1.6
40B	1.5
53A	1.6
53B	1.7
58A	1.7
58B	2.1
84A	1.8
84B	1.5
94A	1.5
94B	1.4

The drilled holes were filled with epoxy, into which the particles were set. After the epoxy cured, the particles were polished level with the sample puck, which was then coated with carbon via electric sputter deposition. The original carbon sputter is no longer present on the sample pucks, but did not need to be replaced for this study because it is not necessary for micro-XRF accuracy. These samples were maintained by Lawrence Livermore National Laboratory (LLNL) in the time between AFIT studies and were shipped to Ohio from their facility in California.

4.2 Equipment

Horiba XGT-7200 X-Ray Analytical Microscope.

Once prepared, each sample was analyzed using a micro-XRF spectrometer. Measurements were conducted with the Horiba XGT-7200 X-Ray Analytical Microscope at AFIT, which is the same instrument used at the FBI Laboratory. The spectrometer and computer setup is shown in Figure 12. The Horiba micro-XRF analyzer

runs Microanalysis Suite 20a, XGT-7200 version 2.02 B01. The FBI Laboratory also utilizes an EDAX Eagle II micro-Probe for comparison purposes.

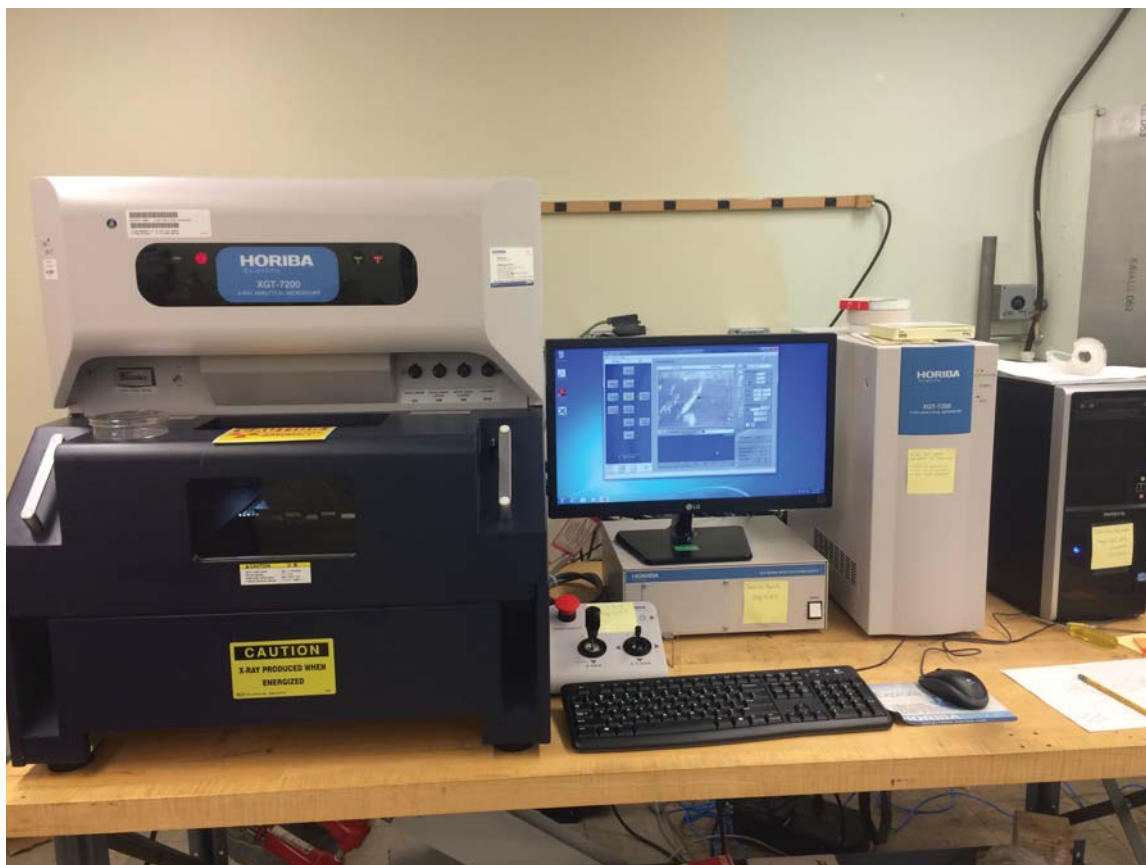


Figure 12. AFIT Horiba XGT-7200 detector setup. Left to right: detector, monitor on top of high voltage power supply, detector tower, computer.

Relevant information on the Horiba and the silicon drift detector are listed in Table 2.

Table 2. Horiba detector general information.

Descriptor	Value
Detector System Brand	AXAS-M
Serial Number	M10298
Article Number	M5T2T0-H30-M18BEV 133
SDD Part Name	Vitus H30
Resolution	137.1 ± 0.2 eV

The front panel of the spectrometer opens and slides back to expose the sample

mount, which has four removable supports so that the height of the mount can be adjusted for a sample up to 100 mm deep. For additional stability, samples can be adhered to the stage with carbon tape. This tape is of sufficiently low-Z material as to be insensitive to the micro-XRF detector, as sodium is the lightest element that can be detected with this machine and software. Once the sample is mounted, an origin search is performed and an optical image of the sample is taken for reference. A series of cameras and a set of control joysticks allow for the adjustment of sample height to the desired level. Once the front panel is closed and sealed, which can be accomplished at any point throughout this process, the sample chamber can be placed under vacuum to minimize the effects of Compton scattering and other x-ray interactions with air. For loose powder or liquid samples, a probe head equipped with a mylar window can be placed over the x-ray tube and detector window, allowing for a partial vacuum that evacuates the probe head, but not the whole chamber. The XRF software is not able to quantify element concentrations unless the measurements are taken under vacuum. Therefore, the ability to evacuate either the probe head or the chamber is essential to collecting quantitative data.

As described in the theory section of this paper, the micro-XRF generates x-rays via bremsstrahlung radiation and fluorescence of the anode, which may appear in the detector spectra. In the case of the detector used for this study, the anode is made of rhodium. Spectral lines pertaining to this element are considered background unless significant quantities are present in a given sample. The accelerating voltage used to generate the bremsstrahlung radiation spectrum for this device has three settings: 15 kV, 30 kV, and 50 kV. Spot size for the directed incident x-rays is user-selected at either 10 microns or 100 microns. Further setting options include process time, a quantity correlated to the amount of time the software takes to process each spectrum, which can be set as a number between 1 and 6 μ s; measurement time, the amount

of time the detector collects fluorescence from each spot, in seconds; and current, in milliamps, which can be set as a fixed value or an automatic, machine-varied value.

In the software's "Spectrum" function, a user may collect a series of spectra for analysis. The machine is capable of measuring a series of specific user-selected points, a fixed number of evenly-spaced points along a line, a fixed number of evenly-spaced points in a grid, or a set of points defined in an imported, comma-separated file. The number of spectra that the machine will collect independent of further input is limited to 5000. Element lines in these spectra can then be identified either manually or automatically in the "Confirm Elements" window. Once this is accomplished, elements in the spectrum are quantified by the software in the "Quant" window. The user specifies which elements should be quantified in the "Quant Setup" window. The elements in the currently selected spectrum, a combination of all processed spectra, or a fixed list of elements can all be used for this purpose. However, caution should be taken in using fixed lists. For a fixed list with only one or two elements, the software assumes that these are the only elements present in the sample, and can assign values that do not align with reality. A list with greater than five elements is preferred. However, the software will not accept a fixed list with more than twenty elements, which can require the elimination of elements deemed less interesting to the research in question.

In the software's "Mapping" function, a user may collect a raster image of a sample or region of a sample for analysis. Machine resolution (128, 256, or 512) is selected by the user, as are the sampling area, time per frame, and number of accumulations. The software then generates a SmartMap and a sum spectrum, which consists of an average of all of the spectra the detector collects over the entire sampling area. Element lines on this spectrum can be identified manually or automatically. Once this is accomplished, the "Element Maps" window is populated with raster maps that

visually display the location and intensity of all of the identified elements.

Machine Error.

One area of concern in the execution of this research is the evaluation of spectra within the Horiba software, which uses built-in libraries, calibrated to company standards, to label peaks and make decisions about the presence of different elements. All of this analysis is completed within the software, which leaves space for error that is difficult to quantify. For this reason, this study assumes that machine error holds consistent with the error quantified for the detector for 50 kV x-rays and a 100 μm spot size at the time of the detector upgrade, which occurred in August 2015. This error is valued at $\pm 1.3\%$.

Die and Press.

The pressing die used in this experiment is an International Crystal Laboratories 10-mm KBr die set. First, the die and base are connected and one anvil is inserted into the die. The powdered sample is measured and inserted on top of this anvil, and is compressed and leveled as much as possible before the second anvil is inserted. The plunger is then inserted into the die, which is placed in the briquette press so that pressure can be applied to compact the sample. The press is then used to apply the 10 tons of pressure needed to create briquettes. An image of the pieces used in this process are shown in Figure 13.

4.3 Research Approach

The NIST SRM micro-XRF analysis component of this research was divided into two phases. The first phase consisted of analysis of SRM 2702 and 2703. These results were checked by NIST for accuracy. The second phase consisted of analysis of SPUD



Figure 13. The five pieces of the die used to press the SRM material: base, die, plunger, and two anvils.

doped with depleted uranium.

Eleven fallout debris samples were analyzed with micro-XRF for comparison to existing autoradiography data.

Experimental Techniques: NIST.

SRM 2702 and SRM 2703 were examined under the same conditions and using the same procedure. For each SRM, one data collection was taken 1000 times at a single point on the surface of the sample and one data collection was taken using 1000 random points across the surface of the sample. The repeated measurements in one location are designed to account for all of the variance in the data that results from factors other than heterogeneity in the sample—for example, instrument drift. NIST recommends that this stability analysis be performed, at a minimum, between each set of four samples if measurements are taken consecutively.

The random data collection is intended to find heterogeneities in the bulk of the sample. Random point generation was facilitated by a Microsoft Excel macro built by the FBI Laboratory. This tool allows the user to input coordinates and receive a random set of points between them, which may then be uploaded into the Horiba software via a .csv file. The software then allows the user to select the top left and bottom right corner of the area of interest and distributes the random points within this area in order to accomplish the scan. For this study, the outer boundaries of the random-point area were selected so that the largest possible amount of sample surface was included.

As described above in the Equipment section, details may be adjusted on the micro-XRF in order to maximize the signal for the elements to be measured. Current settings for this experiment at AFIT are shown in Table 3. “Initial collection time” refers to the amount of time spent warming up the detector in order to mitigate data loss due to machine variance. This involves taking a set of spectra that will not be used in the final analysis.

Table 3. Horiba detector settings for SRM 2702 and 2703 with NIST-recommended parameters.

Setting	AFIT value	NIST suggested value
Spot Size	100 microns	100-500 microns
Initial Collection Time	30 minutes	20-30 minutes
Time Per Point	5 seconds	2-10 seconds
Points Per Sample	1000	1000+
Current	1.000 mA	any fixed value
X-Ray Tube Voltage	50 kV	50 kV
Process Time	4 μ s	N/A

An emphasis item for the examination of the SPUD material was to determine how many random points were necessary to compute an average that would be statistically indistinguishable from repeated measurements at a single point. For this reason, a 10,000 random-point measurement and a 10,000-point stability measurement were

taken for each sample. Machine settings for SPUD material are listed in Table 4.

Table 4. Horiba detector settings for SPUD with NIST-recommended parameters.

Setting	AFIT value	NIST suggested value
Spot Size	100 microns	100-500 microns
Initial Collection Time	30 minutes	20-30 minutes
Time Per Point	5 seconds	2-10 seconds
Points Per Sample	10000	10000
Current	1.000 mA	any fixed value
X-Ray Tube Voltage	50 kV	50 kV
Process Time	4 μ s	any fixed value

Once all of the spectra in a particular scan are collected and identified, the “Quant” portion of the software analyzes the raw spectral data and outputs the elemental composition of each 100 μ m spot. For this study, the list of elements displayed is built as a fixed list based on known sample content. Once the software has displayed the data, it is possible to copy and paste it to a file for use in other programs. For this study, the data was pasted into Microsoft Excel spreadsheets for convenience in later manipulation. Data to be mined from this spreadsheet include element, intensity, and location values.

Experimental Techniques: LLNL.

The XRF protocol for the LLNL fallout samples was based upon the process established by Monroe in the 2013 study. For each sample, both a 2500-point grid of spectra and a 128×128 -pixel SmartMap raster scan were taken over the same set of coordinates contained within a 1.280-mm square. XRF settings for this experiment are listed in Table 5.

Only SmartMaps for the most prominent elements in each raster scan were retained, as many element maps proved to be relatively homogeneous and, upon visual inspection, provided little information about the composition of fallout. For the eleven fallout sample studied here, these retained maps are those for Ca, Fe, Si, K, and Ti.

Table 5. Horiba detector settings for LLNL samples.

Setting	Spectrum	Mapping
Spot Size	100 microns	10 microns
Time Per Point	5 seconds	N/A
Time Per Frame	N/A	210 seconds
Points Per Sample	2500	128×128
Resolution	N/A	128×128
Current	1.000 mA	1.000 mA
X-Ray Tube Voltage	50 kV	50 kV
Process Time	4 μ s	6 μ s
Sample Area	1.280 mm	1.280 mm

Additionally, an Al map for a whole-disk raster scan, taken with the same disk orientation as the individual sample maps, is retained for image alignment purposes. Al is chosen for this purpose because the sample disks are housed in an aluminum coating, which causes the edges of each sample to be clearly identifiable on the map.

Computational Techniques.

NIST.

A truly homogeneous sample should produce a normal distribution of intensities for each element measured. Heterogeneity causes changes to this distribution. For this reason, statistical analysis of each set of spectra is the first step in data analysis. Average intensity, standard deviation, relative standard deviation, counting statistical error, skew, and kurtosis for all collected points are computed for each element. Relative standard deviation (RSD), also known as the coefficient of variation, is a standardized measure of dispersion of a distribution, and is computed as shown in Equation 4, where σ is the standard deviation and μ is the average intensity. Counting statistical deviation (CSD) accounts for sampling error and is computed as shown in Equation 5. For this experiment, N is obtained by multiplying the count rate, which has units of $\frac{\text{counts}}{\text{s}}$, by five, because each measurement was taken for five seconds.

As referenced to the normal distribution, skewness is a measure of the asymmetry of a distribution, and kurtosis is a measure of the flatness of the distribution peak. In combination, these values describe the shape of the elemental distributions in the sample. Additional information, including the atomic number and line energy detected for each element, are also used to conduct PCA on the data set.

$$RSD = \frac{\sigma}{\mu} \quad (4)$$

$$CSD = \sqrt{N} \quad (5)$$

The PCA code for this study follows the PCA algorithm established in the Theory section of this document and was written in MATLAB version R2015a. It transforms data, produces principal components, and calculates confidence ellipses and the variance attributed to each principal component. Two plots are then produced. The first is a MATLAB-generated biplot that plots the first principal component against the second, overlaying data points with vectors that illustrate the influence that different data variables have on the spread of the data. The second is a scatter plot that is analogous to the scatter plot produced on the biplot, but here is color-coded or labeled to differentiate between different categories of data (for example, to distinguish between different elements in a sample, or between different sample types on the same plot). The scatter plot also includes confidence ellipses for one-, two-, and three-sigma from the mean of each principal component for measurement certainty purposes.

LLNL.

Intensity values for all of the elements found in all eleven fallout samples are mined from the XRF data to create an array. Each column represents an element and each row represents an observation. The autoradiography image from the sample disk used (either Disk 1 or Disk 2) is then aligned rotationally with the raster scan Al map and the optical microscopy image in Adobe Photoshop. Once the sample locations on the Al map are properly aligned to the sample locations on the autoradiography image, other raster maps are much easier to align, as they can be rotated at the same angle as the Al map. Once the autoradiography image and each corresponding SmartMap are properly aligned, the autoradiography image is cropped to the same area over which the elemental maps and the grid of 2500 spectra were collected. The dimensions of the cropped autoradiography image are 50×50 pixels for a total of 2500 pixels per image, so that each pixel aligns as closely as possible to the location of each of the 2500 spectra.

Once an autoradiography image is acquired for each sample, it is loaded into a MATLAB function that reads the digital image and outputs a 50×50 array of pixel intensity values, valued from 1 to 255. A value of 1 represents a fully black pixel, while a value of 255 represents a fully white pixel. These values are then divided by 255 to produce fractional values, which are then subtracted from 1, so that the darkest pixels now have values approaching 1 and the lightest pixels have values approaching 0. The 50×50 array is then reshaped into a single column vector by turning each row into a column and concatenating it beneath the values from the previous row. Once this is accomplished for all of the samples in question, the vectors are concatenated vertically and normalized on a scale from zero to one, so that the activity in different samples can be compared on the same scale. These activity-based scaling factors are then applied to the element intensity values from each corresponding spectrum, so that

the intensities associated with the most activity are scaled highest, while intensities associated with the least activity are scaled lowest. PCA is then performed on the data, which is plotted in a similar manner to the NIST data.

5. Results: NIST SRM

5.1 Micro-XRF Results

SRM 2702 and 2703.

The pressed pellet samples of SRM 2702 and SRM 2703 were analyzed following the recent upgrade of the Horiba micro-XRF to a silicon drift detector. Sets of spectra, consisting of 1000 random points and 1000 stability measurements, were taken and averaged for each. An example spectrum from this set of measurements is shown in Figure 14.

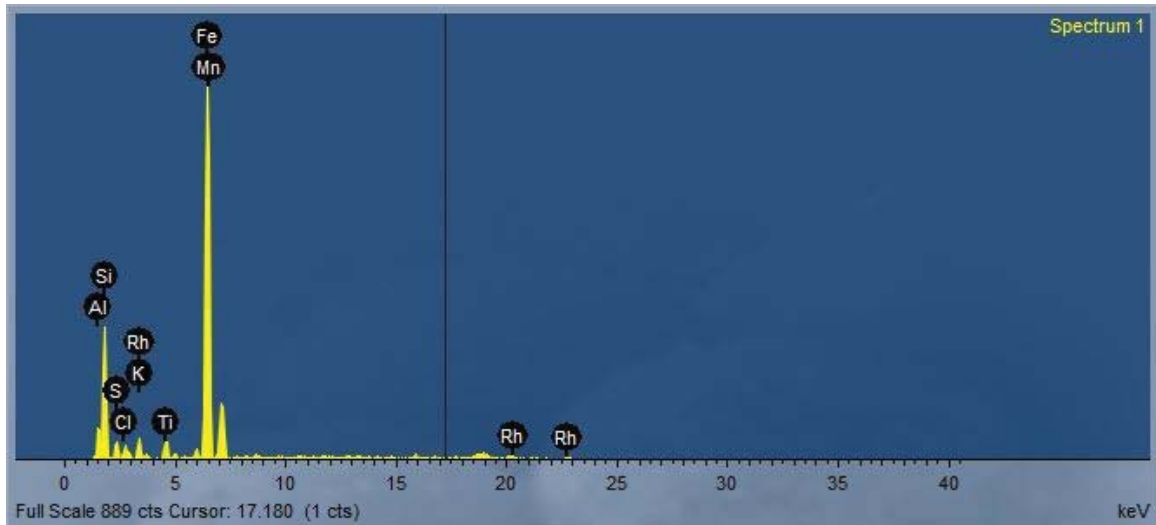


Figure 14. An auto-ID sample spectrum from a data collection on SRM 2702. Peak values represent counts at each energy and are labeled with the element line to which they correspond.

The automatic-identification software analysis of these spectra used a NIST- recommended fixed list of 20 elements to quantify the data: Mg, Al, Si, P, S, K, Ca, Ti, V, Cr, Mn, Fe, Ni, Cu, Zn, Rb, Sr, Cs, Ba, and Pb. These include 15 of the 25 certified elements known to be present in SRM 2702, as well as 3 of the 8 reference elements and 1 of the 12 information elements [30]. Si is the only element on the list not included on the SRM certificate. Reference elements and information elements

are given as NIST’s best estimate and are on the certificate chiefly to inform curious parties, with the caveat that values may be inconsistent across methods. Therefore, NIST values for Ca, Mg, Cs, S, and Si, which is a major component of these samples but lacks a certificate value, may not always be reflective of true sample content.

Average values and standard deviation of mass percentage for each of the 20 elements for stability measurements of 2702 and 2703 are shown in Table 6 and Table 7. The tables also contain the NIST certificate mass percentage and error. Mass percentages for the AFIT measurements were not used to compute error, as the use of a fixed list in quantifying element concentrations does not allow for the presence of elements outside of those on the list. This forces the 20-element list to account for 100% of the mass of a sample, which is not realistic. Other trace elements exist in the samples, as do lighter elements that cannot be detected with micro-XRF. These elements that are present but not on the list are either identified incorrectly or discounted altogether, causing calculated mass percentages for elements on the list to be artificially high. Therefore, the mass percentage values given in Tables 6 and 7 are for reference only. This shortcoming of the software package is the reason that data sent to NIST from AFIT is composed of intensity values rather than mass fractions. These intensity values are presented in Tables 8 and 9.

Table 6. Quantified XRF results and comparison to NIST values for SRM 2702 [30]. Values are given as mass percentages. Values given as N/A are not given on the NIST certificate.

Element	AFIT Value	AFIT Std Dev	NIST Value	NIST Error
Mg	1.287	0.613	0.99	0.07
Al	14.491	0.857	8.41	0.22
Si	50.337	2.017	N/A	N/A
P	0.434	0.197	0.1552	0.0066
S	2.706	0.657	1.5	N/A
K	5.155	0.487	2.054	0.0072
Ca	0.908	0.360	0.340	0.02
Ti	2.086	0.510	0.884	0.082
V	0.132	0.072	0.03576	0.00092
Cr	0.092	0.050	0.0352	0.0022
Mn	0.449	0.079	0.1757	0.0058
Fe	21.273	1.324	7.91	0.24
Ni	0.017	0.025	0.00754	0.00015
Cu	0.047	0.037	0.01177	0.00056
Zn	0.146	0.051	0.04853	0.00042
Rb	0.029	0.027	0.01277	0.00088
Sr	0.025	0.025	0.01197	0.0003
Cs	0.148	0.116	0.00071	N/A
Ba	0.179	0.214	0.03974	0.00032
Pb	0.059	0.059	0.01328	0.00011

Table 7. Quantified XRF results and comparison to NIST values for SRM 2703 [31]. Values are given as mass percentages. Values given as N/A are not given on the NIST certificate.

Element	AFIT Value	AFIT Std Dev	NIST Value	NIST Error
Mg	1.161	0.544	1	N/A
Al	13.548	0.668	8.33	0.22
Si	51.304	0.919	N/A	N/A
P	0.381	0.181	0.16	N/A
S	2.933	0.367	N/A	N/A
K	4.956	0.380	2.08	0.24
Ca	0.805	0.163	0.31	0.12
Ti	2.061	0.166	0.88	0.046
V	0.125	0.071	0.036	0.0013
Cr	0.093	0.043	N/A	N/A
Mn	0.444	0.076	0.1734	0.0048
Fe	21.540	0.609	7.38	0.32
Ni	0.016	0.024	0.0075	N/A
Cu	0.048	0.040	0.012	0.0015
Zn	0.144	0.051	0.048	0.0022
Rb	0.028	0.026	0.013	0.0011
Sr	0.025	0.026	0.0118	0.0018
Cs	0.160	0.119	0.00077	0.00007
Ba	0.166	0.222	0.0416	0.0032
Pb	0.061	0.063	0.013	0.0011

Table 8. Quantified XRF results for SRM 2702 [30]. AFIT values are intensities (c/s/mA).

Element	Avg Intensity	Std Deviation
Mg	3.060	1.499
Al	114.17	7.655
Si	570.092	31.687
P	5.069	2.322
S	67.617	17.166
K	74.550	7.410
Ca	18.156	7.373
Ti	78.852	20.316
V	6.293	3.450
Cr	4.776	2.568
Mn	24.263	4.329
Fe	1236.546	85.972
Ni	0.719	1.094
Cu	2.083	1.648
Zn	7.025	2.461
Rb	1.238	1.158
Sr	0.926	0.929
Cs	1.297	1.026
Ba	1.673	2.013
Pb	1.008	1.011

Table 9. Quantified XRF results for SRM 2703 [31]. AFIT values are intensities (c/s/mA).

Element	Avg Intensity	Std Deviation
Mg	2.528	1.215
Al	98.233	5.902
Si	542.061	17.824
P	4.090	1.956
S	67.231	8.703
K	65.744	5.263
Ca	14.809	3.019
Ti	71.770	5.706
V	5.484	3.111
Cr	4.434	2.047
Mn	22.157	3.78
Fe	1152.938	31.563
Ni	0.630	0.939
Cu	1.958	1.605
Zn	6.381	2.250
Rb	1.088	1.027
Sr	0.842	0.895
Cs	1.296	0.965
Ba	1.438	1.932
Pb	0.951	0.984

SPUD Blanks.

The pressed pellet samples of SRM 4600/SPUD-1 were analyzed after the results from SRM 2702 and 2703 were reviewed by NIST. Sets of spectra, consisting of 10,000 random points and 10,000 stability measurements, were taken and averaged for each. An example spectrum from this set of measurements is shown in Figure 15.

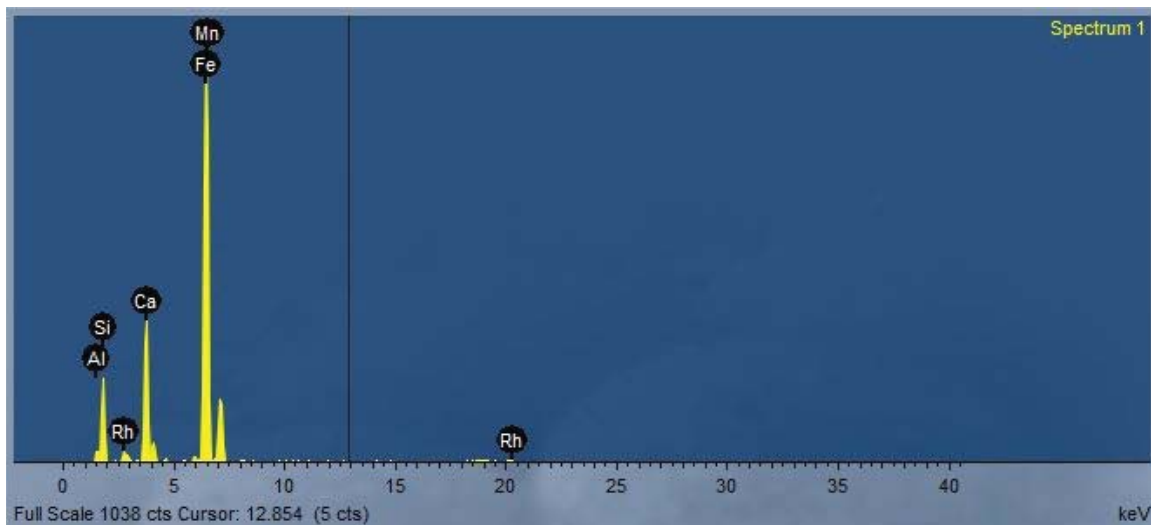


Figure 15. An auto-ID sample spectrum from a data collection on SPUD-1. Peak values represent counts at each energy and are labeled with the element line to which they correspond.

The automatic-identification software analysis of these spectra also used a NIST-recommended fixed list of 20 elements to quantify the data. This list of elements is different from the one used for SRM 2702 and 2703. Element values acquired for SPUD were: Na, Mg, Al, Si, P, K, Ca, Ti, V, Cr, Mn, Fe, Co, Ni, Cu, Sr, Zr, Nb, Mo, and U.

Average values and standard deviation of signal intensity for each of the 20 elements quantified for SPUD-1 Test 1 are shown in Table 10. At the current time, this table is only representative of measurements taken at AFIT, and error related to this particular micro-XRF spectrometer.

Table 10. Quantified XRF results for SPUD-1 Test 1. Values are intensities (c/s/mA).

Element	Avg Intensity	Std Deviation
Na	0.173	0.223
Mg	0.608	0.538
Al	52.348	3.877
Si	350.007	9.747
P	0.854	0.827
K	9.009	2.921
Ca	761.448	23.624
Ti	6.662	2.124
V	1.827	1.493
Cr	3.920	1.984
Mn	22.865	3.510
Fe	2554.253	44.013
Co	4.308	3.557
Ni	4.091	1.652
Cu	3.941	1.807
Sr	4.324	1.889
Zr	0.096	0.334
Nb	0.668	0.896
Mo	1.974	1.354
U	0.237	0.538

At this time, no true comparison to NIST values can be made, as an SRM certificate has not yet been completed.

5.2 Principal Component Analysis

Test Data Set.

Before PCA was conducted on data from SRM 2702, SRM 2703, or any synthetic nuclear material, successful PCA code development was demonstrated via the use of Ronald Fisher's 1936 *Iris* flower data set. This is a multivariate data set that is commonly used as a sample set in the introduction of statistical data analysis methods. 50 samples each of three different species of iris were measured for sepal length, sepal width, petal length, and petal width. PCA can be used to discriminate among them, showing that it is possible to both establish a pattern of identification between species and determine which factors contribute the most to their differences.

The four PCs generated for this data are created by multiplying the centered and scaled flower measurement values with the eigenvectors of the data set's covariance matrix. Before this step is performed, the eigenvectors are ordered based on decreasing value of their corresponding eigenvalues. A relatively high eigenvalue indicates that an eigenvector better represents the covariance relationships of the whole data set. Therefore, the first two PCs are the dimensions that contain the most information. Plotting these two PCs as two axes of an orthonormal basis allows efficient representation of the way that a change in a combination of the original descriptive variables influences the relationship between data points. In this case, the PCA results show how petal width, petal length, sepal width, and sepal length collectively describe each flower in comparison to every other flower in the data set. The results of PCA analysis on *Iris* are shown in Figures 16 and 17. Figure 16 illustrates the influence of each of the four measurements on the first two principal components (PCs). Figure 17 allows a color-coded visualization of the variance in the three different species.

These results make several suggestions about the data set. From the biplot vectors, which visually represent the loading coefficients that define the relative influence of

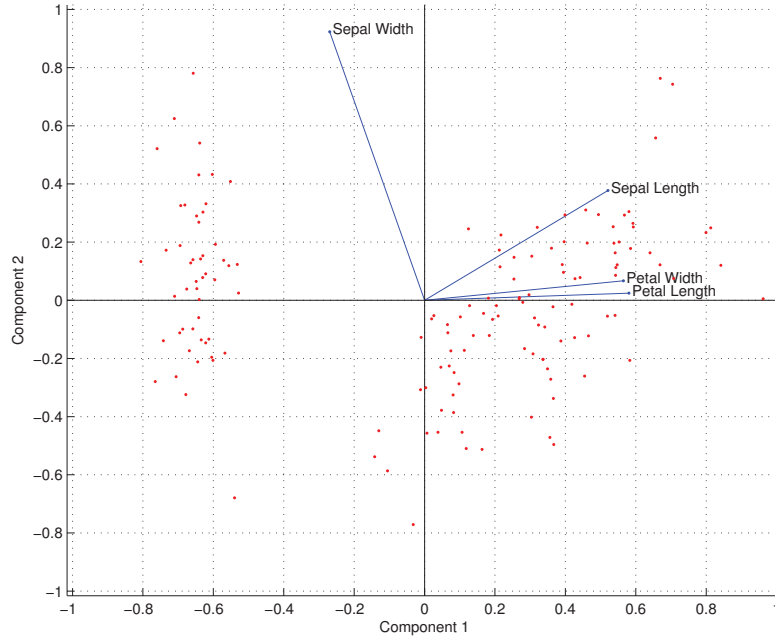


Figure 16. Biplot of the first and second principal components of Fisher's Iris data.

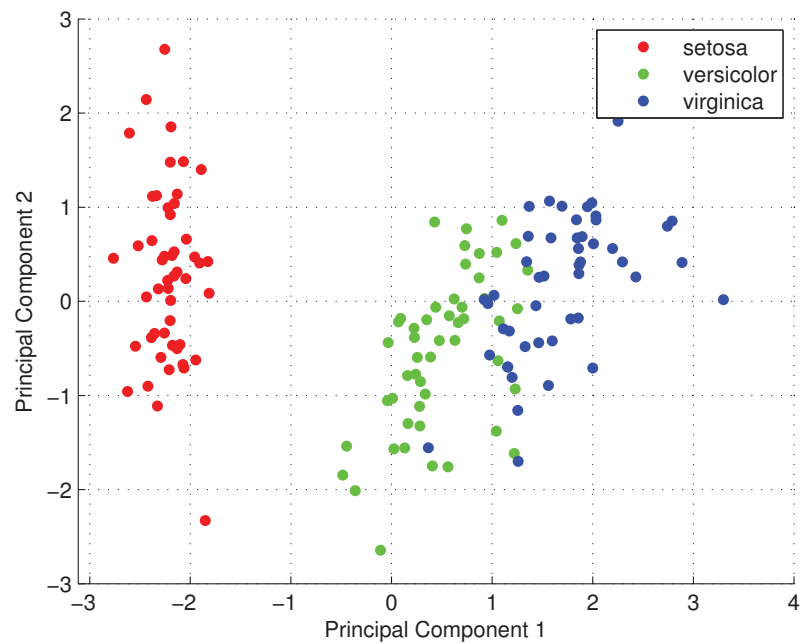


Figure 17. Scatter plot, color-coded by species, of the first and second principal components of Fisher's Iris data.

each of the original flower measurements, it can be seen that petal length and, to a comparable but slightly lesser degree, petal width, strongly influence the first principal component in the positive direction. They are significant vectors with direction of greatest change along the x-axis. Therefore, these two factors most strongly influence the horizontal spread of the data.

The species-dependent color coding in the scatter plot indicates that different species of iris are most clearly separated along the first principal component; this leads to the conclusion that it is most prudent to distinguish between iris species by comparing the length and width of their flower petals. *Setosa*, on average, has smaller average petal length and width than *versicolor*, which in turn has smaller average petal length and width than *virginica*. Sepal width most strongly influences the second principal component, accounting for the largest variance in the vertical spread of the data. This is less useful information outside of a few cases in the overlap between *versicolor* and *virginica*, and accounts in general for more of the variance within a species than it does for the variance between species. These conclusions have been compared to existing analyses of this test data set [32], and are found to be accurate, indicating a successful PCA code implementation.

SRM 2702 and 2703.

The goal in conducting PCA on SRM 2702 and 2703 was to confirm that 2702 is measured to be more heterogeneous than 2703. Here, the statistics described in Section 4.3 of this document were used as descriptors for the intensity distribution of each element measured, analogous to the different measurements used to describe Fisher’s irises. Collectively, these statistics described the shape of the distribution for each element in the sample. In this way, PCA was used to identify sources of heterogeneity in the sample by finding the element intensity distributions that differed

most significantly from the desired normal distribution.

The first two principal components were plotted to visually map the spread of the data. Figures 18 - 21 display the biplot and scatter plot results for both stability and random measurements for these two materials. Each scatter plot point represents a different intensity distribution, and is labeled with the name of the corresponding element. The three red confidence ellipses on each scatter plot represent (from the innermost to the outermost) one, two, and three standard deviations from the mean of the transformed data. For a value more than three standard deviations from the mean, statistically significant differences are found to exist between the measured element intensity distribution and a normal distribution. When this occurs, it can be said with 99.7% certainty that this element produces nugget effects in the material, which may cause measured results to differ from the values found on the SRM certificate. Likewise, those elements within the $3\text{-}\sigma$ confidence ellipse do not show significant heterogeneity, and are therefore considered adequately homogeneous.

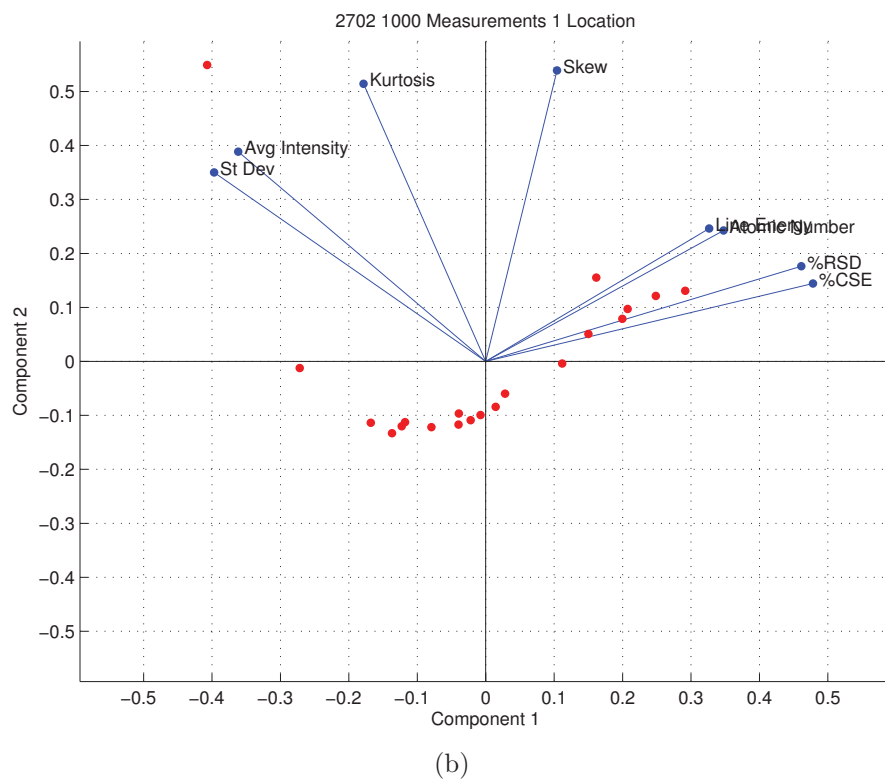
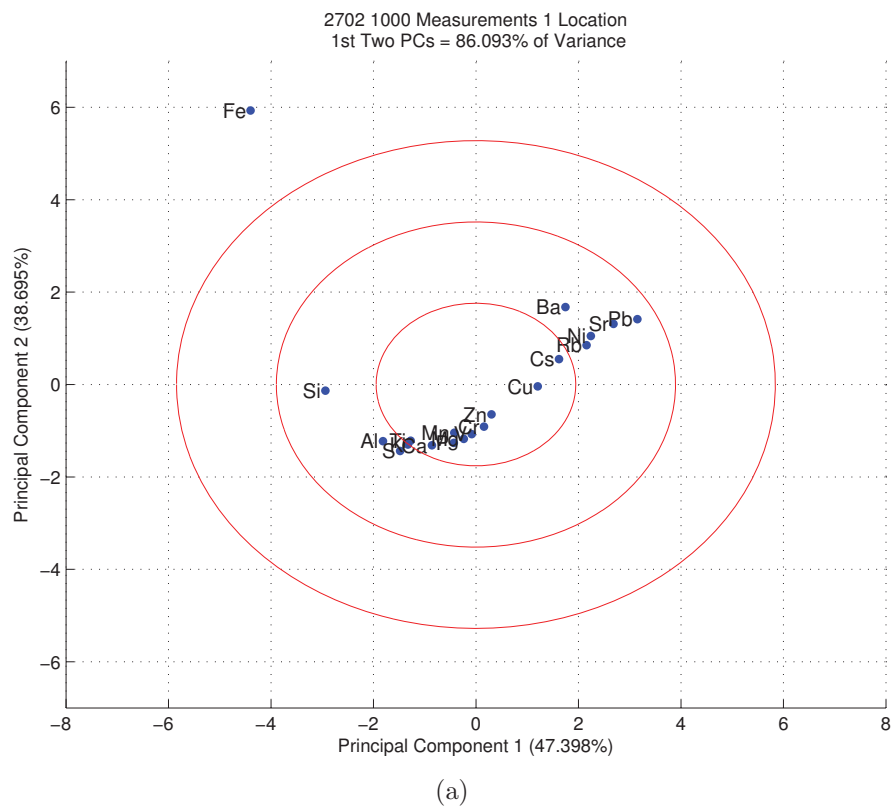


Figure 18. PCA results for stability measurements on SRM 2702.

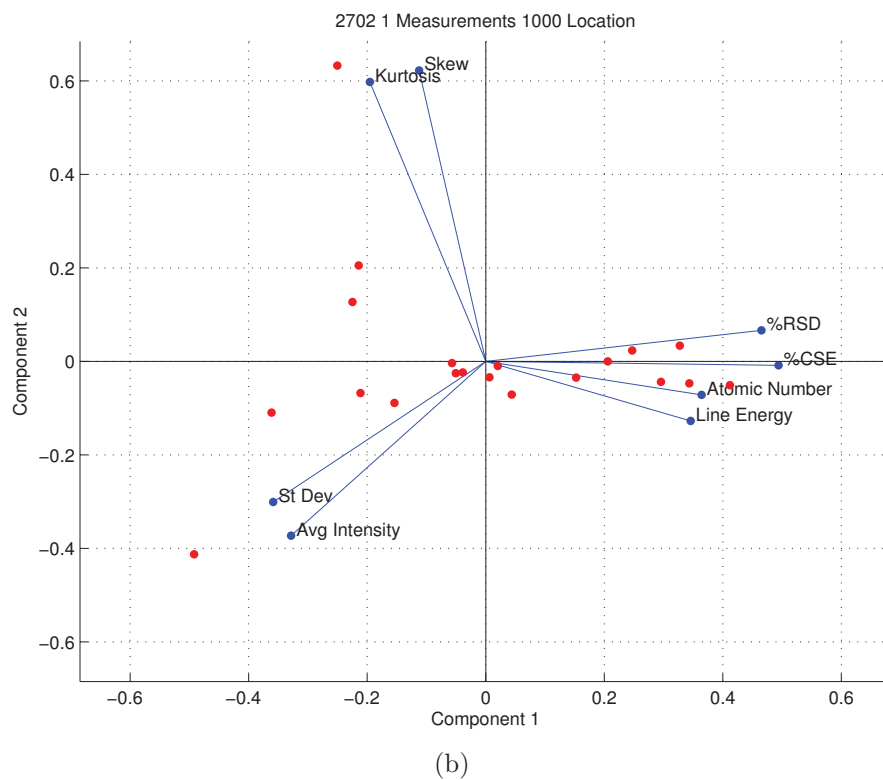
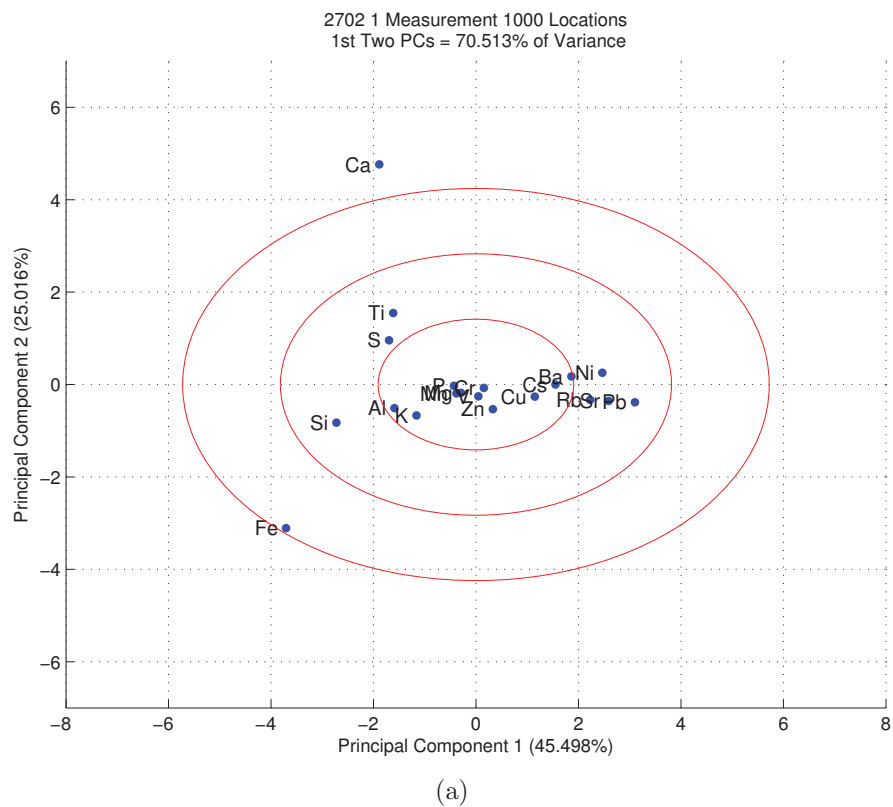


Figure 19. PCA results for random measurements on SRM 2702.

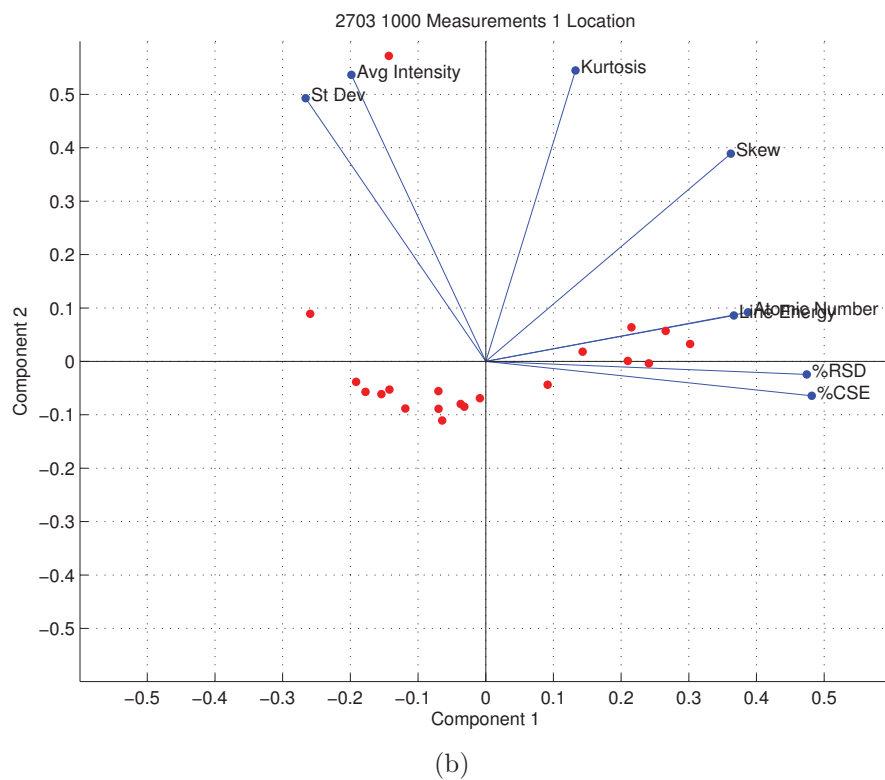
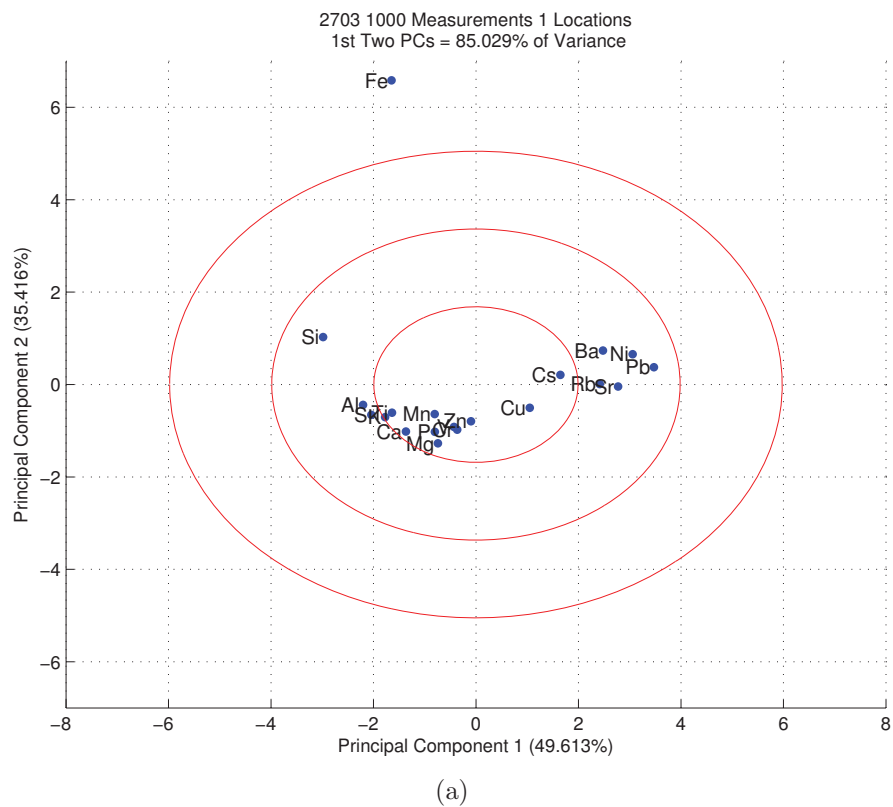


Figure 20. PCA results for stability measurements on SRM 2703.

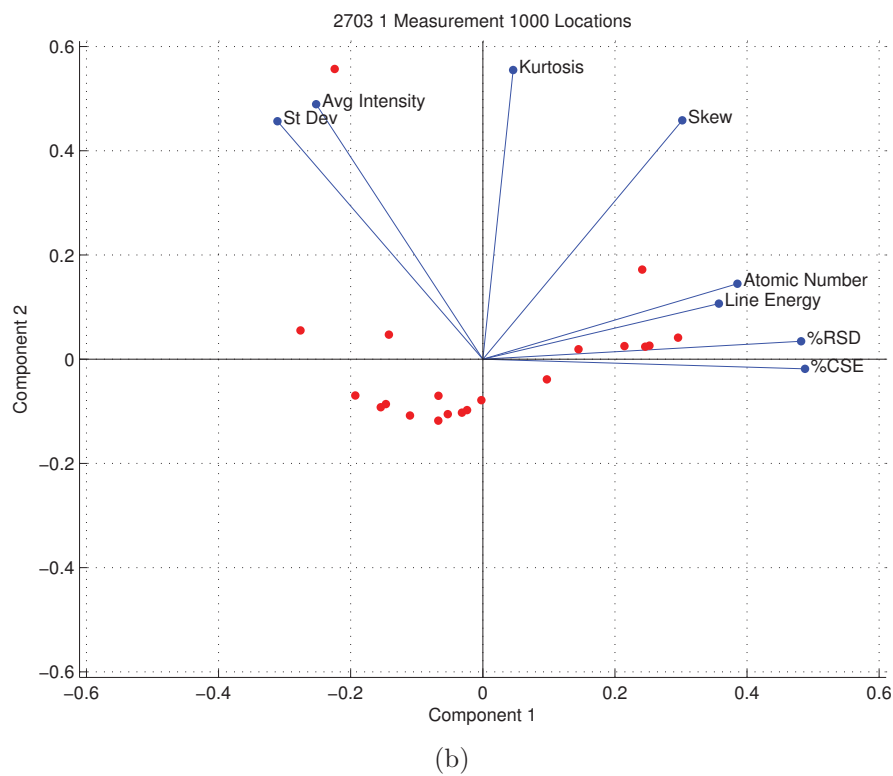
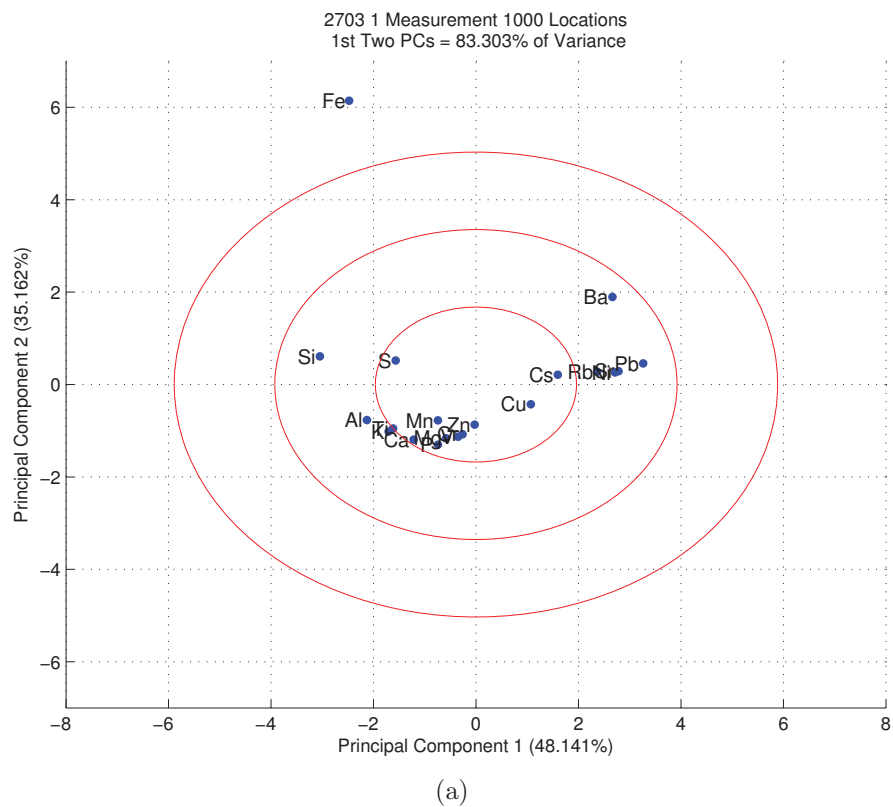


Figure 21. PCA results for random measurements on SRM 2703.

The scatter plots produced for the two SRM materials indicate that 1000 measurements in one location give a more homogenous result than 1000 measurements in unique, randomly determined locations. For SRM 2702, this accounts for a 15% difference in variance in the first two principal components. For SRM 2703, the difference between the random point collection and the stability analysis only accounts for a 2% difference, but this is largely because 2703 is more homogeneous to begin with. The first two PCs account for 13% more of the variance in 1000 random points on 2703 than on 2702 when samples are prepared and analyzed the same way. Because a larger amount of the variance in a sample can be explained with the same number of principal components for 2703 than 2702, and because the spread of the data is less pronounced in 2703, 2703 is more homogeneous than 2702.

Analysis of the biplots gives more information about the different factors that influence the first two principal components. Relative standard deviation (RSD), counting statistical error (CSE), atomic number, and line energy have the strongest influence on the first principal component in all four cases, also appearing to account for the direction of greatest data association. Kurtosis has the most consistent influence on the second principal component.

Figures 18b and 19b also illustrate the interdependence of certain descriptors. For instance, the influence vectors for standard deviation and average intensity often fall close to one another on these plots, indicating that both descriptors influence the data in the same direction. This trend is explained by similarities in the aspects of the data that these values describe. Average intensity and standard deviation are both related to signal strength; skew and kurtosis both describe the intensity distribution's curvature and relationship to the normal distribution. Atomic number and line energy both describe qualities of the particular elements. These qualities of the descriptors further aid in the explanation of the spread of the data and any outliers that may

occur.

For 2702, the stability measurement indicates nugget effects for Fe, which is found outside the $3\text{-}\sigma$ confidence ellipse in Figure 18. Because this is a stability measurement, this result is not necessarily indicative of variance in the contents of the sample, as all of the averaged measurements were taken at the same location. Instead, this is more likely caused by an unknown machine or environmental property. The biplot in this figure shows that average intensity and standard deviation have the strongest influence on the location of the Fe data point, which may indicate that the reason for the distribution's deviation from normal is the production of a particularly intense signal. This can be confirmed through study of the mass percent numbers generated for this set of spectra; Fe content is consistently evaluated as three times higher than the certificate value. However, Fe does not appear to produce nugget effects in the random measurement for 2702. In this case, the average of a series of random measurements indicates adequate homogeneity for this element, suggesting that nugget effects may not actually be significant. However, Ca, which exhibits no heterogeneous behavior in the stability measurement, is found to have nuggets in the random measurement; these nuggets are therefore far more likely to be found in other measurements.

Heterogeneities in Fe are also found in the stability measurement for 2703. Again, this is shown in the biplot to be most strongly influenced by the values for average intensity and standard deviation. Because this behavior is consistent between the stability and random measurements for 2703, the nugget effect found for this SRM is deemed most likely to be the result of a factor other than actual sample variance. It is possible that the steel die used to press briquettes for this study leaves behind additional Fe on the surface of the samples, which in turn causes Fe to appear more plentiful under examination. Further investigation is needed in this area.

Infinite Thickness and Minimum Sample Size.

Minimum sample size was computed through a study of infinite thickness, the formula for which is given in the theory section of this paper. Mass attenuation coefficients and densities for different elements were obtained from NIST [33] and Lawrence Berkeley National Laboratory [34] value tables. This resulted in an infinite thickness depth of 3.743 mm for SRM 2702 and 3.701 mm for SRM 2703. This thickness was then used as the depth component in the volume of a pressed briquette, with a 10 mm pellet radius corresponding to the 10 mm die used in this study. The resulting minimum sample mass was 0.814 g for 2702 and 0.810 g for 2703.

Varying Measurement Time.

SRM 2702 was measured for 100 points on the same evenly spaced grid for 5, 10, 15, 20, 25, and 30 seconds per point. Statistical information was collected for each set of 100 spectra and then grouped by measurement time and plotted. Results are shown in Figure 22.

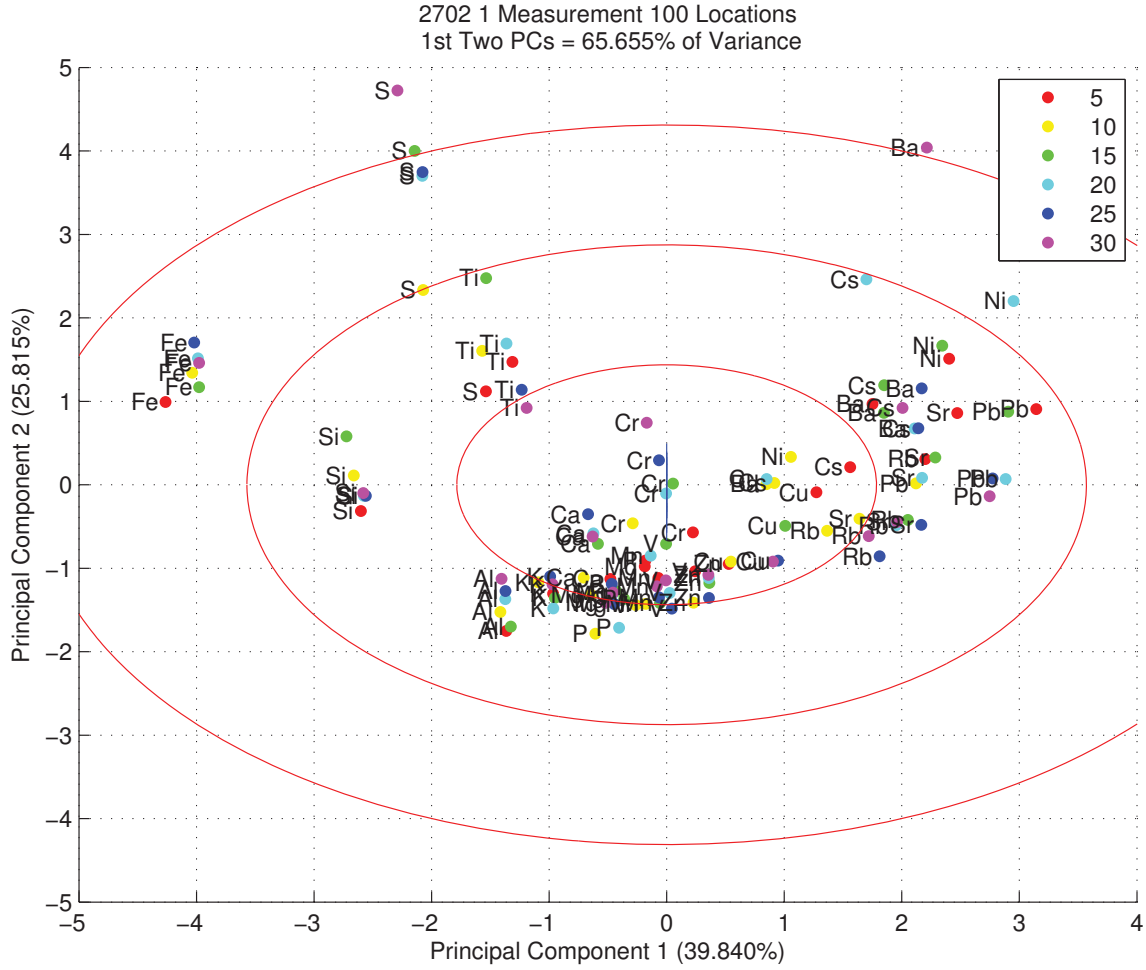


Figure 22. Scatter plot, with element labels and color-coded by measurement time, of six different tests of the same 100 points using measurement times of 5, 10, 15, 20, 25, and 30 seconds.

The locations of the elements, grouped by time, on the scatter plot gives information as to whether certain elements, if measured for longer than five seconds, tend to demonstrate more heterogeneity due to better signal values. The scatter plot indicates that, in particular, barium, nickel, and sulfur show significantly more variance at longer measurement times. Of these three elements, only sulfur has a significant presence in the sample. Therefore, it is considered acceptable for this study to keep measurement time at five seconds instead of increasing to a longer period of time.

SPUD Blanks.

The goal in conducting PCA on the SPUD-1 material was to determine whether there are any notable nugget effects in the medium, because nugget effects are undesirable for method testing purposes. The same PCA method and descriptors used on 2702 and 2703 were also used on the SPUD data. The results of the PCA conducted on random and stability measurements of Test 1 and 58B are shown in Figures 23 - 26.

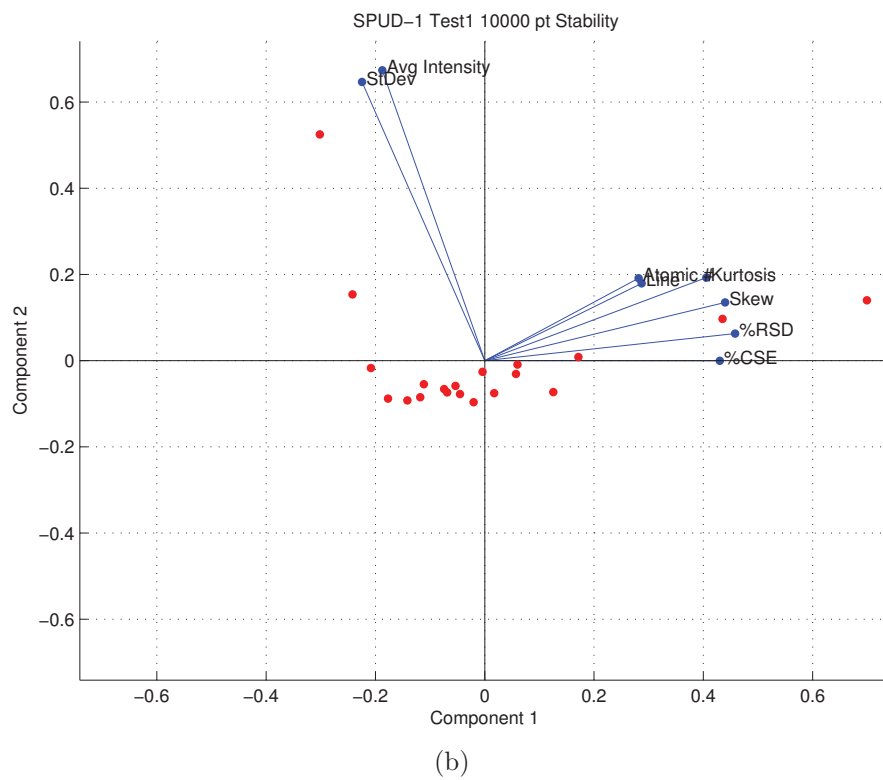
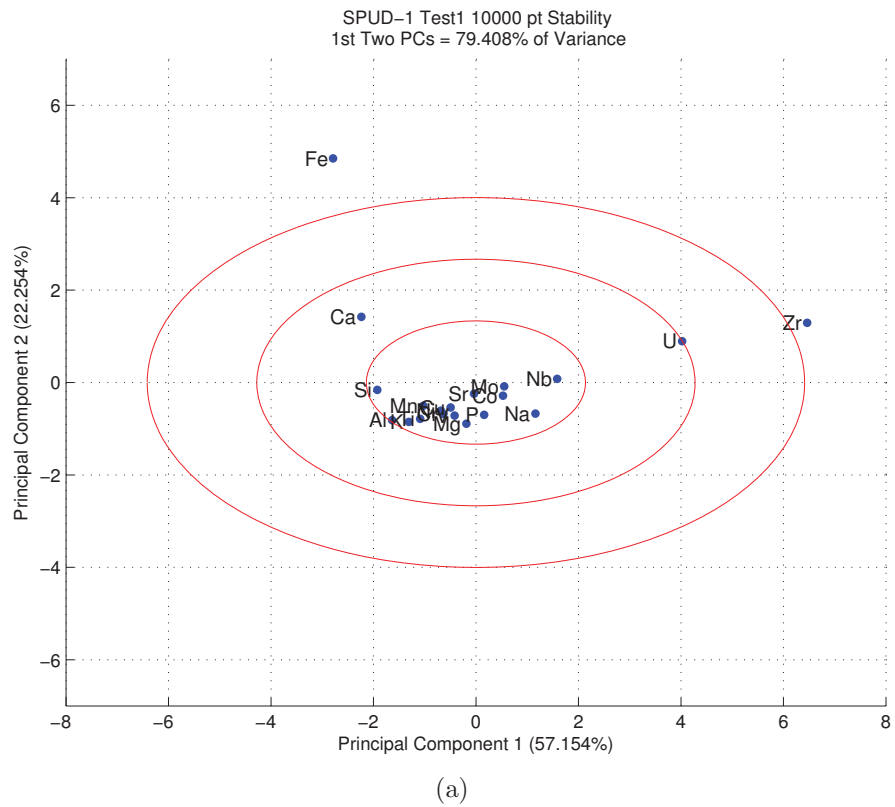


Figure 23. PCA results for stability measurements on SPUD-1 Test 1.

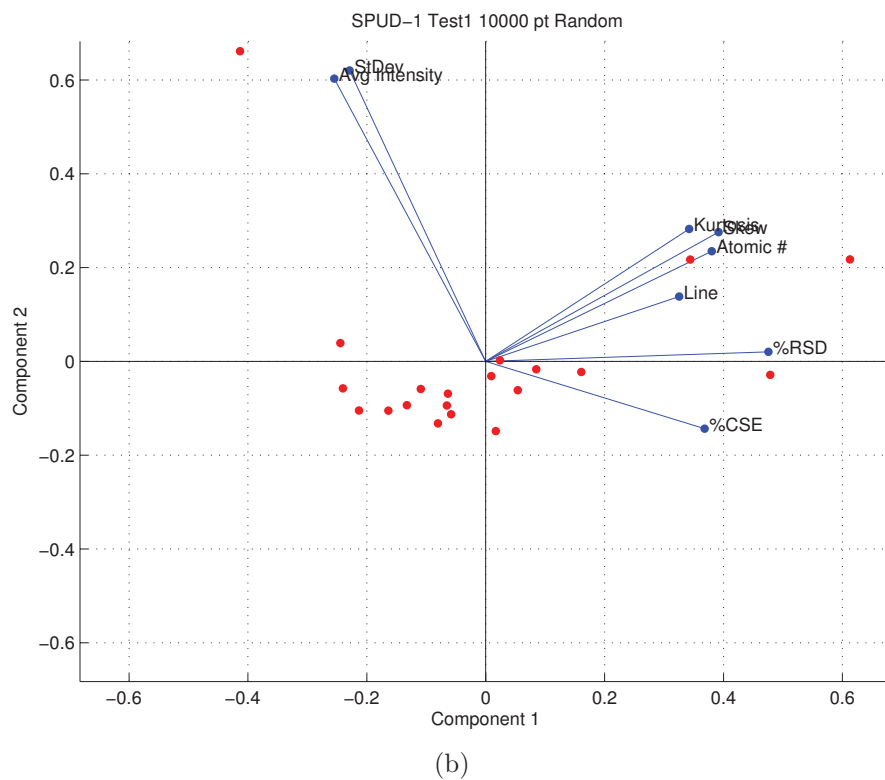
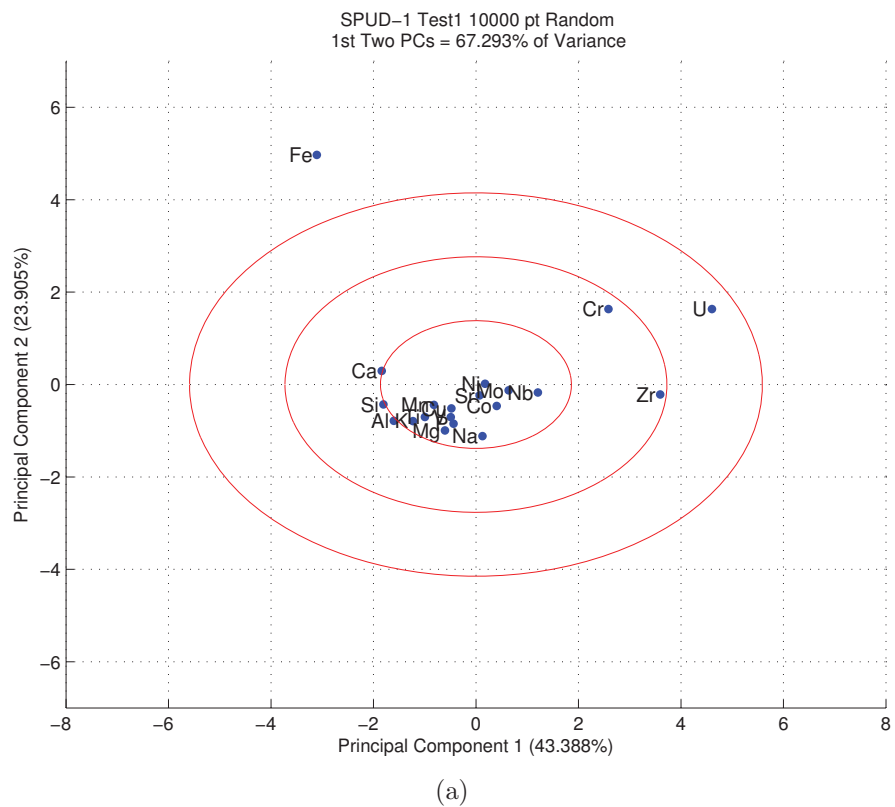


Figure 24. PCA results for random measurements on SPUD-1 Test 1.

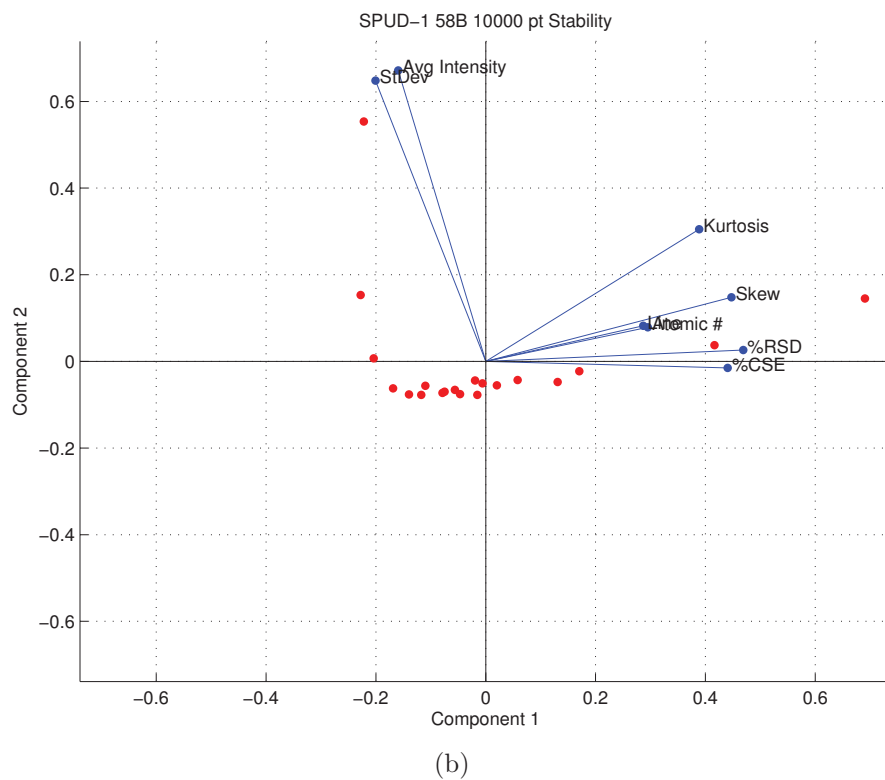
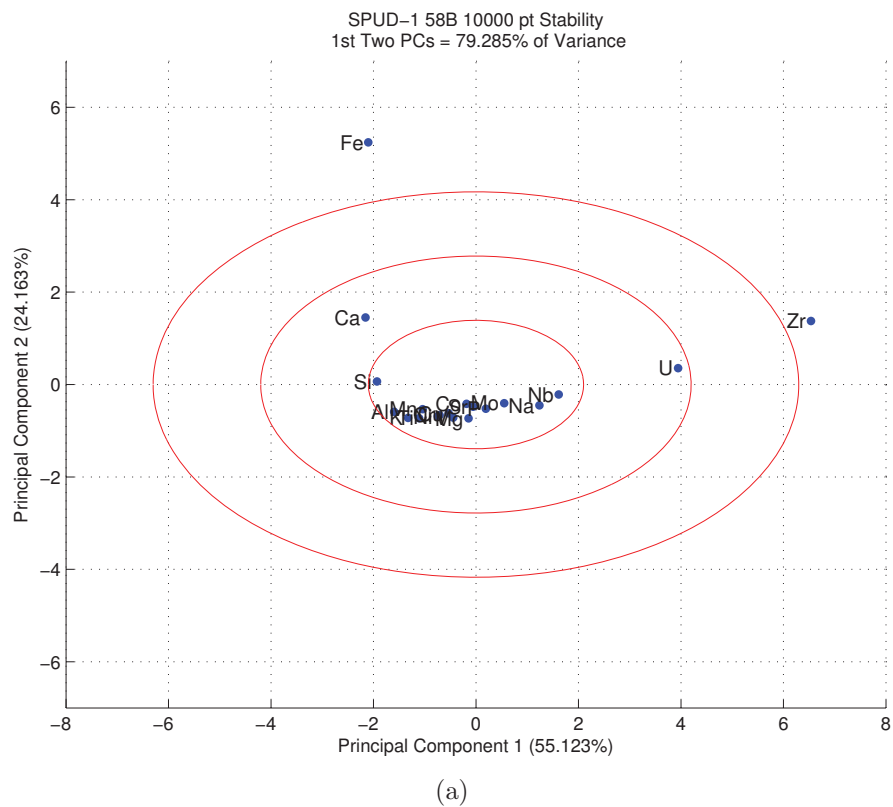


Figure 25. PCA results for stability measurements on SPUD-1 58b.

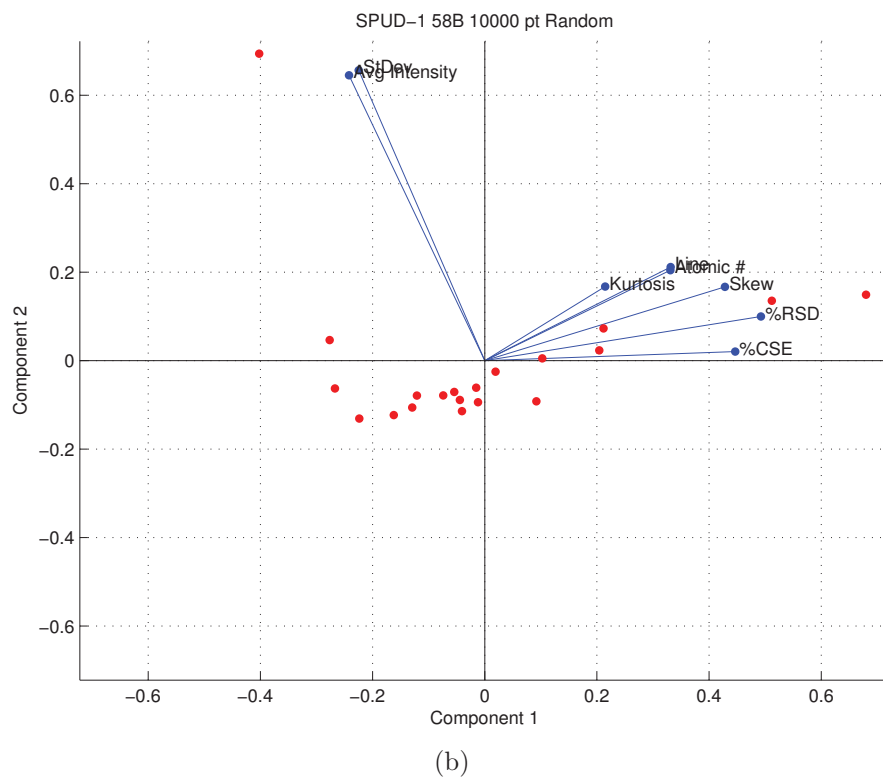
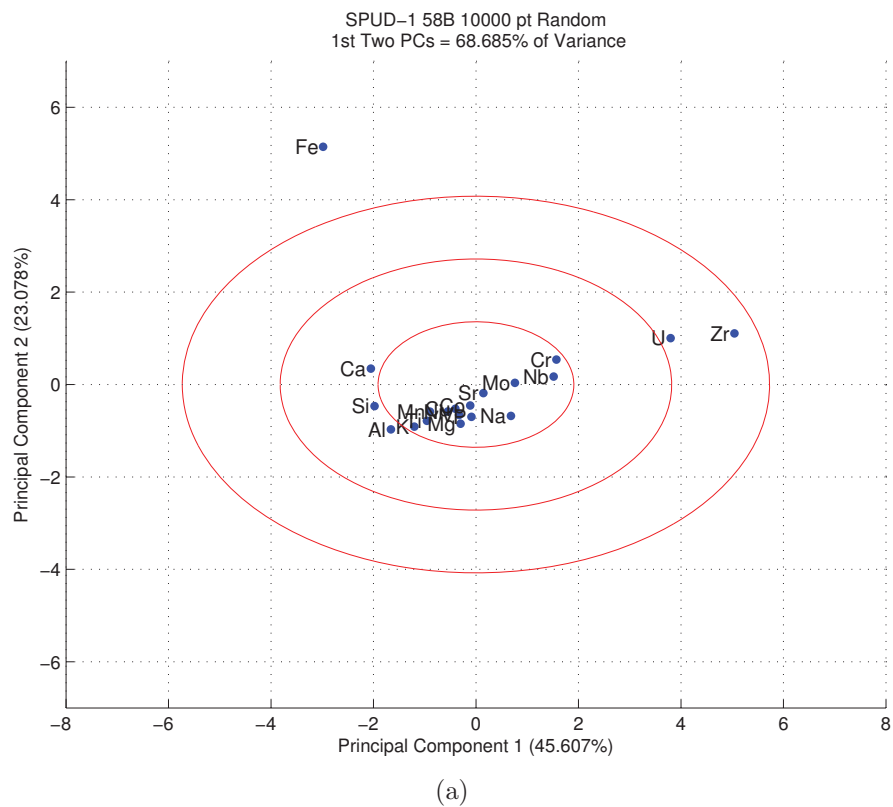


Figure 26. PCA results for random measurements on SPUD-1 58b.

The scatter plots again indicate that 10000 measurements in one location gives a more homogenous result than 10000 measurements in unique, randomly determined locations. For SPUD-1 Test 1, this accounts for approximately a 12% difference in variance accounted for by the first two principal components. For SPUD-1 58B, the difference between the random point collection and the stability analysis accounts for approximately an 11% difference. When calculated to three decimal places, the difference between the variance accounted for by the first two PCs in a random measurement of these two samples is 1.515%. This result aligns with the expectation that each SPUD sample be comparable in composition and relative homogeneity to every other SPUD sample.

The stability measurements for both samples reveal heterogeneities in Fe and Zr. Again, because these measurements are all taken at the same point on the sample, they indicate distribution variance that is not a result of actual sample variation, and instead indicate intensity distribution differences that are caused by other factors, such as machine error. The lack of heterogeneity shown for Zr in the random measurements indicates that some of this variance is controlled by random point sampling, and that Zr may be more homogeneous than it appears. The consistency of the Fe heterogeneities shown between stability and random measurements in both samples mirror the results of PCA on 2702 and 2703. Again, the Fe content in these samples likely does not display the nugget effects shown in this experiment; further interrogation is needed to determine the cause of this behavior.

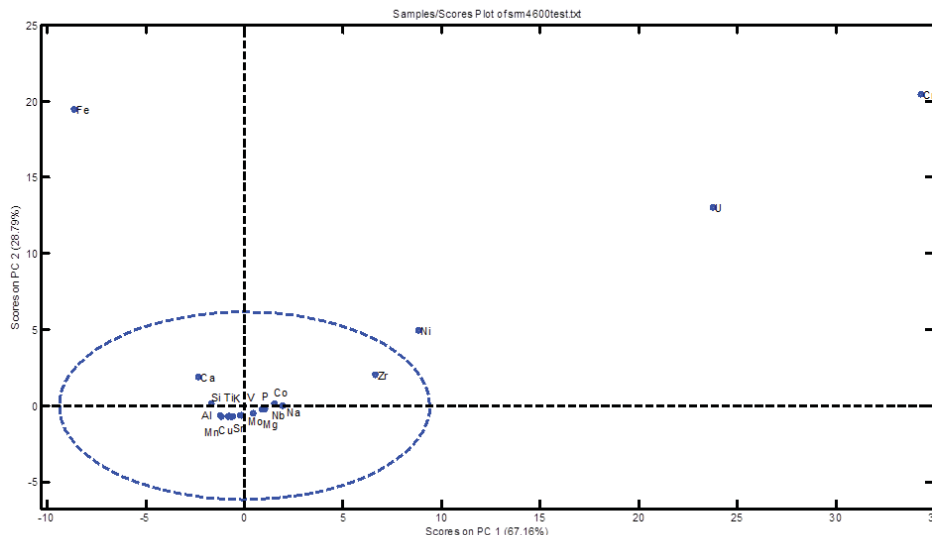


Figure 27. NIST PCA results plot for SPUD-1 Test 1.

For comparison to NIST techniques, the scatter plot shown in Figure 27 was provided. Though there are some algorithmic differences between the two PCA codes, which are difficult to pinpoint due to NIST's use of a third-party software system for PCA analysis, the general trend in data point location is consistent. It should be noted that the PCA descriptors that NIST uses for its plots are: Average Intensity, Standard Deviation, Skew, Kurtosis, %RSD, and %CSE. All preceding analysis in this paper has also used these descriptors for consistency, with the addition of Atomic Number and Line Energy as used by Molloy and Sieber in previous NIST studies [13, 14]. However, analysis of the loading coefficients for these descriptors indicates that not all of these can be categorized as the descriptors that best describe the data set. For the first principal component in the Test 1 random measurement, which accounts for 43% of the variance in the data set, the weights in Equation 6 are assigned to each descriptor. The descriptors with higher-valued loading coefficients have a stronger influence on the spread of data than their lower-valued counterparts. That means that these descriptors are the ones that should be retained if simplification of the

data set is desired.

$$\begin{aligned}
 PC1 = & -0.187AvgInt - 0.225StDev + 0.458RSD + 0.430CSE + 0.439Skew \\
 & + 0.406Kurtosis + 0.287AtomNum + 0.281LineE
 \end{aligned}
 \tag{6}$$

These weights indicate that, if six descriptors are to be chosen from the eight used in the original NIST studies, then more accurate results would be found by eliminating Average Intensity and Standard Deviation and instead using RSD, CSE, Skew, Kurtosis, Atomic Number, and Line Energy. This is acceptable from a statistical standpoint because both Average Intensity and Standard Deviation of the sample are accounted for in the calculation of the RSD. If further simplification were desired, only those weights that are valued above the average of all of the loading coefficients might be used: Skew, Kurtosis, %RSD, and %CSE. When only these four descriptors are used, the results of the SPUD PCA appear as shown in Figures 28 - 31, and the weight of each descriptor is given in Equation 7.

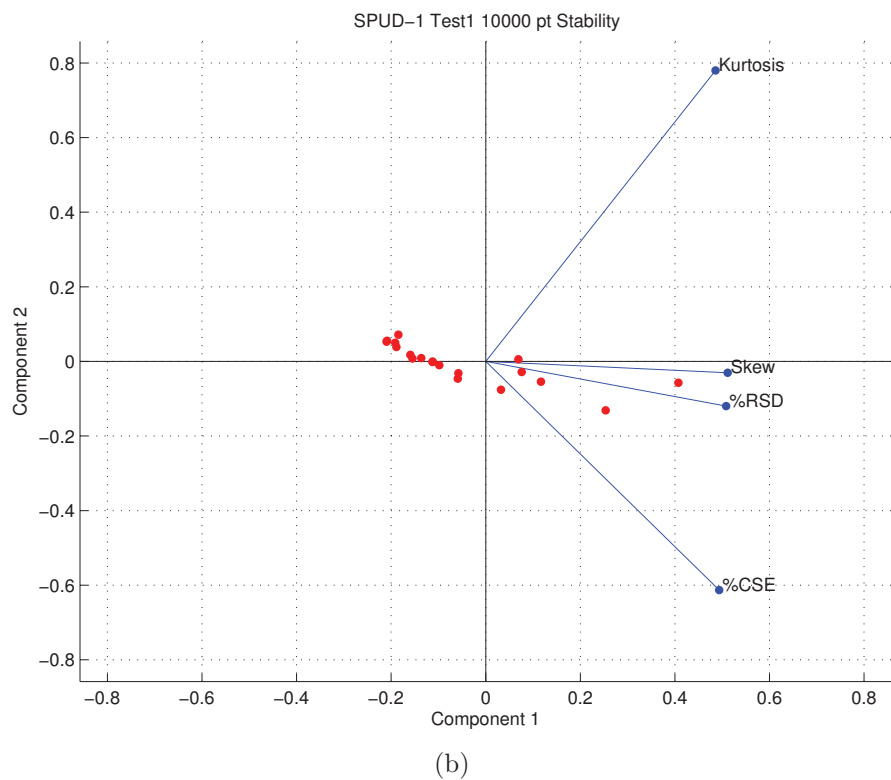
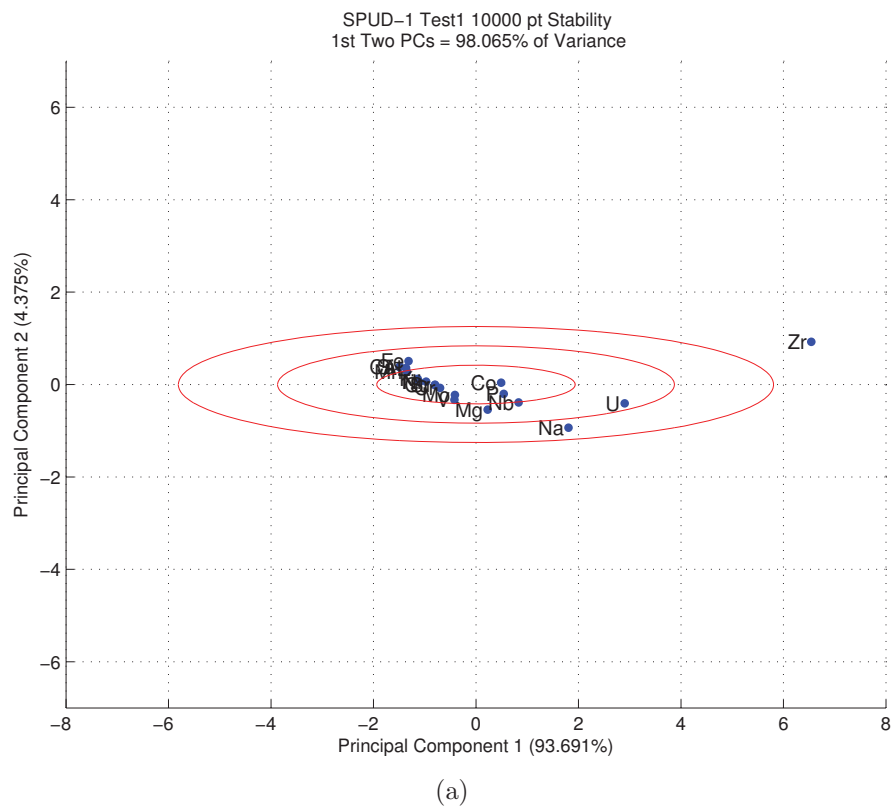


Figure 28. PCA results for stability measurements on SPUD-1 Test 1 using only important descriptors.

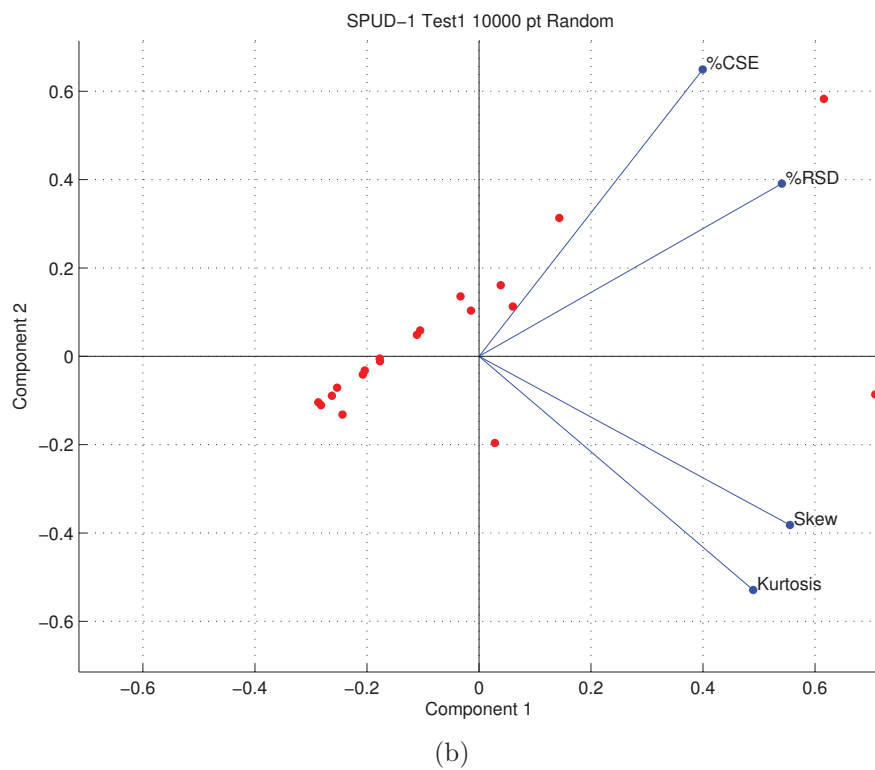
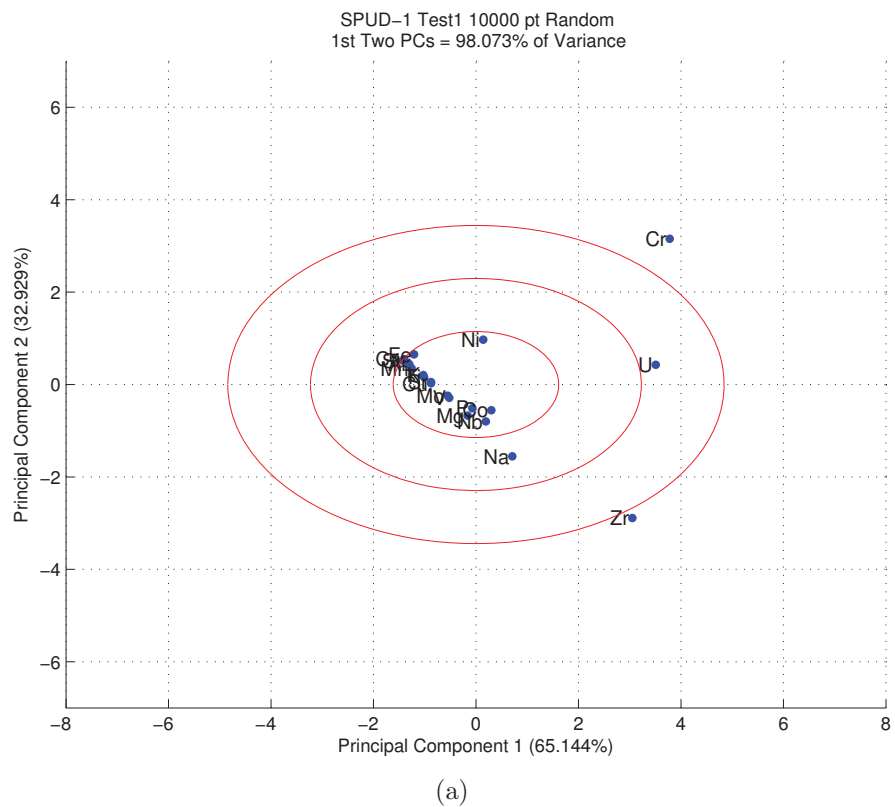


Figure 29. PCA results for random measurements on SPUD-1 Test 1 using only important descriptors.

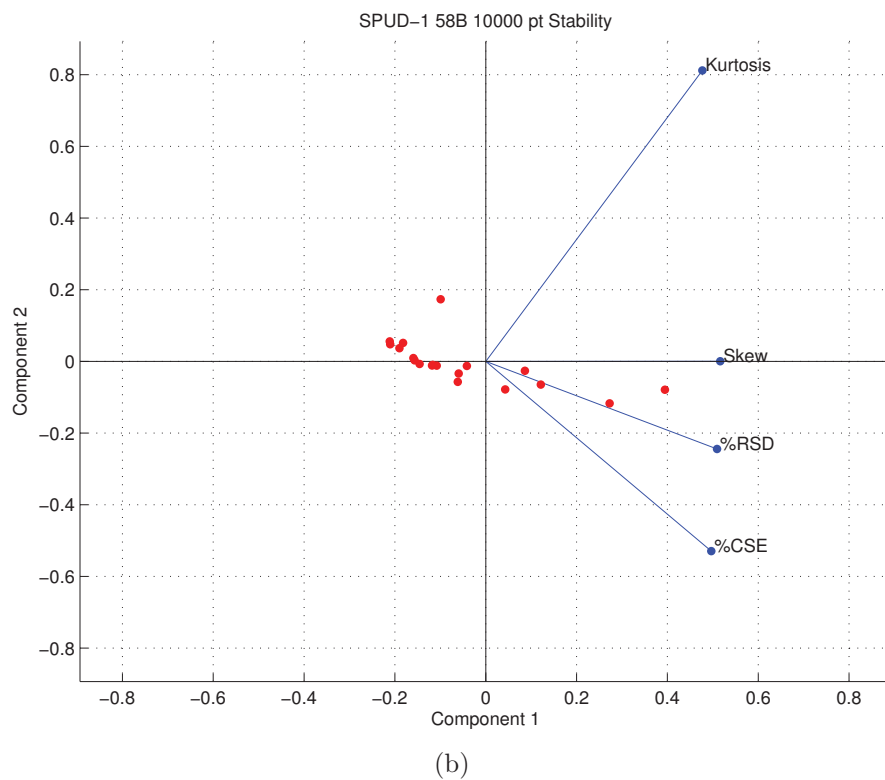
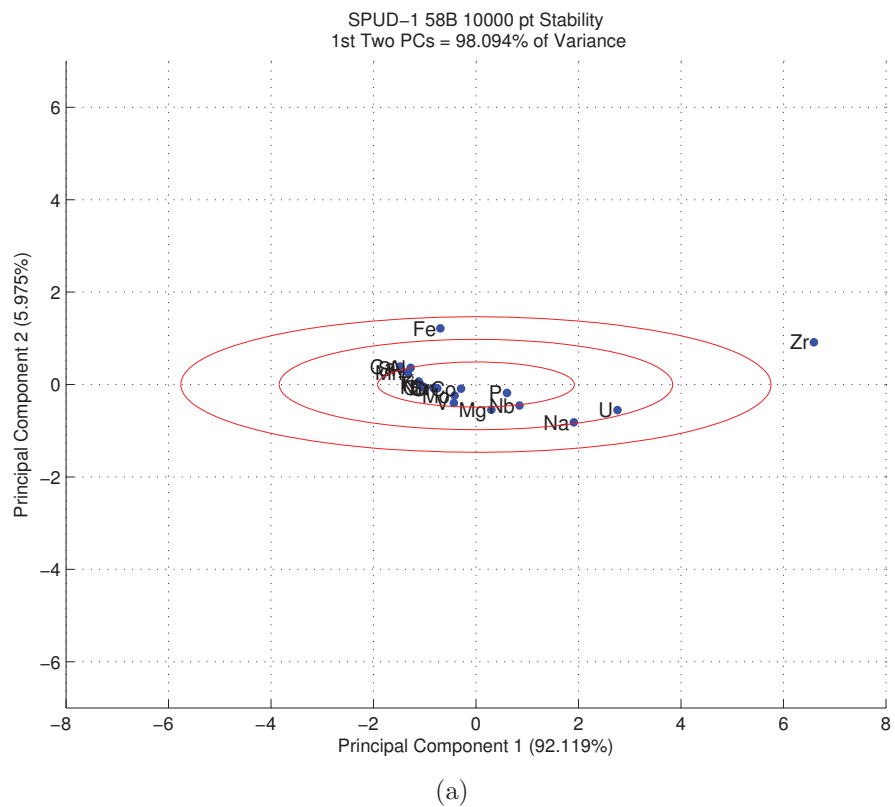
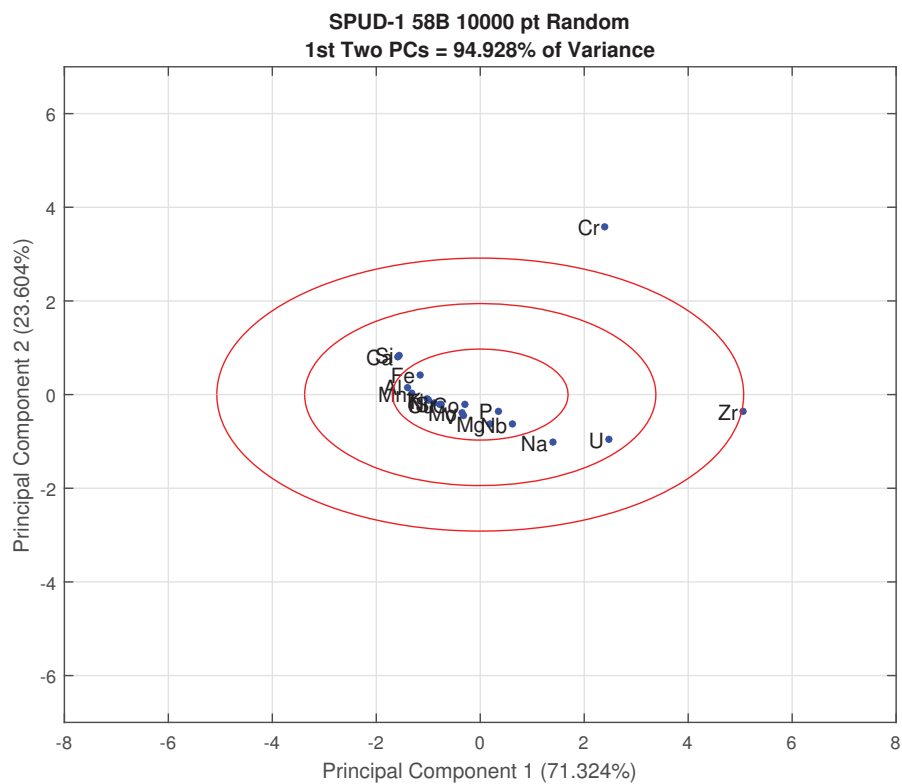
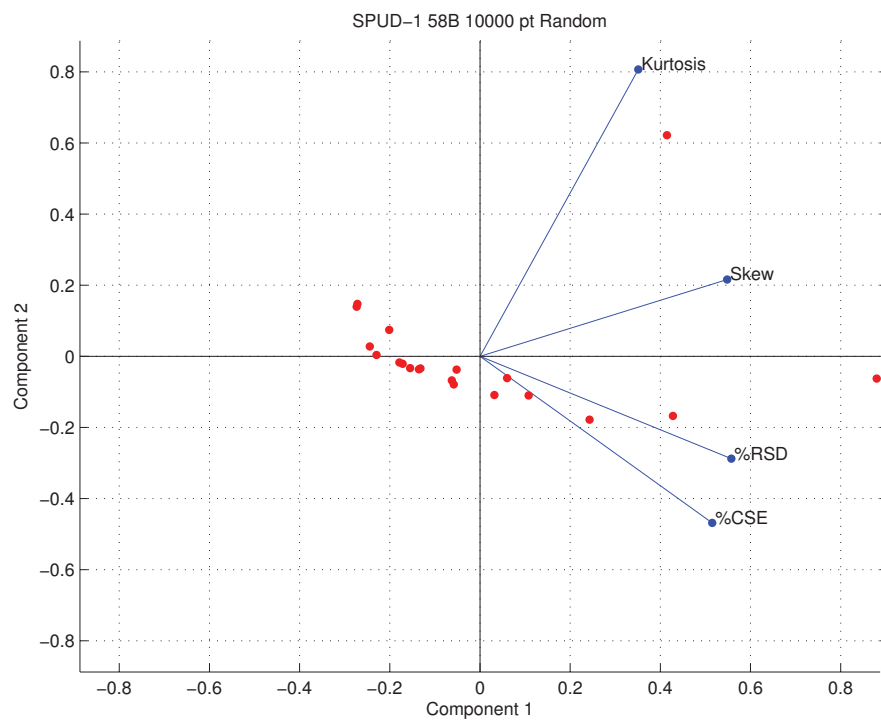


Figure 30. PCA results for stability measurements on SPUD-1 58b using only important descriptors.



(a)



(b)

Figure 31. PCA results for random measurements on SPUD-1 58b using only important descriptors.

$$PC1 = 0.541RSD + 0.399CSE + 0.555Skew + 0.490Kurtosis \quad (7)$$

The removal of Average Intensity and Standard Deviation as descriptors neutralizes the outlying behavior of Fe, confirming that it is likely an artificial behavior, and not representative of the sample's true variance. This method also reveals heterogeneities in Cr in the random measurements that are not found in the stability measurements, indicating the presence of nugget effects for this element, which agrees with the NIST analysis.

Infinite Thickness and Minimum Sample Size.

Preliminary minimum sample size for the SPUD material was computed through a study of infinite thickness, the formula for which is given in the theory section of this paper. This resulted in an infinite thickness depth of 2.242 mm. This thickness was then used as the depth component in the volume of a pressed briquette, with a 10 mm pellet radius corresponding to the 10 mm die used in this study. The resulting minimum sample mass was 0.607 g.

6. Results: Fallout

6.1 Micro-XRF Results

Eleven total LLNL fallout samples from two different sample disks were analyzed in this study. From Disk 1, Row 1, Samples 1-5; Row 3, Sample 1; and Row 4, Sample 2 were analyzed. From Disk 2, Row 2, Samples 1 and 5; Row 3, Sample 1; and Row 4, Sample 1 were analyzed. The first five samples were chosen in order to include a variety of radiation levels, while the latter six were chosen due to relatively well-defined areas of activity. The samples are shown in Figure 32.

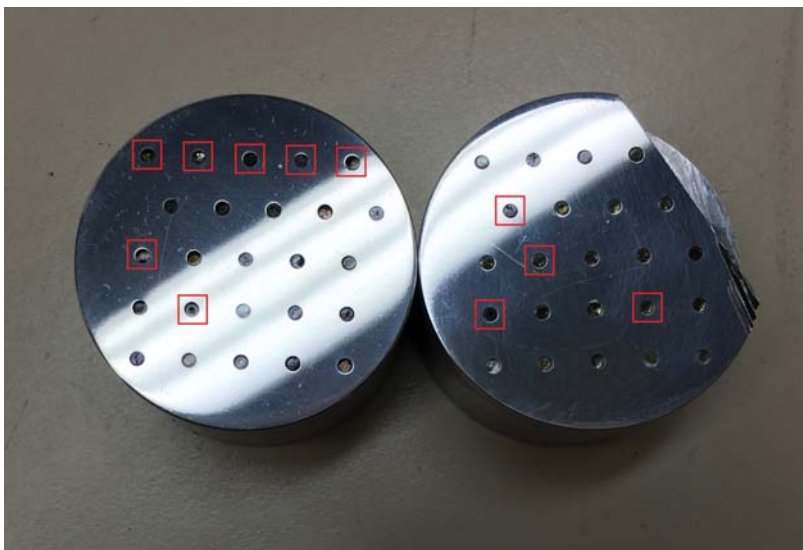


Figure 32. The fallout samples used in this experiment shown mounted in aluminum disks. Disk 1 is on the left and Disk 2 is on the right. Samples that were examined are indicated with red boxes.

As stated in the Experiment section of this paper, five element maps were retained from the raster scan of each sample: Si, Ca, Fe, K, and Ti, which across all samples showed the most significant intensities and levels of variation. These maps are shown in Figure 33. The sum spectrum from these raster scans was then used to identify detectable elements of interest, which were then quantified for the grid of 2500 individual spectra collected for each sample.

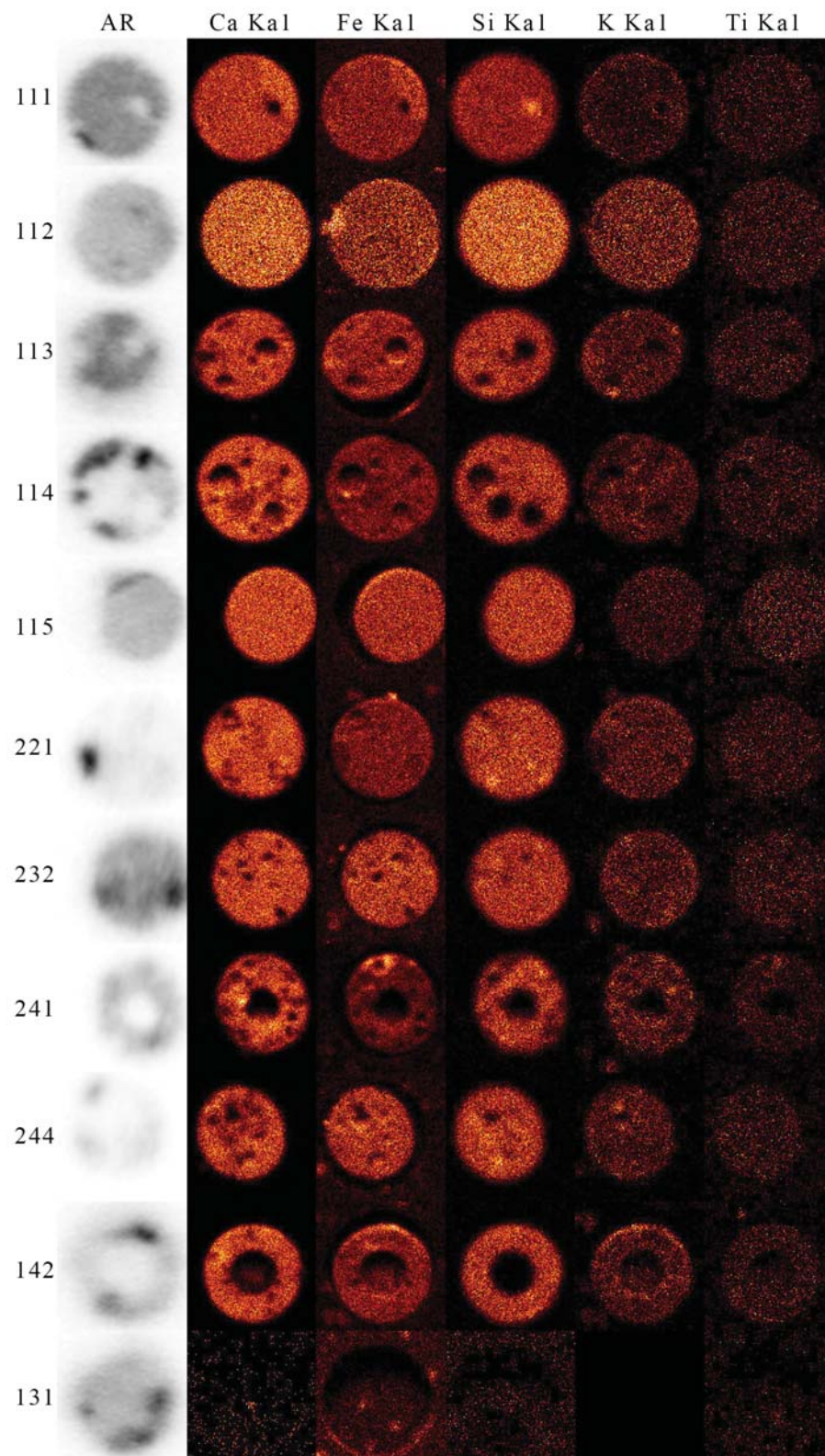


Figure 33. Autoradiography and micro-XRF raster scans for each of the LLNL fallout samples examined in this experiment.

Upon qualitative inspection, it appears that the presence of radiation can be attributed to a high concentration of calcium or iron. This is particularly prominent in samples 111, 221, 244, and 142, as significant inclusions appear to correspond to darker segments of autoradiography. It appears in sample 111 that the presence of silicon may be a contributing factor to the absence of activity. Samples 113, 114, 221, 241, and 142 appear to indicate that the absence of potassium may be a contributing factor to the presence of activity. However, none of these conclusions are consistent or definitive. It was suggested by a previous study [3] that the presence of activity may be correlated not to a particular element, but to a combination of elements —specifically mafic glass, which is a silicate material that is rich in calcium, magnesium, and iron. Therefore, PCA analysis of these fallout samples is performed on a combination of elements at once, in an attempt to find the elemental composition of the materials most closely associated with activity.

6.2 Principal Component Analysis

Sample Separation.

PCA was performed on the micro-XRF results in several different ways in order to examine different influences on the spread of the data.

First, the micro-XRF data for the LLNL samples was combined with the micro-XRF data from 2702, 2703, and the SPUD-1 samples. This was done to determine whether it is possible to separate samples with different compositions, as well as whether it is still possible to identify differences in homogeneity via PCA. Then, the LLNL samples were analyzed only against one another. This was done to examine the possibilities for differentiating between fallout with different compositions. These studies were done in tandem to find a simple model for the separation of samples taken from the environment.

For this method, PCA was performed on element intensity values as quantified by the micro-XRF software. The goal of this study is to progressively eliminate those elements that have a smaller influence on the spread of the data in the most information-rich PCs so that only the elements that are most helpful to fallout sample differentiation remain. Once this is accomplished, the intensity levels for those elements will be examined for patterns that help to identify the presence or absence of activity in a sample. For the initial run, shown in Figures 34 and 35, all of the element intensities that the fourteen samples have in common were used as descriptors for each measured location on each fallout sample. These elements were: Si, Ca, Fe, K, Mg, Al, Ti, Cr, Mn, Ni, Cu, and Sr.

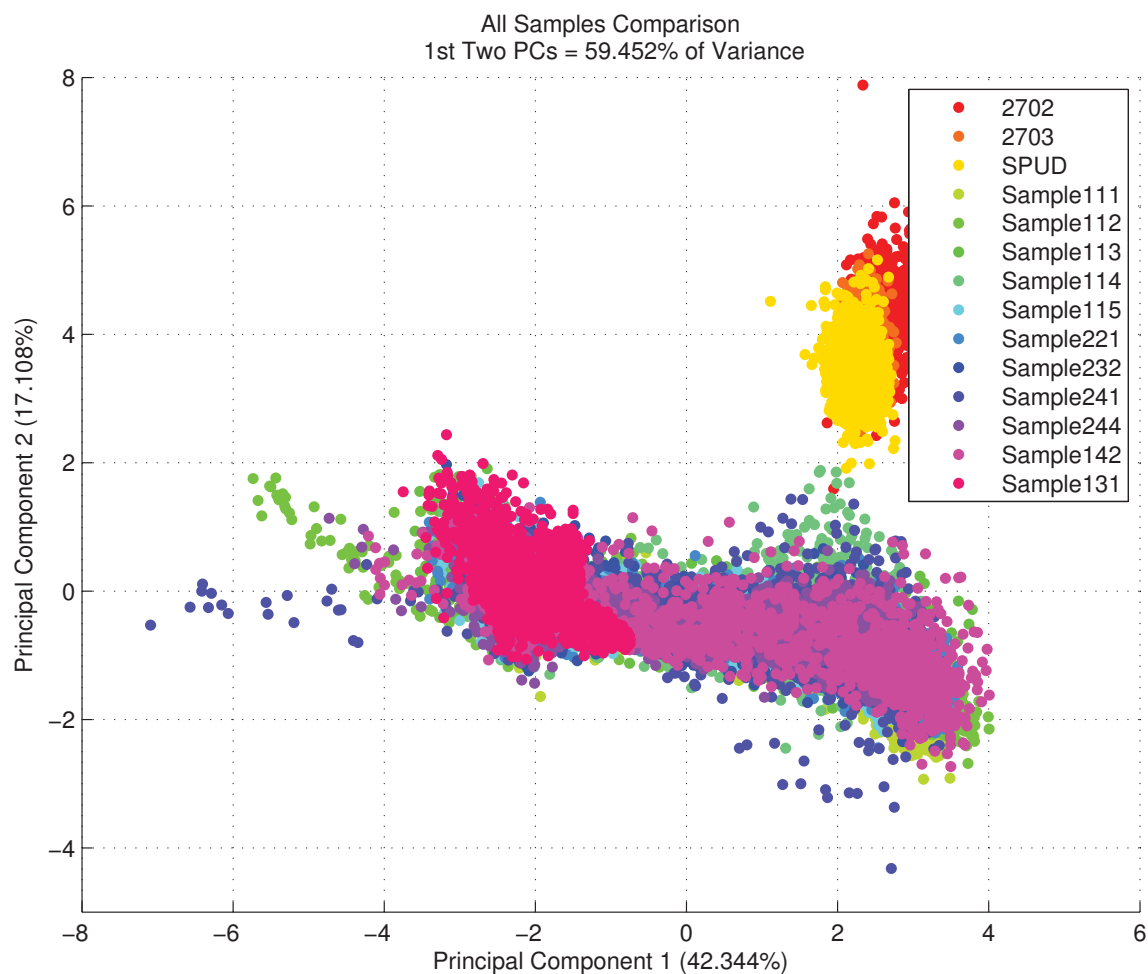


Figure 34. Scatter plot, color-coded by sample, of a comparison of all samples examined in this study. PCA was conducted upon the element intensity values of every element that all fourteen samples had in common.

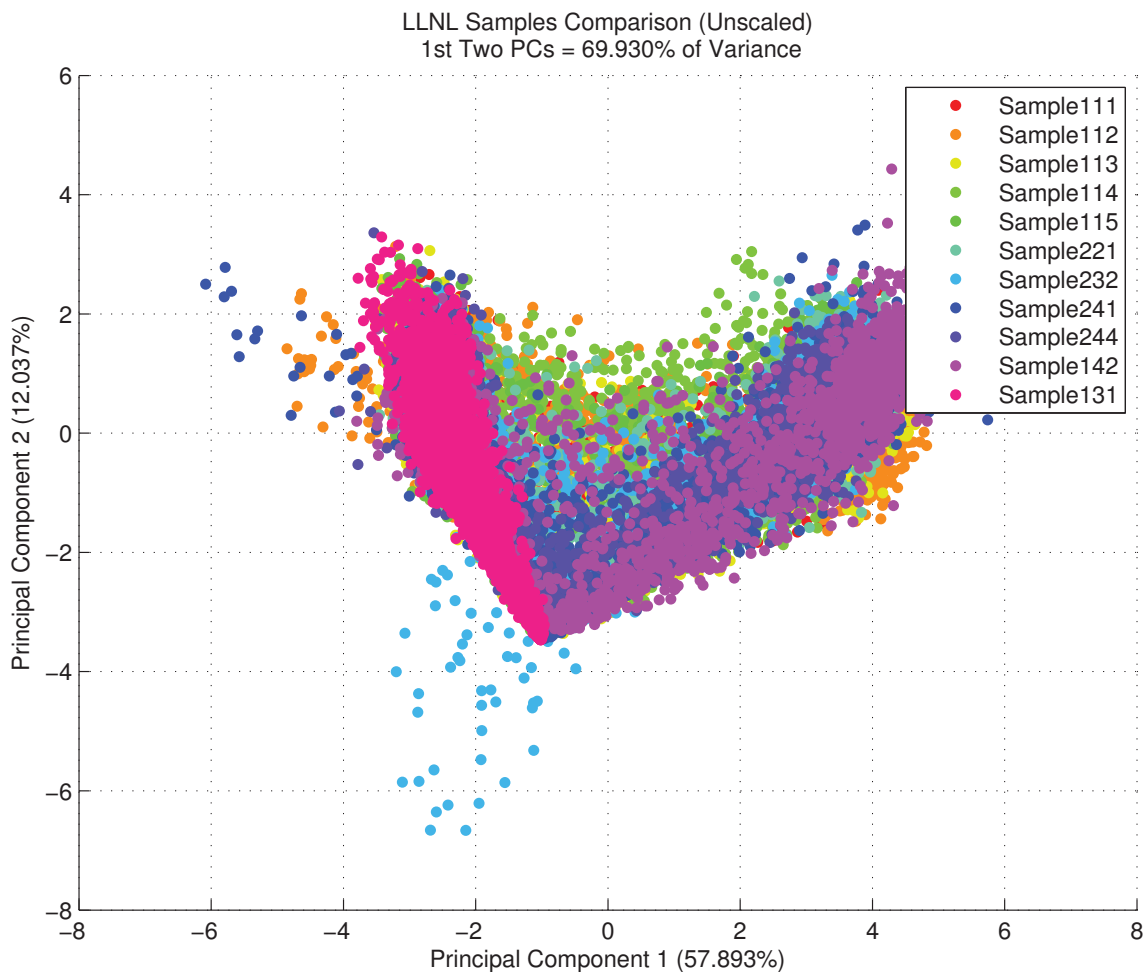


Figure 35. Scatter plot, color-coded by sample, resulting from PCA performed upon all eleven LLNL fallout samples using all element intensities.

When all of the samples are analyzed, the plotted results demonstrate two main clusters of data points: the NIST SRM and the LLNL fallout. The more closely-grouped nature of the data points belonging to the NIST SRM suggests that these samples are more homogeneous than the fallout samples, which is already known to be true. This first PCA iteration does not give much information in terms of differentiating similar samples; were the plots monochromatic, only two groups would be visible. The first two PCs also only account for about 59% of the variance in the data set, indicating that this plot is not necessarily descriptive of all of the factors that influence the data. However, it does effectively separate fallout material from

synthesized, homogenized SRM material.

When only LLNL samples are used, the scatter plot bifurcates into two main “arms” of data with some overlap. This is a much more useful result. It shows that most of the fallout falls into one of two composition categories. However, because there are many factors that influence the spread of this data, as shown in the associated biplot in Figure 36, it is difficult to separate the important influencing factors behind these groupings.

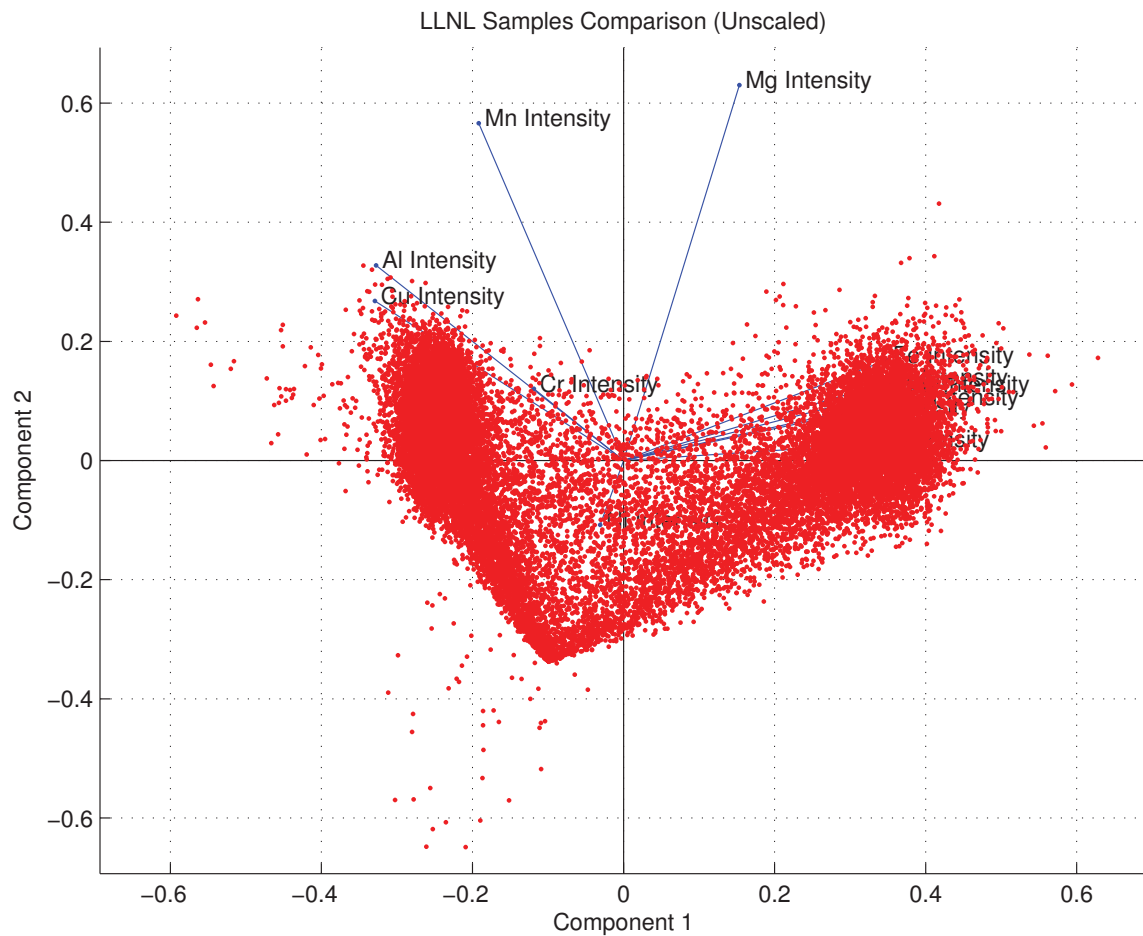


Figure 36. Biplot resulting from PCA performed upon all eleven LLNL fallout samples using all element intensities. Vectors show how each element influences the variance in the samples.

For this reason, the loading coefficient associated with each elemental intensity was evaluated to determine whether or not that element’s intensity values had a

major influence on the spread of the data. Evaluating these loading coefficients and eliminating those that are less influential to the spread of the data is another way to use PCA to simplify the data set. Those elements for which the loading coefficients are eliminated are removed from the PCA analysis in further iterations. Because computation with fewer descriptors is more efficient, this also contributes to the desired rapid execution of this technique. For the clustering shown in Figure 34, the loadings produced by each are described as shown in Equation 8, and for the clustering shown in Figure 35, the loadings produced by each element are described as shown in Equation 9. Both of these equations apply to the first principal component because it accounts for the largest percentage of the overall variance in the data.

$$\begin{aligned}
 PC1 = & 0.422Si + 0.366Ca + 0.218Fe + 0.375K + 0.089Mg \\
 & - 0.395Al + 0.248Ti - 0.139Cr - 0.041Mn - 0.033Ni \\
 & - 0.398Cu + 0.308Sr
 \end{aligned} \tag{8}$$

$$\begin{aligned}
 PC1 = & 0.364Si + 0.366Ca + 0.349Fe + 0.331K + 0.153Mg \\
 & - 0.328Al + 0.351Ti - 0.119Cr - 0.192Mn - 0.031Ni \\
 & - 0.329Cu + 0.297Sr
 \end{aligned} \tag{9}$$

For the data set containing the SRM and the LLNL samples, the average absolute value of the coefficients was 0.253, and for the LLNL samples alone, the average absolute value was 0.267. The absolute value was used because in interpreting the results of PCA, positive and negative numbers serve chiefly to relate data points or descriptors to one another; the important factor in determining whether a descriptor should be kept is the numerical value of the loading coefficient. The further the number is from zero, the more influential the descriptor is. For this study, any coefficients that were below the average absolute value computed for both sets of samples were re-

moved from the equation. For this iteration, Mg, Cr, Mn, and Ni were eliminated. Al was also eliminated from the equation at this time, as the large amount of aluminum in the sample housing disks would overwhelmingly (and, perhaps, inaccurately) associate Al with areas of no activity. Again, it should be noted that data reduction was performed only on the first principal component. Including coefficient values for the second principal component would have produced different key values, and presents another avenue for further investigation.

The process was iterated with the remaining elements (Si, Ca, Fe, K, Ti, Cu, and Sr), resulting in the scatter plots shown in Figures 37 and 38, and the loading coefficients given in Equations 10 and 11.

$$\begin{aligned}
 PC1 = & 0.470Si + 0.394Ca + 0.265Fe + 0.415K + 0.295Ti \\
 & - 0.426Cu + 0.336Sr
 \end{aligned}
 \tag{10}$$

$$\begin{aligned}
 PC1 = & 0.403Si + 0.405Ca + 0.391Fe + 0.368K + 0.392Ti \\
 & - 0.349Cu + 0.333Sr
 \end{aligned}
 \tag{11}$$

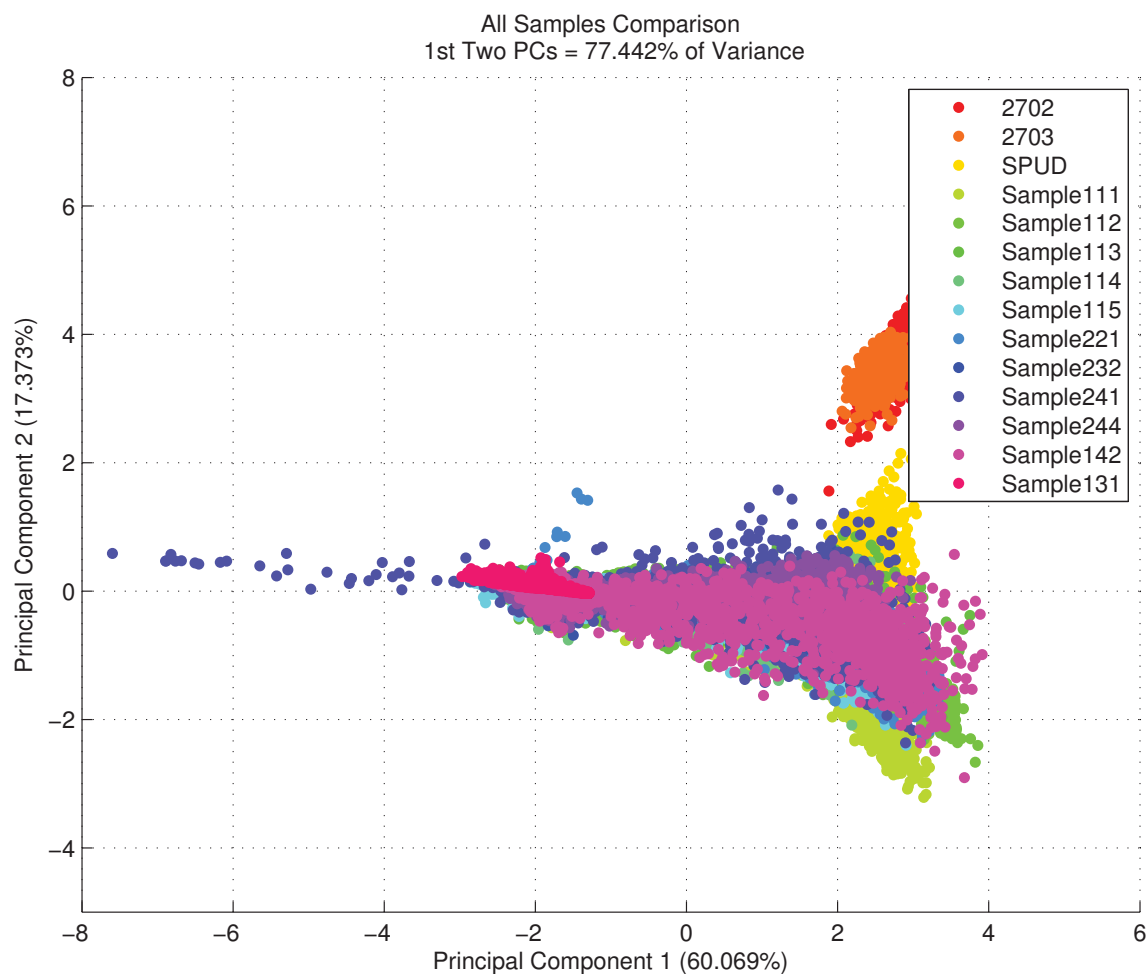


Figure 37. Scatter plot, color-coded by sample, of a comparison of all samples examined in this study. PCA was conducted upon the element intensity values of every element shown to have an above-average influence on the results shown in Figure 34.

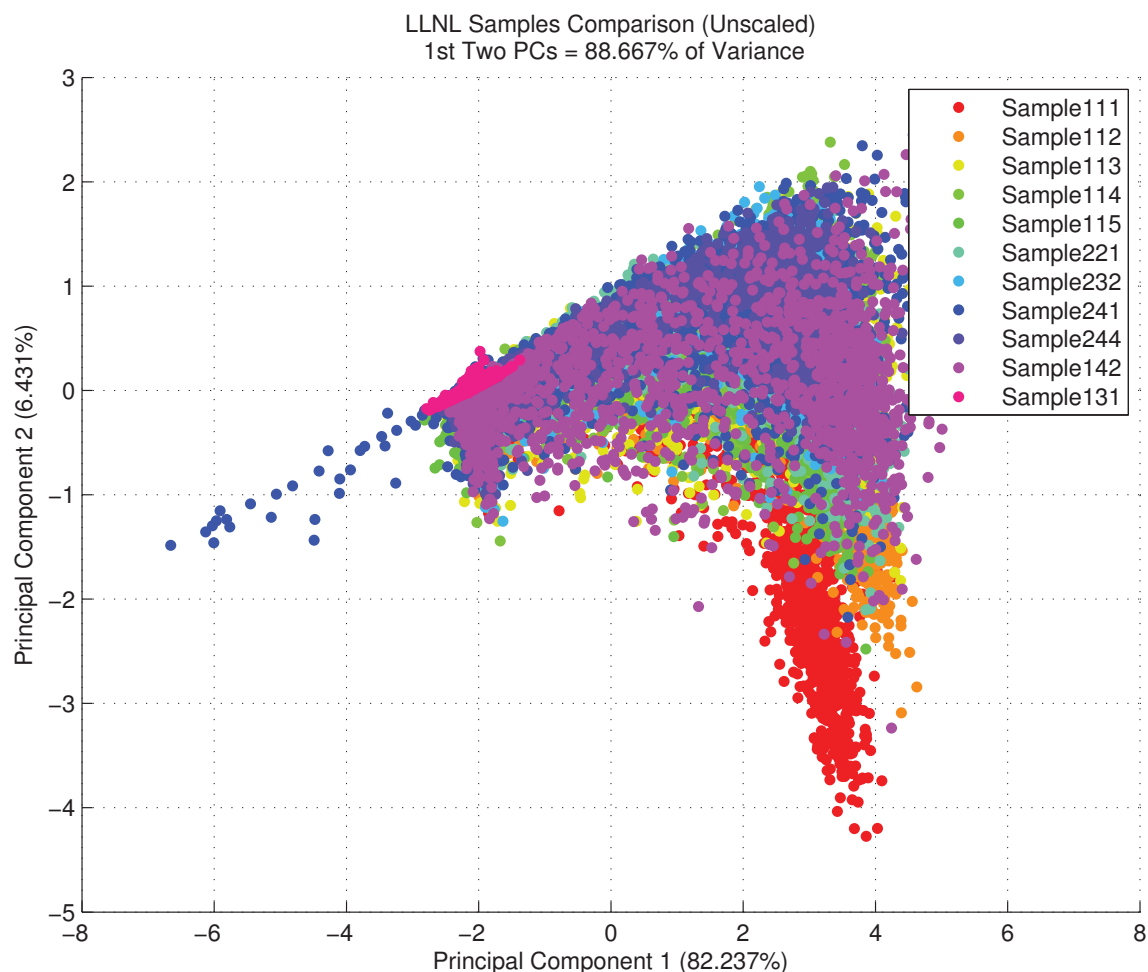


Figure 38. Scatter plot, color-coded by sample, resulting from PCA performed upon all eleven LLNL fallout samples using every element shown to have an above-average influence on the results shown in Figure 35.

In the case of Figure 37, the SPUD data points have shifted noticeably toward the fallout, though it is still identifiable as a material with a different composition. This is not an unexpected result; the SPUD material was synthesized to mimic fallout, and it can be shown with this method that when an adequately simplified model is used, the SPUD performs as intended. The LLNL samples are further defined on this plot, appearing to separate into colored bands that show small differences in fallout composition. Finally, SRM 2702 and 2703 remain separate from the fallout and grouped closely together, which is expected, as they are created from the same

homogenized material.

There is no remarkable change from Figure 35 to Figure 38. Data points from Sample 111 separate clearly from the rest of the data points, but the two general categories of fallout composition remain. For this iteration, the data set containing the SRM and the LLNL samples has an average coefficient absolute value of 0.372, and the data set containing the LLNL samples alone has an average coefficient absolute value was 0.377. This time, the Sr coefficient was removed from both equations, because it is the only element with two below-average coefficients. PCA is then performed on the remaining elements (Si, Ca, Fe, K, Ti, and Cu), yielding Figures 39 and 40 and Equations 12 and 13.

$$PC1 = -0.491Si - 0.389Ca - 0.303Fe - 0.443K - 0.345Ti + 0.448Cu \quad (12)$$

$$PC1 = -0.422Si - 0.428Ca - 0.416Fe - 0.395K - 0.416Ti + 0.370Cu \quad (13)$$

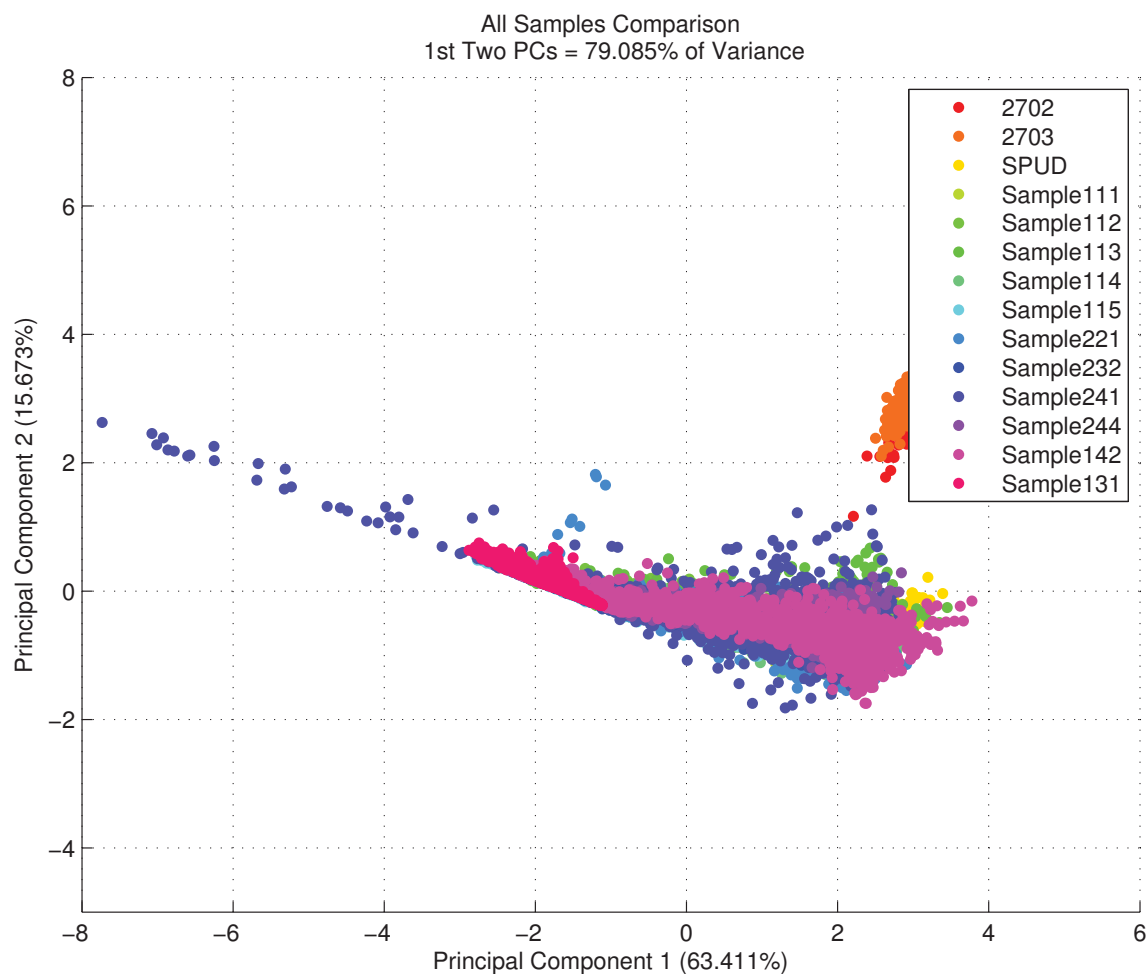


Figure 39. Scatter plot, color-coded by sample, of a comparison of all samples examined in this study. PCA was conducted upon the element intensity values of every element shown to have an above-average influence on the results shown in Figure 37.

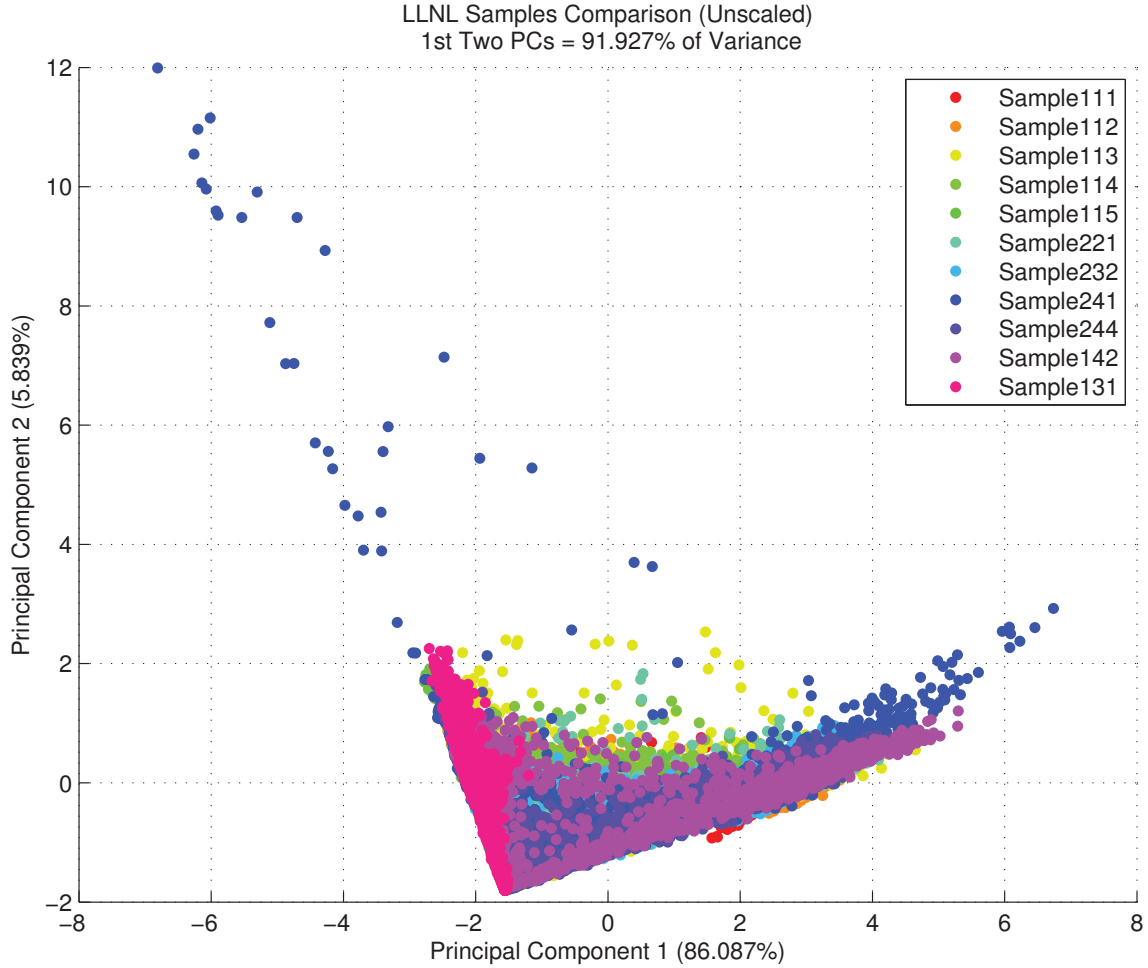


Figure 40. Scatter plot, color-coded by sample, resulting from PCA performed upon all eleven LLNL fallout samples using every element shown to have an above-average influence on the results shown in Figure 38.

When compared to Figure 37, Figure 39 shows that, with a further simplified model, SPUD becomes indistinguishable from real fallout. Figure 40 continues to show two main categories of fallout composition, but the first two principal components now account for 91.9% of the variance in the data set, indicating that the plot is now describing the data set more accurately than it was before. The average coefficient absolute value for the data set including SRM and LLNL samples is now 0.403, while the average absolute coefficient for the data set containing only LLNL samples is now 0.408. None of the elements currently used in the model have two

coefficients that are both below the average, so all six are retained. Furthermore, it is clear from the sign conventions in the coefficient equations that the two main categories of fallout are those that are rich in Si, Ca, Fe, K, and Ti, and those that are rich in Cu. This can also be shown visually with the biplot in Figure 41.

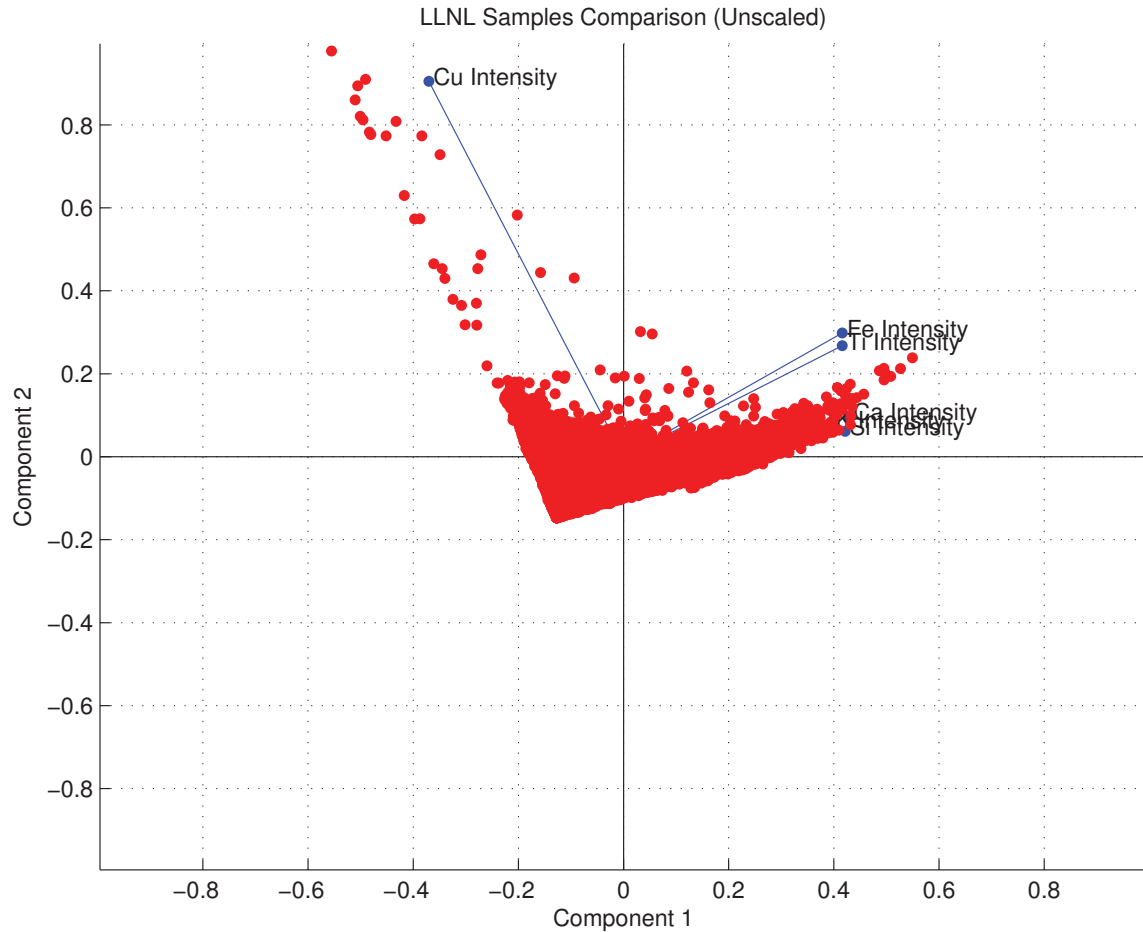


Figure 41. Biplot resulting from PCA performed upon all eleven LLNL fallout samples using every element shown to have an above-average influence on the results shown in Figure 38.

Actinide Correlation.

While it is helpful to know that fallout can be separated from other materials based on composition alone, the true interest of this study is whether PCA can be used to separate out areas that contain radioactivity, and therefore actinides from nuclear fuel.

The next step in analyzing the fallout samples was to locate the most intense radiation and attempt to find a link between activity and composition via PCA analysis. To accomplish this, the normalized autoradiography values from all samples were grouped and tagged according to their value. Those with a value between 0 and 0.7 were tagged “minor activity,” those between 0.7 and 0.8 were tagged “some activity,” those between 0.8 and 0.9 were tagged “more activity,” and those between 0.9 and 1 were tagged “most activity.” When PCA was performed on the data this time, the points tagged “minor activity” were assigned a light background color so that points with more significant activity would stand out. Because the SPUD material was included in this analysis, data points in this category were separated into those with uranium content and those without. Results for the PC iteration described by Equation 8 are shown in Figure 42, while results for the PC iteration described by Equation 12 are shown in Figure 43.

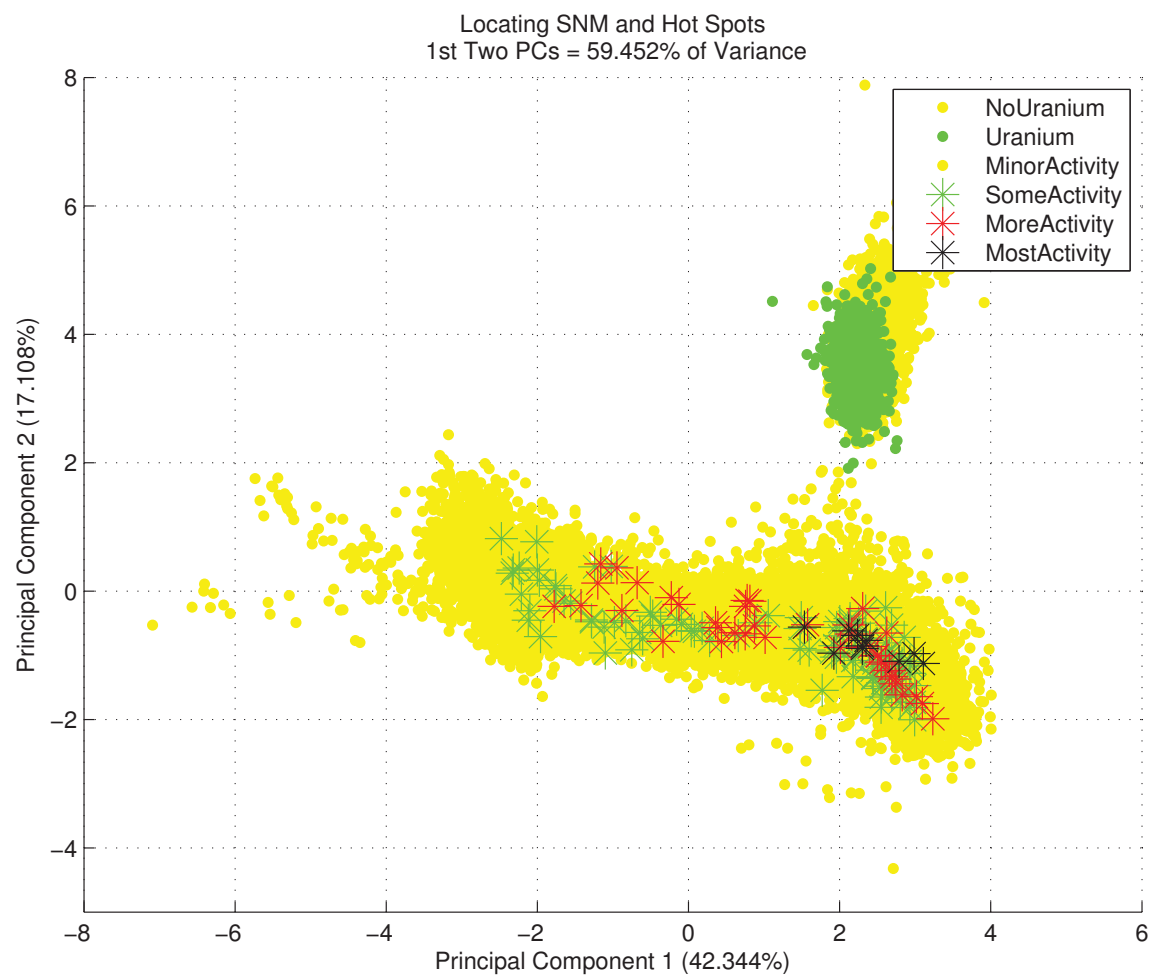


Figure 42. Scatter plot, color-coded by activity and uranium content, resulting from PCA performed upon all samples examined in this study using all element intensities.

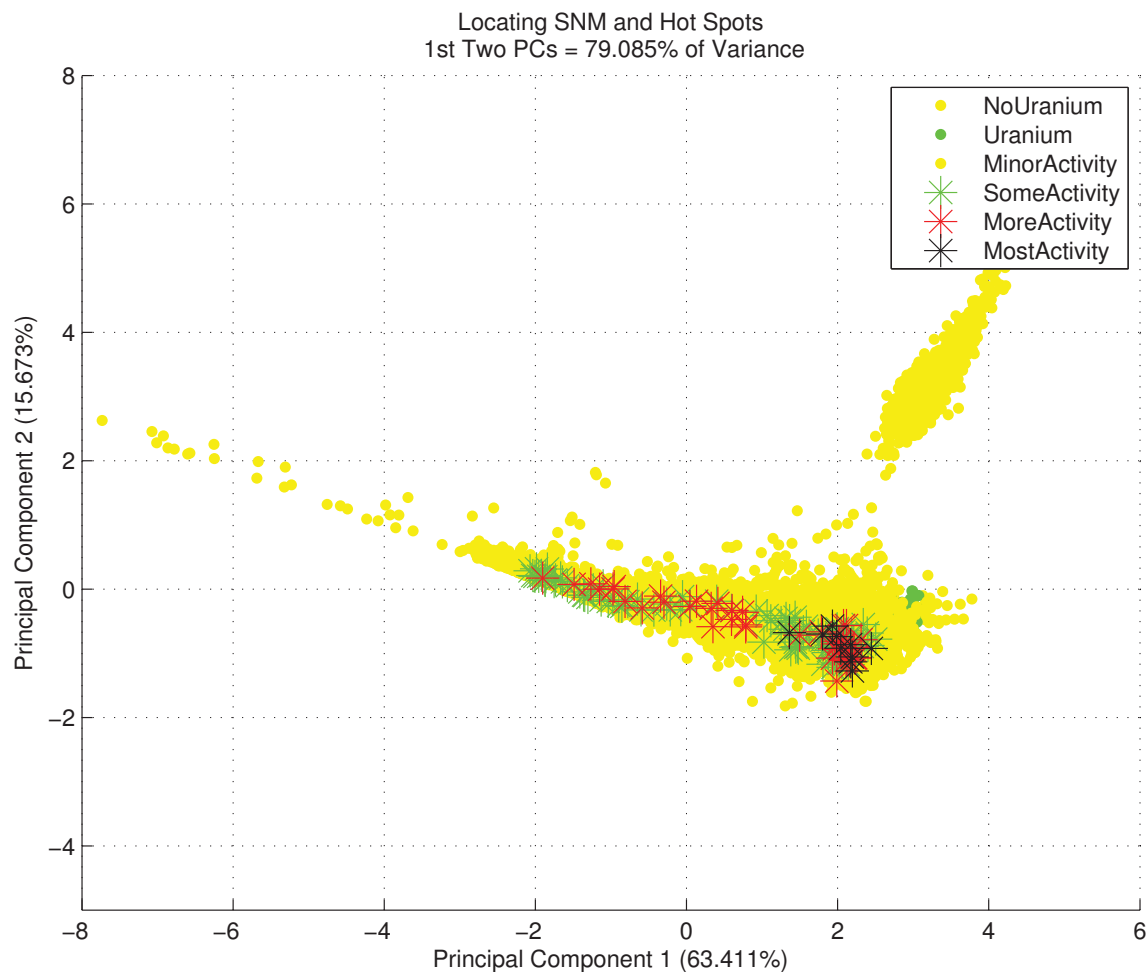


Figure 43. Scatter plot, color-coded by activity and uranium content, of a comparison of all samples examined in this study. PCA was conducted upon six element intensity values: Ca, Si, Fe, K, Ti, and Cu.

While points with “some activity” are scattered throughout the plot, points with “more activity” and “most activity” are confined to increasingly smaller areas within the same region. While not tightly packed, the points with the most activity exhibit notable clustering. It is possible that areas of other samples that have similar characteristics to those found in this region of the data may be more likely to contain nuclear materials of forensic interest. Furthermore, Figure 42 shows that the data points that contain some uranium tend to cluster in one region of the SPUD data, indicating that there are compositional markers for actinides in the SPUD material

as well. This result is more difficult to see in Figure 43, as by this point in the transformation, the SPUD data is no longer visually separated from the fallout data.

An examination of the LLNL samples alone, with no SPUD or SRM material, was also conducted to determine whether the clustering of high-activity regions produced by PCA analysis holds true. The results of the first iteration of this study are shown in Figure 44, and the results of the final iteration are shown in Figure 45.

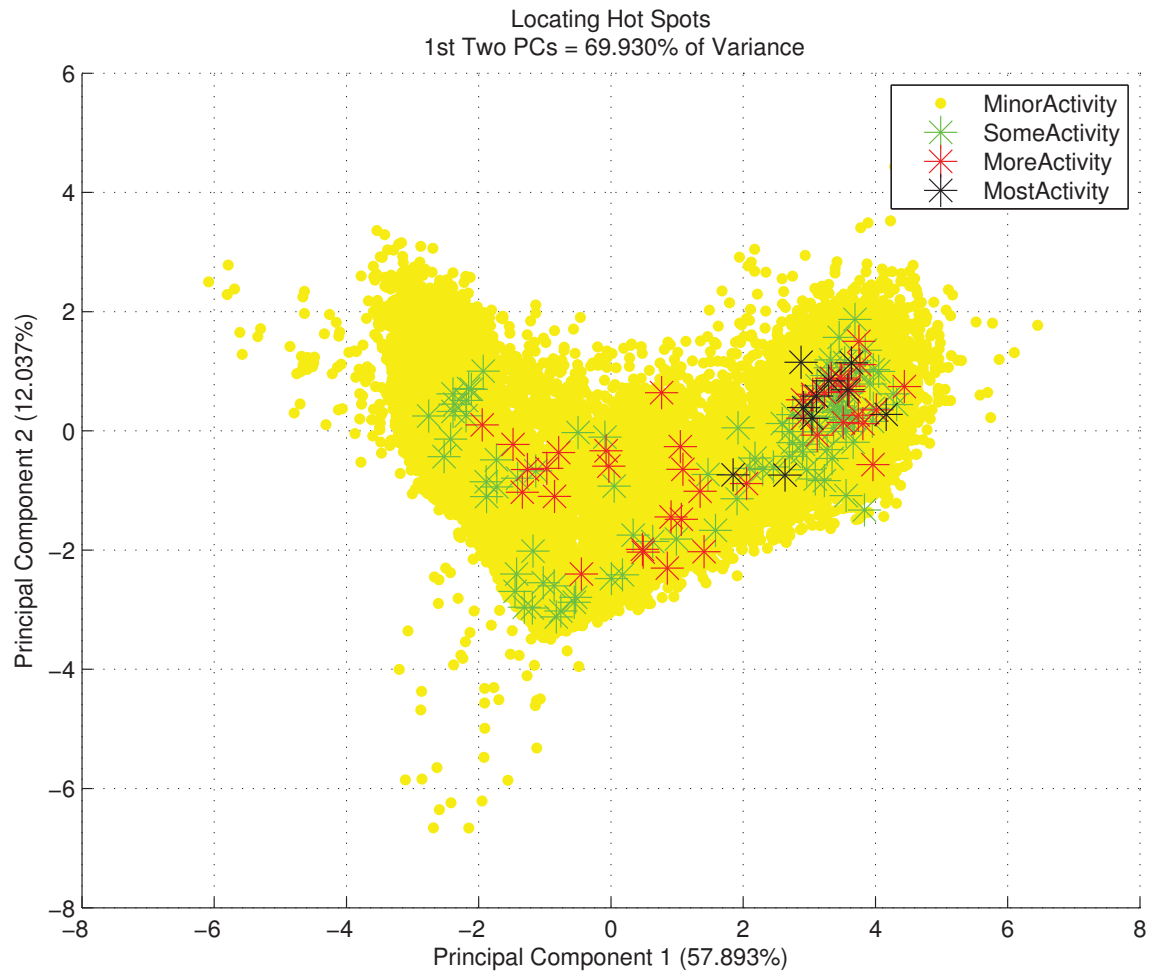


Figure 44. Scatter plot, color-coded by activity, resulting from PCA performed upon all eleven LLNL fallout samples using all element intensities. Notable clustering is seen for the ninetieth percentile, represented by black stars.

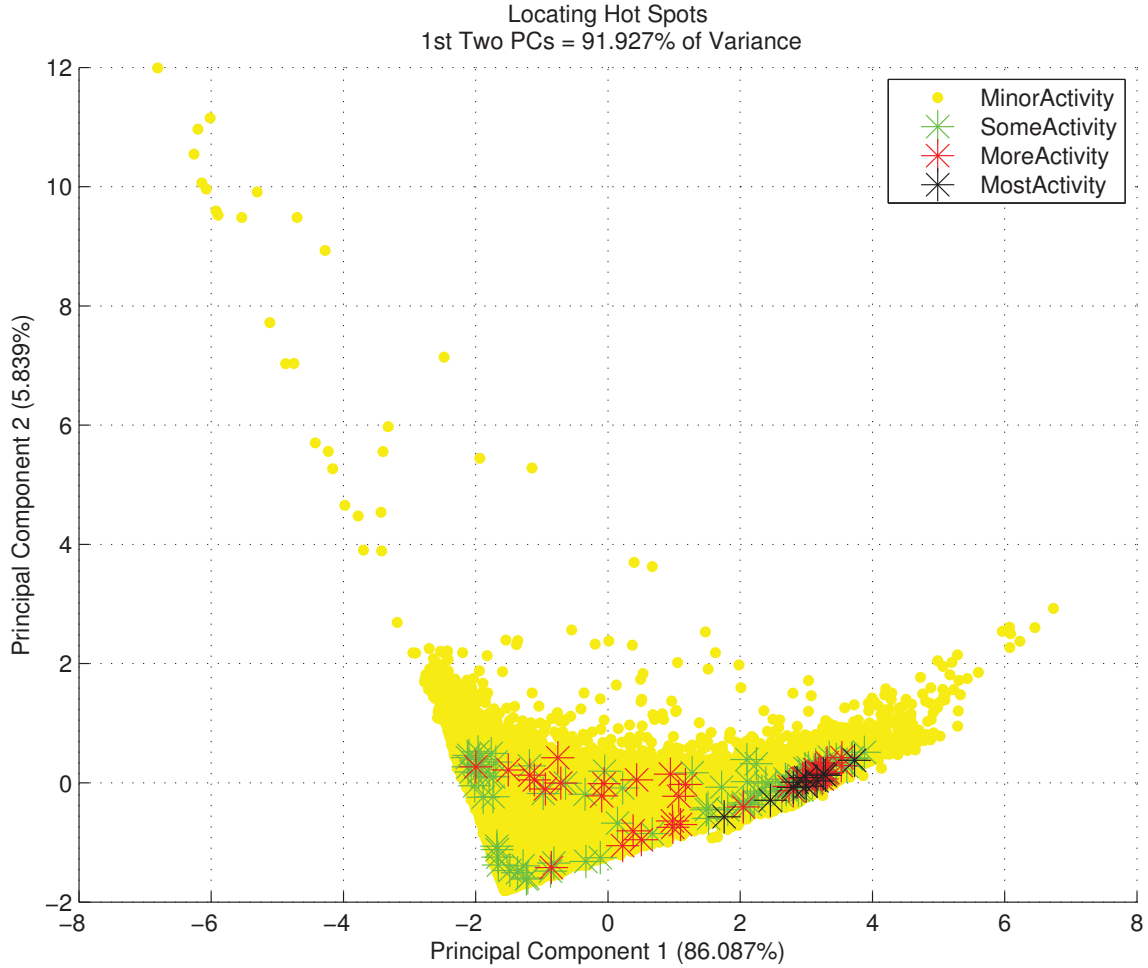


Figure 45. Scatter plot, color-coded by activity, resulting from PCA performed upon all eleven LLNL fallout samples using six element intensity values: Ca, Si, Fe, K, Ti, and Cu. The notable clustering is seen for the ninetieth percentile is maintained even when the model is simplified.

Again, the points with some activity are spread throughout the data set, while those with more activity and most activity are increasingly clustered. Of interest is the demonstrated clustering in Figure 44 of all of the highest-activity data points in the right “arm” of the scatter plot. This means that there is a major compositional category that does not contain any of the highest-activity locations, and also contains fewer of the locations with the next-highest activity. Figure 45 shows that even with a significantly simplified model, the locations with the highest activity still form a cluster. Comparison to Figure 41 visually indicates that these high-activity locations

are likely rich in Si, Ca, Fe, K, and Ti, but are depleted in Cu.

Another area of interest in this study involves determining which particular pieces of fallout contain the most radioactive regions, as this is not immediately visually apparent from the autoradiography maps. This can be accomplished in one of two ways: by categorizing the scaled autoradiography pixel values and referencing the pieces of fallout that correspond to them, or by scaling the LLNL fallout data with the autoradiography pixel values, performing PCA, and plotting the data. Both methods were used in this study and compared to ensure accuracy. The plot of the last PCA iteration of the scaled data is shown in Figure 46.

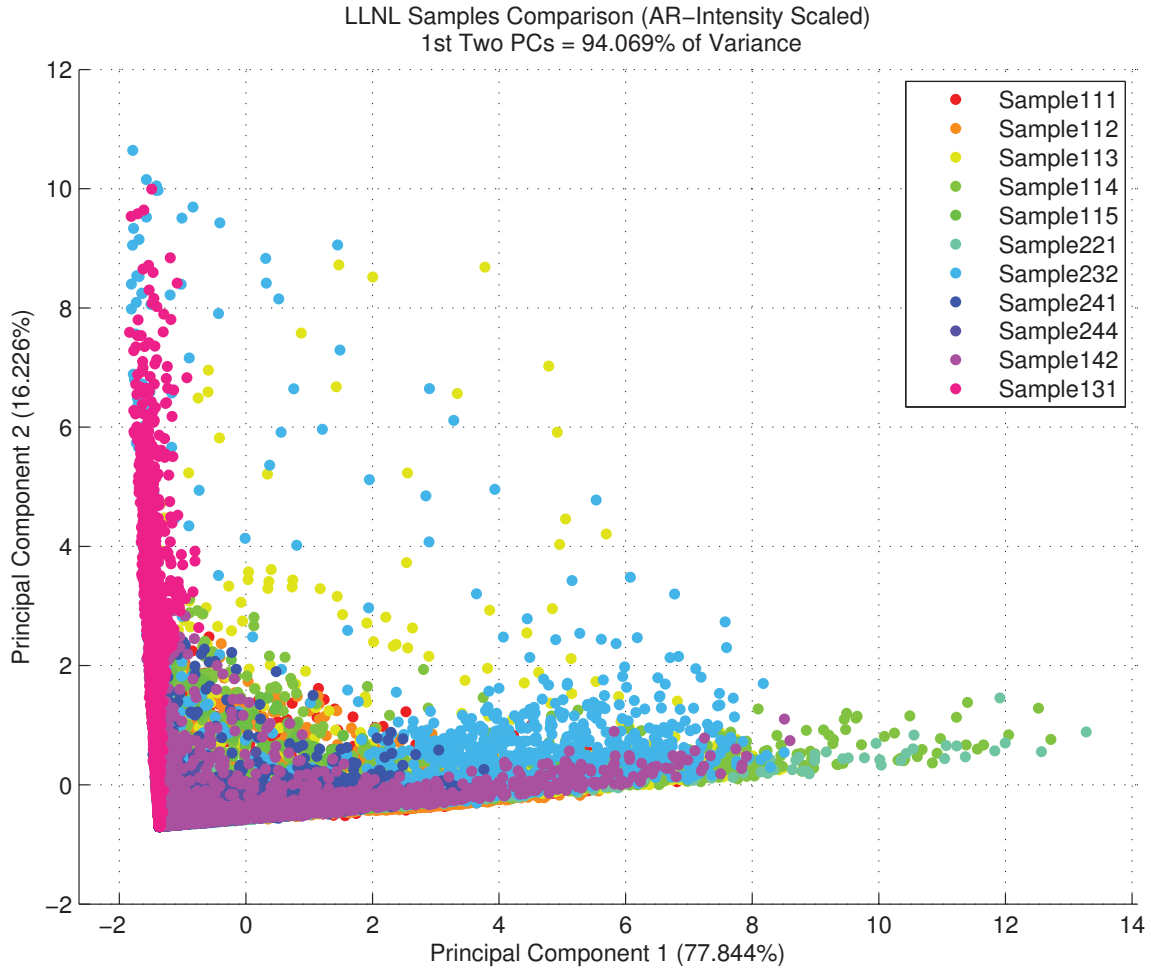


Figure 46. Scatter plot, color-coded by species, of results of PCA performed on fallout element intensity data for five elements (Ca, Si, Fe, K, and Ti) that was first scaled based on the autoradiography pixel value associated with each spectrum. Regions with more radioactivity trend toward the right-hand side of the plot.

In this plot, the data points with the highest activity, scaled with a value closer to one, appear at the far right of the scatter plot, while the data points with the lowest activity, scaled with a value closer to zero, appear at the far left. This plot indicates that samples 114 and 221 demonstrate the locations with the most intense radiation. This is verified by using a series of conditional statements to sort the scaled autoradiography values into categories; again, samples 114 and 221 show the most intense radiation. The least radioactive sample is 131, which has the highest Cu content of the fallout samples.

As a final step, average intensity and mass percentage values for each of the five elements used in the model were collected for locations with top-10% radiation values. The results of this data collection are shown in Tables 11 and 12. For reference, the average values of these intensities and mass percentages for all eleven samples are provided as well.

Table 11. Element intensity averages for locations with the highest amount of activity compared to element intensity averages for each sample.

Sample	Si	Ca	Fe	K	Ti	Cu
“Hot Spots”	418.28	690.36	358.44	62.58	12.97	1.80
Sample 111	275.81	299.79	211.61	12.18	6.89	42.46
Sample 112	295.17	332.73	183.22	40.53	9.07	42.43
Sample 113	165.55	247.55	201.92	25.25	6.41	48.47
Sample 114	193.58	348.79	228.94	9.87	7.37	42.83
Sample 115	188.96	281.95	204.84	9.87	6.20	46.37
Sample 221	172.75	294.15	177.19	26.38	6.33	42.75
Sample 232	247.81	348.56	236.18	30.25	8.51	47.69
Sample 241	138.90	237.11	182.12	22.62	6.17	53.47
Sample 244	177.60	203.04	176.61	24.09	5.64	47.93
Sample 142	167.35	265.59	207.94	29.76	6.31	43.40
Sample 131	2.18	0.57	48.90	0.68	1.09	71.54

Table 12. Element mass percentage averages for locations with the highest amount of activity compared to element mass percentage averages for each sample.

Sample	%Si	%Ca	%Fe	%K	%Ti	%Cu
“Hot Spots”	42.89	31.94	5.41	3.44	0.528	0.043
Sample 111	46.56	22.05	4.13	1.19	0.38	0.08
Sample 112	42.68	21.93	3.15	3.38	0.45	0.09
Sample 113	36.33	23.49	5.62	3.07	0.46	0.16
Sample 114	33.98	27.28	5.82	3.19	0.49	0.13
Sample 115	40.01	25.37	5.47	1.15	0.45	0.35
Sample 221	37.05	27.39	4.57	3.12	0.46	0.12
Sample 232	40.23	23.98	4.67	2.79	0.46	0.20
Sample 241	36.22	25.95	5.76	3.44	0.54	0.36
Sample 244	42.99	22.05	4.87	3.42	0.44	0.23
Sample 142	35.37	26.83	7.20	4.17	0.03	0.22
Sample 131	0.73	0.36	3.29	0.00	0.31	1.23

When considered in terms of difference between average “Hot Spot” values and av-

erage fallout values, Cu presence was a significant factor. The numerical results of this study indicate that the amount of Cu present in high-activity regions is significantly lower than in less radioactive regions of fallout, with an average mass percentage of 0.04 ± 0.03 for hot spots and an average mass percentage of 0.29 ± 0.3 for all samples. When the Cu-rich sample 131, the least radioactive sample and a significant outlier, is removed from the data set, the average over all of the measured samples was a mass percentage of 0.19 ± 0.09 .

This analysis also identified Ca as an indicator of activity. The two samples with the highest activity levels, 114 and 221, show the highest average concentrations of calcium among all eleven fallout samples. Ca prevalence in regions of high activity has held true in previous studies, which was noted in a preceding section of this paper. The numerical results of this study indicate that the amount of Ca present in high-activity regions is 4-10% higher than in less radioactive regions of fallout, with an average of $31.94 \pm 3.9\%$ for hot spots and an average of $24.63 \pm 2.2\%$ for all samples.

Because a previous study on the same set of fallout found that activity was most concentrated in regions composed of mafic glass [3], which can be identified based on significant amounts of Ca, Fe, and Mg, the latter two elements were also investigated more closely. Mg presence was also notable, contributing to 1-2% more of the composition of the regions of fallout with the highest activity. This is a significant increase, given that, on average, Mg levels throughout the fallout averaged $3.35 \pm 0.3\%$. High activity areas averaged $4.70 \pm 0.8\%$. While increased Fe presence was not statistically significant, regions of high activity did exhibit slightly more Fe than the fallout samples on average. Average values were $5.41 \pm 0.7\%$ for hot spots and $5.13 \pm 1.1\%$ for all samples. Based on these results, the theory of mafic glass composition in high-activity regions is now supported by micro-XRF analysis in addition to previous techniques.

7. Conclusion

7.1 Conclusions of Research

The aim of this research was to develop a method for rapid detection and analysis of actinides and correlated materials in nuclear fallout debris using micro-XRF and PCA. This was accomplished through the completion of two main projects. The first was a collaborative effort with NIST and the FBI Laboratory to produce an SRM that is a surrogate for glassy nuclear fallout debris in a modern urban environment, which will be useful to researchers for the development and validation of nuclear forensics methods. The second was a quantitative analysis of element-actinide correlation in real nuclear test fallout debris, which will contribute further to the body of knowledge surrounding the formation of nuclear fallout.

The first objective, which sought the creation of a NIST SRM that would simulate nuclear fallout while remaining consistent across all samples, has progressed with promising results. The samples analyzed in this study proved to be very similar, with a 1.515% difference in composition based on the first two principle components, which accounted for up to 79% of the variance in the samples. Preliminary infinite thickness was found to be achieved at a depth of 2.242 mm, resulting in a minimum sample size of 0.607 g for the equipment used in this study. Furthermore, it was shown that for a simplified model, the SPUD material becomes indistinguishable from a bulk sampling of real nuclear fallout material. This result suggests that, though the resemblance may not be exact, the SPUD material is a reasonable facsimile for nuclear fallout in terms of laboratory method testing.

The second objective, which sought to separate the actinides in fallout based on collocated media, also proved successful in that the ninetieth percentile of radioactive locations were shown to exist in regions with similar elemental compositions. It was

shown that the best elemental descriptors of variance in fallout are Ca, Si, Fe, K, Ti, and Cu. Ca was shown to exist in levels 4-10% higher than average in the regions of the fallout that exhibited the highest activity, and Mg was shown to exist in levels 1-2% higher, supporting Dierken's earlier conclusion that fallout regions with higher activity tend to be found in mafic glass. The sample with the least activity, sample 131, had the highest Cu content, while regions with higher activity were found to be depleted in Cu. Only 11 fallout samples were examined in this study, so substantial further work is needed in this area, but this technique shows promise in the identification of areas of interest in nuclear fallout.

7.2 Recommendations for Future Research

Due to time constraints, only two SPUD samples were analyzed in this study. Currently, 13 more exist at AFIT, and a likely further 15, this time doped with 22% U-235, will eventually require analysis. It is recommended that the analysis performed on these samples mirror the analysis performed in this study as closely as possible.

The historical fallout from the Nevada Test Site was all acquired from the same test area, and only 11 samples were able to be analyzed. A further study of the remaining samples provided, as well as samples from tests accomplished in different environments and under different conditions, should be performed. An analysis of prominent chemical compositions within glassy fallout features, rather than an element-by-element analysis, will likely provide additional information in terms of actinide correlation. Additionally, if and when higher-quality autoradiography film becomes available, it should be used to obtain data for any fallout relevant to future studies. It is predicted that experimental accuracy will increase significantly as autoradiography image quality increases.

The PCA analysis used in this experiment is adequate for a relatively small number

of samples in a user-supervised setting. However, large-scale data analysis is likely better suited to unsupervised computing. Further work in this area may allow the classification of fallout samples to be assigned to a machine learning system that uses PCA to reduce data set dimensionality while maintaining a low error value. NIPALS PCA, which generates only a few of the most important PCs for any given data set [35], may be particularly well-suited to this process.

A possible further application of PCA analysis to this research that has not yet been explored is a specific study of the uranium content across different samples. Isotopic differences in uranium can often be traced to particular geographic locations or enrichment techniques, allowing the nuclear forensic scientist to identify potential sources of material in a weapon detonated by an unknown entity. Follow-on work would include a study to be performed on specific uranium fluorescent lines in an attempt to match line shape characterizations with identifiable environmental factors.

7.3 Significance of Research

A standard reference material for post-detonation, fresh-fission product nuclear fallout in a modern urban environment was created and tested. Once its development and characterization are complete, it will be used to reliably test nuclear forensics measurement capabilities and techniques, thereby improving method development, validation, testing, and preparedness in the nuclear forensics community. It also allows the FBI Laboratory, among other government agencies, to demonstrate the efficacy, accuracy, and precision of their analysis methods, providing needed legal defensibility of evidence analysis.

This research also provides further development of a method intended to further advance nuclear forensic analysis speed and efficiency through the rapid identification of areas of interest in nuclear fallout samples. This method, though it still requires

more refinement, is simple and straightforward. It does not require extended periods of data acquisition or a significant amount of computer processing power, allowing for execution and analysis of results that could be accomplished within a matter of hours.

Bibliography

1. J. L. Mann, M. A. Tyra, and J. L. Molloy, "Surrogate Post-Detonation Urban Debris," MARC X Conference, April 2015.
2. M. L. Monroe, "Elemental Identification for Forensics Analysis of Nuclear Fallout Debris Samples Utilizing Micro-XRF, SEM, and Autoradiography Mapping," Master's thesis, Air Force Institute of Technology, 2013.
3. J. M. Dierken, "Analysis of Fallout Particles Using Image Registration of Autoradiography and Scanning Electron Microscopy," Master's thesis, Air Force Institute of Technology, 2014.
4. G. R. Crocker, J. D. O'Connor, and E. C. Freiling, "Physical and Radiochemical Properties of Fallout Particles," *U.S. Naval Radiological Defense Laboratory*, 1965.
5. C. E. Adams, N. H. Farlow, and W. R. Schell, "The compositions, structures, and origins of radioactive fallout particles," *Geochimica et Cosmochimica Acta*, vol. 18, pp. 42–56, 1959.
6. E. Mankin, "Principal Component Analysis: A How-To Manual for R," University of Colorado, Boulder, 2008, online. http://psych.colorado.edu/wiki/lib/exe/fetch.php?media=labs:learnr:emily_-_principal_components_analysis_in_r:pca_how_to.pdf.
7. R. C. Gostic, "Characterization of plutonium particles originating from the BO-MARC accident - 1960," dissertation, University of Nevada, Las Vegas, 2010.
8. J. Jernstrom, M. Eriksoon, R. Simon, G. Tamborini, O. Bildstein, R. C. Marquez, S. R. Kehl, T. F. Hamilton, Y. Ranebo, and M. Betti, "Characterization and source term assessments of radioactive particles from Marshall Islands using non-destructive analytical techniques," *Spectrochimica Acta Part B*, vol. 61, pp. 971–979, 2006.
9. P. P. Parekh, T. M. Semkow, M. A. Torres, D. K. Haines, J. M. Cooper, P. M. Rosenberg, and M. E. Kitto, "Radioactivity in Trinitite six decades later," *Journal of Environmental Radioactivity*, vol. 85, pp. 103–120, 2005.
10. F. Belloni, J. Himbert, O. Marzocchi, and V. Romanello, "Investigating incorporation and distribution of radionuclides in trinitite," *Journal of Environmental Radioactivity*, vol. 102, pp. 852–862, 2011.
11. A. J. Fahey, C. J. Zeissler, D. E. Newbury, J. Davis, and R. M. Lindstrom, "Postdetonation nuclear debris for attribution," *PNAS*, vol. 107, no. 47, 2010.

12. C. Wallace, J. J. Belluci, A. Simonetti, T. Hainley, E. C. Koeman, and P. C. Burns, "A multi-method approach for determination of radionuclide distribution in trinitite," *Journal of Radioanalytical and Nuclear Chemistry*, vol. 298, pp. 993–1003, 2012.
13. J. Molloy and J. Sieber, "Classification of microheterogeneity in solid samples using micro-XRF," *Analytical and Bioanalytical Chemistry*, vol. 392, pp. 995–1001, 2008.
14. ———, "Assessing microscale heterogeneity in batches of reference materials using microbeam XRF," *X-Ray Spectrometry*, vol. 40, pp. 306–314, 2011.
15. C. J. Bridgman, *Introduction to the Physics of Nuclear Weapons Effects*. Fort Belvoir, VA: Defense Threat Reduction Agency, 2001, vol. 8725.
16. "Directory Listing of P4. Nuclei and Particles," University of Maryland, online. <http://physics.umd.edu/deptinfo/facilities/lecdem/services/avmats/slides/thumbs.php?title=P4>.
17. J. M. Guthrie and J. R. Ferguson, "Overview of X-Ray Fluorescence," University of Missouri-Columbia, August 2012, online. http://archaeometry.missouri.edu/xrf_overview.html.
18. Camerino, "Lectures about XRF (X-Ray Fluorescence)," Advanced Physics Laboratory, Laurea Magistrale in Fisica, 2013, online. http://gnxas.unicam.it/XASLABwww/pag_teaching/lect_XRF.pdf.
19. "What Does Infinite Thickness Mean in Reference to XRF?" Bruker Corporation, 2015, online. <https://www.bruker.com/products/x-ray-diffraction-and-elemental-analysis/handheld-xrf/infinite-thickness-xrf-analysis.html>.
20. N. Kucuk, Z. Tumsavas, and M. Cakir, "Determining photon energy absorption parameters for different soil samples," *Journal of Radiation Research*, vol. 54, no. 3, pp. 578–586, 2013.
21. "Silicon Drift Detector Development," PNSensor - Research and Development of Advanced Radiation Detectors, online. <http://www.pnsensor.de/Welcome/Detectors/SDD/>.
22. C. Fiorini, J. Kemmer, P. Lechner, K. Kromer, M. Rohde, and T. Schulein, "A new detection system for x-ray microanalysis based on a silicon drift detector with Peltier cooling," *Review of Scientific Instruments*, vol. 68, no. 6, pp. 2461–2465, 1997.
23. "Thermoelectric Coolers," TEC Microsystems GmbH, 2015, online. http://www.tec-microsystems.com/EN/Thermoelectric_Coolers.html.

24. W. Dwinnel, “Principal Components Analysis,” Data Mining in MATLAB, August 2010, online. <http://matlabdatamining.blogspot.com/2010/02/principal-components-analysis.html>.
25. J. Shlens, “A Tutorial on Principal Component Analysis,” *arXiv preprint arXiv:1404.1100*, December 2005.
26. E. W. Weisstein, “Gram-Schmidt Orthonormalization,” Wolfram Research, Inc., 2006, online. <http://mathworld.wolfram.com/Gram-SchmidtOrthonormalization.html>.
27. “Standard Reference Materials: Definitions,” National Institute of Standards and Technology, April 2015, online. <http://www.nist.gov/srm/definitions.cfm>.
28. “Guidelines for the Selection and Use of Reference Materials,” International Laboratory Accreditation Cooperation, 2005, online. http://www.enao-eth.org/documents/ILA_P56laj_NCEF.pdf.
29. J. Molloy, “Generalized protocol for microheterogeneity analysis using microbeam x-ray fluorescence,” National Institute of Standards and Technology.
30. “Certificate of Analysis: Standard Reference Material 2702, Inorganics in Marine Sediment,” National Institute of Standards and Technology, July 2012.
31. “Certificate of Analysis: Standard Reference Material 2703, Inorganics in Marine Sediment,” National Institute of Standards and Technology, July 2012.
32. U. Kohler and M. Luniak, “Data Inspection Using Biplots,” *The Stata Journal*, vol. 5, no. 2, pp. 208–223, 2005.
33. J. Hubbell and S. Seltzer, “Tables of X-Ray Mass Attenuation Coefficients and Mass Energy-Absorption Coefficients from 1 keV to 20 MeV for Elements $Z = 1$ to 92 and 48 Additional Substances of Dosimetric Interest,” Radiation Physics Division, PML, NIST, July 2004.
34. “X-Ray Properties of the Elements,” Lawrence Berkeley National Laboratory, 1995, online. http://henke.lbl.gov/optical_constants/pert_form.html.
35. T. Howley, M. G. Madden, M.-L. O’Connell, and A. G. Ryder, “The effect of principal component analysis on machine learning accuracy with high-dimensional spectral data,” *Knowledge-Based Systems*, vol. 19, no. 5, pp. 363–370, 2006.

REPORT DOCUMENTATION PAGE

Form Approved
OMB No. 0704-0188

The public reporting burden for this collection of information is estimated to average 1 hour per response, including the time for reviewing instructions, searching existing data sources, gathering and maintaining the data needed, and completing and reviewing the collection of information. Send comments regarding this burden estimate or any other aspect of this collection of information, including suggestions for reducing this burden to Department of Defense, Washington Headquarters Services, Directorate for Information Operations and Reports (0704-0188), 1215 Jefferson Davis Highway, Suite 1204, Arlington, VA 22202-4302. Respondents should be aware that notwithstanding any other provision of law, no person shall be subject to any penalty for failing to comply with a collection of information if it does not display a currently valid OMB control number. **PLEASE DO NOT RETURN YOUR FORM TO THE ABOVE ADDRESS.**

1. REPORT DATE (DD-MM-YYYY) 24-03-2016			2. REPORT TYPE Master's Thesis		3. DATES COVERED (From — To) June 2014 - March 2016	
4. TITLE AND SUBTITLE Nuclear Forensics Applications of Principal Component Analysis on Micro X-ray Fluorescence Images					5a. CONTRACT NUMBER	
					5b. GRANT NUMBER	
					5c. PROGRAM ELEMENT NUMBER	
6. AUTHOR(S) Castro, Sarah T., 2d Lt, USAF					5d. PROJECT NUMBER	
					5e. TASK NUMBER	
					5f. WORK UNIT NUMBER	
7. PERFORMING ORGANIZATION NAME(S) AND ADDRESS(ES) Air Force Institute of Technology Graduate School of Engineering and Management (AFIT/EN) 2950 Hobson Way WPAFB OH 45433-7765					8. PERFORMING ORGANIZATION REPORT NUMBER AFIT-ENP-MS-16-M-061	
9. SPONSORING / MONITORING AGENCY NAME(S) AND ADDRESS(ES) Defense Threat Reduction Agency DTRA-J9-NTF POC: Lt Col Matthew Zickafoose (matthew.s.zickafoose.mil@mail.mil) 8725 John J. Kingman Road Ft. Belvoir, VA 22060					10. SPONSOR/MONITOR'S ACRONYM(S) DTRA	
					11. SPONSOR/MONITOR'S REPORT NUMBER(S)	
12. DISTRIBUTION / AVAILABILITY STATEMENT Distribution Statement A. Approved for public release; Distribution Unlimited.						
13. SUPPLEMENTARY NOTES This material is declared work of the U.S. Government and is not subject to copyright protection in the United States.						
14. ABSTRACT A method is developed for rapid detection and analysis of actinides and correlated materials in nuclear fallout debris using principal component analysis on quantified micro x-ray fluorescence intensity values. This method is then applied to address goals of nuclear forensics. The first implementation is a collaborative effort with the National Institute of Standards and Technology and the Federal Bureau of Investigation Laboratory to produce a standard reference material that is a surrogate for glassy nuclear fallout debris in a modern urban environment. This reference material will enable researchers in the development and validation of nuclear forensics methods. A method for determining material homogeneity is developed and demonstrated. A preliminary minimum sample size for the surrogate fallout SRM is calculated to be 0.607 g based on an infinite thickness depth of 2.242 mm. It is also shown that, for an adequately simple model, the surrogate fallout SRM is indistinguishable from real fallout. The second implementation is a quantitative analysis of element-actinide correlation in historical nuclear test fallout debris, which will contribute further to the body of knowledge surrounding the formation of nuclear fallout. Eleven historical fallout samples are used. A method for determining the elemental composition descriptors that best account for the variance in these samples is developed. A trend in the composition of media surrounding areas of significant activity, based on correlation of autoradiography images, is confirmed for micro x-ray fluorescence.						
15. SUBJECT TERMS Micro-XRF, Principal Component Analysis						
16. SECURITY CLASSIFICATION OF:			17. LIMITATION OF ABSTRACT	18. NUMBER OF PAGES	19a. NAME OF RESPONSIBLE PERSON	
a. REPORT	b. ABSTRACT	c. THIS PAGE			Dr. John W. McClory, AFIT/ENP	
U	U	U	UU	126	19b. TELEPHONE NUMBER (include area code) (937)255-3636 x.7308; john.mcclory@afit.edu	